

Energy yield simulations of perovskite/c-Si tandem modules in real- world conditions

Mahesh Jayan



Energy yield simulations of perovskite/c-Si tandem modules in real-world conditions

Thesis report submitted in partial fulfilment of the requirements
for the degree of

Master of Science in Sustainable Energy Technology
at the Delft University of Technology

by
Mahesh Jayan (5057566)

August 2021



Mahesh Jayan: *Energy yield simulations of perovskite/c-Si tandem modules in real-world conditions* (2021)

An electronic version of this thesis report is available at <https://repository.tudelft.nl>

This work is scheduled to be defended publicly on 17 August 2021 at 11:00 AM CET

The work for this thesis was performed in:



Photovoltaic Materials & Devices group
Department of Electrical Sustainable Energy
Faculty of Electrical Engineering, Mathematics and
Computer Sciences
Delft University of Technology

Thesis committee:	Prof. Dr. Arthur Weeber	Chair
	Dr. Rudi Santbergen	Supervisor
	Dr. Aleksandra Lekic	External
	Manvika Singh	Daily supervisor

Acknowledgement

This thesis was a challenge I took up to work on a project that demanded coding and simulation. Although I was completely new to this field, I am grateful for the support received from the people around me. Firstly, I would like to thank Dr. Rudi Santbergen and Manvika Singh for providing me the opportunity to work on this project. Your wisdom, guidance and time paved the way for my thesis to the form it is today. When stuck on the little hurdles, I am grateful for Rudi's reminders that allowed me to focus on the bigger picture. I am thankful to Manvika for always being available at the latest of hours and pushing my limits to bring out the best results. I would also like to thank Dr. Malte Ruben Vogt and Dr. Carlos Ruiz Tobon for providing feedback and answering all sorts of queries through the course of this work.

An education at TU Delft wouldn't have been possible without the support of my family. Being away from them for two years have not been easy, and I will always be indebted to them for the sacrifices they have been making for me. As a family away from home, I am glad to have amazing friends around me, especially Vivek, Sreeja, Jitin, and Gary. I wish we could have weekly dinners forever that kept us sane through this pandemic. I hold you all in high regard.

I would like to thank all members of the PVMD group, from students to professors who are a constant source of inspiration and reminder that amazing things are possible when we work together towards the dream we all share. I am proud to say that I am part of the PVMD group and I hope this study contributes and become fuel to many more inspiring works in the future.

Mahesh Jayan
09th August 2021

Abstract

Performance of photovoltaic modules are widely expressed using their efficiency at Standard Test Conditions (STC). Although, real world conditions largely differ from this standard. Energy yield of photovoltaic modules at a certain location gives a clear indication of the performance of the module exposed to varying weather conditions. Photovoltaic Materials and Devices (PVMD) Toolbox developed at Delft University of Technology and implemented in MATLAB®, aims to simulate energy yield of photovoltaic modules while providing the flexibility of modifying cell-level to module-level parameters of the device. Accurately determining the irradiance falling on the module at a certain location and simulating the electrical properties of a solar cell at realistic conditions is crucial in determining the yield generated by a module. Due to the promising results displayed by the technology, in this study, energy yield of perovskite/c-Si tandem modules are simulated using newly developed daylight and parameter extraction models in PVMD toolbox.

Due to high computational efficiency and functionality offered, Preetham daylight model is implemented as an improvement to Perez model currently used in PVMD toolbox. The model considers the effect of Rayleigh and Mie scattering, and turbidity of atmosphere in determining the distribution of diffuse irradiance across the skydome. By implementing the model, three factors can now be determined: luminance distribution, RGB co-ordinates and relative spectral power distribution over the skydome for any location. Luminance is calculated for every point in sky using Perez parametric function that use coefficients derived from simulated data for different sun directions and turbidity values. For all locations considered, Preetham model calculates higher luminance over the year by ~2%. Calculated luminance values normalized against zenith luminance is used to derive CIE xyY values and consecutively, the RGB co-ordinates that are rendered real-time to create images of the skydome for every hour in chosen timeframe. By calculating the relative spectral power distribution, analysis of incident light falling on the module from all points of the skydome is possible which especially deems useful for modelling tandem modules.

To accurately simulate electrical properties of solar cell under varying operating conditions, parameter extraction model for simulated ASA J-V curves is implemented using an analytical method. For the c-Si and perovskite cells considered in the study, the reconstructed curves using extracted parameters fits ASA curve with RMSE or 1.98% and 3.02% respectively at STC.

Using these models introduced in this study, energy yield of mono-facial and bi-facial 2T/4T tandem modules are calculated and analyzed for Rome, Reykjavik and Alice Springs. Depending on air mass of a location, perovskite thickness of mono-facial 2T tandem devices are optimized to produce maximum specific yield. All considered modules generate highest yield at Alice Springs due to high insolation at the location. The yield difference between modules while using the two daylight models is insignificant at <1%. With an increase in perovskite thickness, energy yield of 2T bi-facial modules increase significantly for high albedo while it drops beyond the optimum thickness due to current mismatch for low albedo. Bi-facial 4T module on high albedo (albedo= 0.85) surfaces show best performance out of all the modules producing 36% higher yield than mono-facial 4T module for Rome.

Contents

Abstract	ii
1 Introduction	1
1.1 Background	1
1.2 Single junction solar cell technology	2
1.3 Tandem solar cell technology	3
1.4 Bi-facial solar cell technology	5
1.5 Energy yield prediction	6
1.6 PVMD Toolbox	7
1.7 Thesis objectives	10
1.8 Outline of thesis	11
2 WEATHER: Implementation of daylight model	12
2.1 Introduction	12
2.1.1 Rayleigh and Mie scattering	12
2.1.2 Turbidity	13
2.2 Existing analytical sky models	14
2.2.1 Perez model	14
2.2.2 Preetham model	15
2.2.3 Hosek-Wilkie model	15
2.3 Implementation of Preetham model in PVMD toolbox	16
2.3.1 Defined skydome in PVMD toolbox	17
2.3.2 Distribution coefficients and parametric function	17
2.3.3 Rendering the sky image	19
2.3.4 Spectrally resolving irradiance	20
2.3.5 Normalizing luminance across skydome	21
2.4 Results from Preetham daylight model	22
2.4.1 Sky image	22
2.4.2 Relative spectral power distribution	25
2.5 Conclusion	27
3 ELECTRIC: Parameter extraction from J-V curves	28
3.1 Introduction: Diode models	28
3.1.1 Five-parameter single diode model	29
3.2 About the cells	30
3.2.1 Silicon heterojunction cell	30
3.2.2 Perovskite solar cell	30
3.3 ASA curves for parameter extraction	31
3.4 Parameter extraction method	32
3.5 Model validation	35
3.6 Conclusion	37

4	Energy yield analysis of photovoltaic modules	38
4.1	Tandem cell structures	38
4.2	Energy yield calculation in toolbox	39
4.3	Real world conditions	42
4.3.1	Effect of perovskite thickness	42
4.3.2	Effect of daylight models	44
4.3.3	Effect of location	45
4.3.4	Mono-facial and bi-facial modules	46
4.4	Conclusion	48
5	Conclusions and recommendations	49
5.1	Implement spectrally resolved daylight model	49
5.2	Implement parameter extraction model for simulated J-V curves	50
5.3	Evaluate and analyze the energy yield of photovoltaic modules	50
5.4	Recommendations	51
A	Solar spectral model	53
B	Extracted cell parameter behaviour	55
C	Module geometry and metallization input	59
	Bibliography	60

List of Figures

Figure 1.1	Global LCOE from utility-scale renewable energy sources	1
Figure 1.2	Device architectures for SHJ solar cells	2
Figure 1.3	Major loss mechanisms considered in Shockley-Queisser limit for a solar cell in AM 1.5 spectrum	4
Figure 1.4	Working principle of a typical tandem cell	4
Figure 1.5	Tandem solar cell architectures	5
Figure 1.6	Schematic diagram to demonstrate bi-facial solar cell technology	6
Figure 1.7	2-T and 4-T configurations for perovskite/c-Si bi-facial tandem cell	6
Figure 1.8	Structure of PVMD toolbox	9
Figure 2.1	Behaviour of Rayleigh and Mie scattering	13
Figure 2.2	Meteorological range v/s turbidity values	13
Figure 2.3	Preetham model implementation flowchart	16
Figure 2.4	Coordinate system of the skydome used in Preetham model	17
Figure 2.5	Comparison of sky images rendered using Perez and Preetham models	22
Figure 2.6	Sky images for Day 1 hour 12 for every month of the year in Rome, Italy	24
Figure 2.7	Effect of turbidity during sunset on May 1 at Rome, Italy	25
Figure 2.8	Sky elements chosen over the skydome to calculate relative spectral power distribution	25
Figure 2.9	The relative spectral power distribution for three points in skydome at noon of May 1 in Rome, Italy	26
Figure 2.10	The relative spectral power distribution at triangle area 2 for three times of the day on May 1 in Rome, Italy	26
Figure 3.1	Equivalent circuit of single-diode model for single solar cell	29
Figure 3.2	Cell structure and J-V curve at STC of SHJ cell	30
Figure 3.3	Cell structure and J-V curve at STC of perovskite cell	31
Figure 3.4	The J-V curves simulated from ASA for SHJ cell at different irradiances and different temperatures	32
Figure 3.5	Process diagram for parameter extraction model	33
Figure 3.6	The reconstructed and simulated J-V curves for SHJ and perovskite cells at STC	36
Figure 3.7	RMSE between reconstructed and simulated ASA J-V curve of SHJ cell at different irradiance intensities and temperatures	36
Figure 4.1	Simulated perovskite/c-Si tandem cell structures	39
Figure 4.2	Absorptance and reflectance of 2T bi-facial perovskite/c-Si tandem cell under STC for front side and rear side illumination	40
Figure 4.3	Sensitivity maps of the module for front and rear irradiance	40
Figure 4.4	Calculated module temperature for every hour of the year at Rome from PVMD toolbox	41
Figure 4.5	Hourly DC energy yield (blue) and incident irradiance for every hour of the year in Rome	42

Figure 4.6	The effect of perovskite thickness on specific energy yield of 2T mono-facial tandem module at three different locations	43
Figure 4.7	Implied photo-current of bi-facial 2T tandem module as a function of perovskite thickness	44
Figure 4.8	The annual energy yield of SHJ and mono-facial 2T/4T tandem modules at Reykjavik, Rome and Alice Springs	45
Figure 4.9	Effect of albedo on AEY of bi-facial 2T tandem module at Rome as a function of perovskite thickness	46
Figure 4.10	Effect of albedo on AEY of bi-facial 4T tandem module at Rome as a function of perovskite thickness	47
Figure 4.11	Contribution of perovskite top cell and c-Si bottom cell to AEY of bi-facial 4T tandem module for different albedo surfaces	48

Abbreviations and symbols

LCOE	Levelized cost of electricity
c-Si	Crystalline silicon
2-T/4-T	2-Terminal/4-Terminal
STC	Standard Test Conditions
DNI	Direct Normal Irradiance
DHI	Direct Horizontal Irradiance
T	Turbidity
AM	Air mass
CLEM	Calibrated Lumped Element Model
RMSE	Root Mean Square Error
R	Reflectance
A	Absorptance
T	Transmittance
γ	Angular distance between viewing direction and sun position
θ	Angle between zenith and viewing direction
θ_s	Solar zenith angle
Y_z	Zenith luminance
Y_{rel}	Relative luminance
x	x chromaticity
y	x chromaticity
R/G/B	Red/Green/Blue vector co-ordinates
S	Spectral radiant power
m	Optical air mass
I	Irradiance
ω	Area of sky element
I_{ph}	Photo-generated current
I_0	Saturation current
R_s	Series resistance

n	Ideality factor
k_B	Boltzmann constant
q	Electron charge
T	Temperature (K)
R_{sh}	Shunt resistance
J_{sc}	Short-circuit current
V	Voltage
σ	Stefan-Boltzmann constant
E_g	Bandgap energy

1 Introduction

1.1. Background

The world's energy requirement is predicted to increase by 50% between 2018 and 2050 [1]. Currently, fossil fuels cover major portion of this demand. Due to the pollution risk that fossil fuels poses, a shift towards using renewable sources is imperative. Methods for transition of energy consumption from fossil fuels to renewable sources have been a requirement and a point of interest for researchers for the past few years. Few of the major renewable energy sources that have been studied and implemented include wind, solar, biomass, hydropower and tidal energy.

According to IRENA, 6586 TWh of electricity was generated in 2018 from renewable energy. This accounts for 24.9% of the total electricity production from all sources of energy. About 9% of this was contributed by solar energy, which saw an increase of 28% when compared to 2017 [2]. The share of solar PV in energy production is increasing rapidly due to its high potential, flexibility and dropping costs. The extensive research in the field has helped improve its efficiency considerably since its conception, from an efficiency of less than 1%, to 29.52% in 2020 for perovskite/c-Si tandem cells [3]. As shown in Figure 1.1, this has also helped in improving investments in the sector causing the levelized cost of electricity (LCOE) for solar PV to reduce by 85% (\$ 0.057/kWh) over the period of 2010 to 2020 [4].

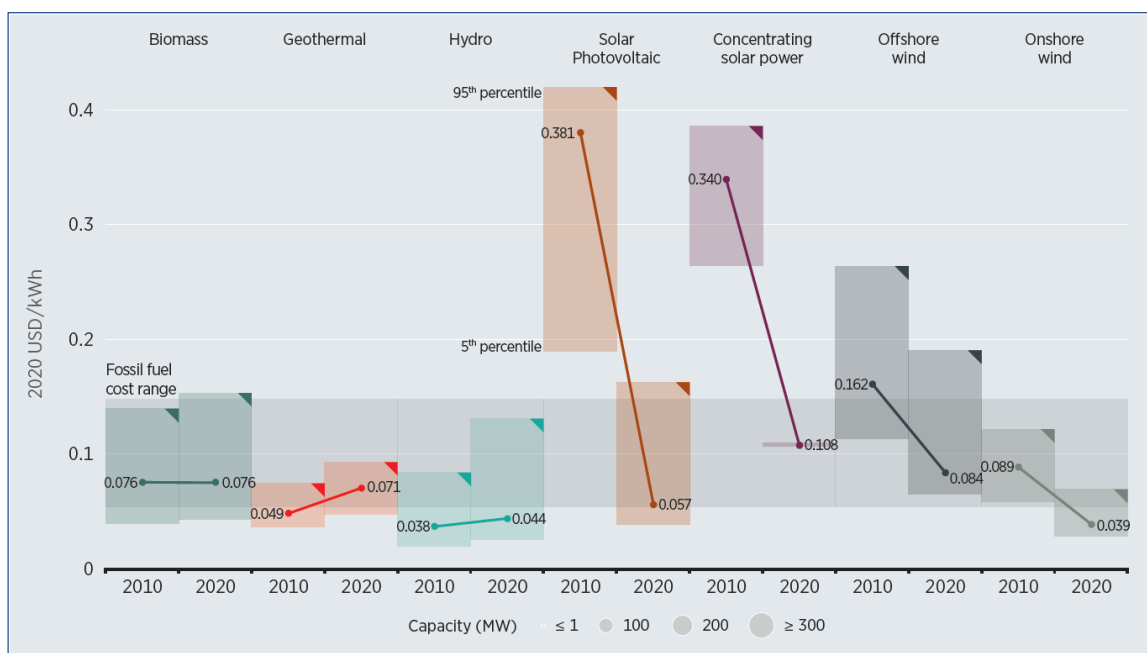


Figure 1.1: Global LCOE from utility-scale renewable energy sources [4]

Predicting the energy yield of innovative cell technologies in experimental stage helps boost investment towards the photovoltaic technology and bolsters the public opinion towards it. In this study, the energy yield of mono-facial and bi-facial perovskite/c-Si tandem modules are estimated and compared to state-of-the-art silicon heterojunction solar modules using the improved in-house developed PVMD toolbox.

1.2. Single junction solar cell technology

1.2.1. Crystalline silicon cell technology

Efficiency of conventional single-junction c-Si cells have been approaching their theoretical limit of $\sim 27\%$, owing to years of research in the technology [5], [6]. To further improve the efficiency of c-Si solar cell and reduce the cost of production, silicon heterojunction solar cells with passivating layers on the Si absorber layer have been introduced. The highest energy conversion efficiency recorded for a SHJ cell is 26.6% by Yoshikawa et.al using an interdigitated back contact cell structure [7], [8]. Although the quantum of research conducted in SHJ cells is limited when compared to the conventional cells, according to Louwen et.al, the production cost for a SHJ module has reached 0.48-0.56 \$/Wp while the cost for a conventional c-Si module is 0.50 \$/Wp [9].

Extensive research in c-Si solar cells have improved their energy conversion efficiencies beyond 25% in recent years [7], [10]–[12]. This efficiency hike can be attributed to the introduction of passivating layers to c-Si solar cells. Silicon heterojunction cells consist of c-Si wafer passivated on both sides by layers of intrinsic and doped hydrogenated amorphous silicon (a-Si:H). Upon illumination, the photo-generated majority carriers are collected in the doped amorphous Si layer through conductive electron and hole transporting layers [13]. The thickness of the intrinsic layer is optimized for maximum conductivity and ample surface passivation. Similarly, the doped a-Si:H layer is kept as thin as possible to minimize losses due to parasitic absorption [8].

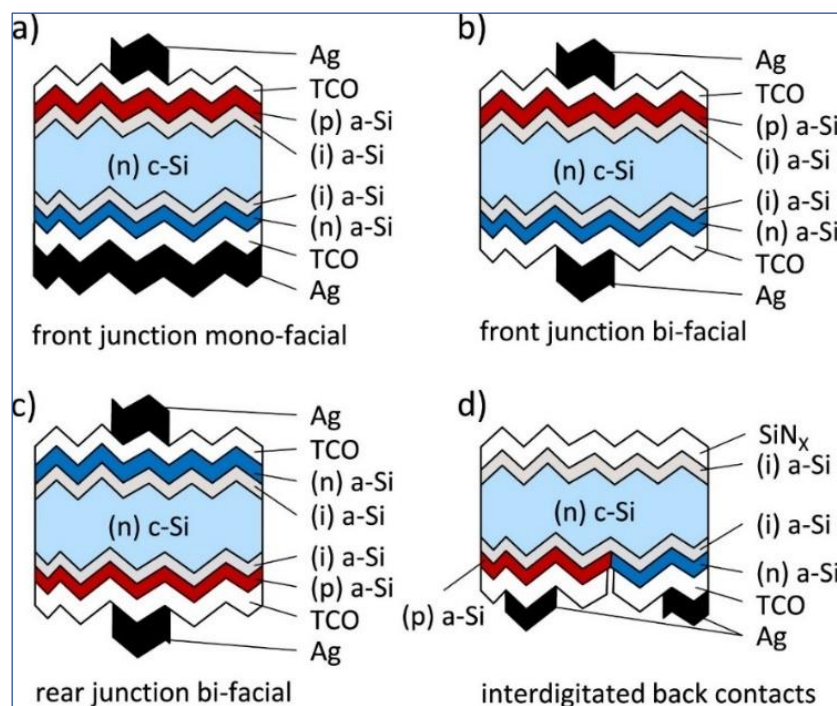


Figure 1.2: Device architectures for SHJ solar cells [8]

Different cell configurations are possible for SHJ cells as shown in Figure 1.2. For absorber materials with short minority charge-carrier lifetime, front contacts allow high short-circuit current density (Figure 1.2(a)). Although, with the presence of passivating contacts and high-quality absorber material that enables high charge-carrier lifetime, high short-circuit current densities can be obtained irrespective of the position of the minority charge-carrier contact (Figure 1.2 (c,d)). The highest efficiency obtained for a SHJ cell (two-side contacted) was fabricated by placing the p-contact on the front side of the n-type c-Si wafer [8].

1.2.2. Perovskite cell technology

Crystalline silicon solar cells have been commercialized to a large extent and the maximum practical efficiency has been nearly achieved. But to reduce the cost of a photovoltaic system, the performance of the module needs to be improved further. Perovskite absorbers have been an ongoing area of interest for the past few years due to its various advantages such as tunable bandgap depending on composition, high charge carrier mobility, ease of fabrication using earth-abundant raw materials and good response to short wavelength photons [14]–[18]. In addition, their high absorption coefficient allow the perovskite thickness to be much lower compared to traditional absorber layers [19].

Perovskite is a crystal structure of the form ABX_3 , where A and B are cations and X represents an anion. Out of the many perovskite structures possible, only few are suitable as a light absorber for solar cells mainly due to the need to align the bandgap with other materials in contact in the cell. The tunable bandgap and excellent response of perovskite to high energy photons make it an ideal candidate as a top cell for tandem structures [20].

Due to the high attention the technology has been gaining, in this study, we shall focus on the performance of tandem solar cells that comprise of perovskite and c-Si solar sub-cells [21]–[28]. The structure of the cells used in this study will be discussed further in detail in Chapter 3.

1.3. Tandem solar cell technology

The Shockley-Queisser limit has been recognized as the maximum theoretical efficiency that a single junction solar cell can attain. Thermalization, and below bandgap losses are large contributors to the limit in the overall efficiency of the cell as shown in Figure 1.3. These losses are mainly caused due to the difference between the photons incident on the cell and the bandgap of the cell. To attain the maximum theoretical efficiency, it is imperative to minimize these losses. Since silicon heterojunction cells can absorb photons in a certain wavelength range, irradiance spectra can be utilized better by improving the bandgap of the cell [29]. Si-based tandem cells are being researched in the last few years by stacking cells of higher bandgap on c-Si absorber, thus improving the overall bandgap of the tandem cell. The top cells currently used in tandem technology include GaAs, Indium Gallium Phosphide and perovskite. Their recorded efficiencies have surpassed the efficiency of single junction solar cells, proving their potential [30].

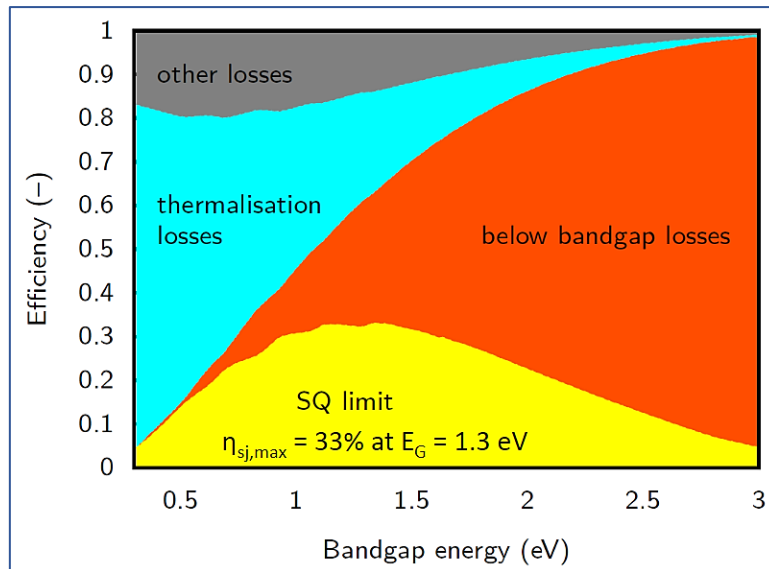


Figure 1.3: Major loss mechanisms considered in Shockley-Queisser limit for a solar cell in AM 1.5 spectrum [31]

1.3.1. Working principle

Tandem cells consist of multiple stacked absorber layers designed to maximize photon absorption and minimize the spectral mismatch losses. In practice, the simple tandem structure consists of two sub-cells. As explained in Fang et.al, high-energy photons are absorbed on the wide bandgap top cell and low energy photons are collected in the bottom cell with a narrow bandgap. Overall, the top and bottom cells improve the open circuit voltage and photo-response of the tandem structure respectively [19]. The general structure of a tandem solar cell is illustrated in Figure 1.4.

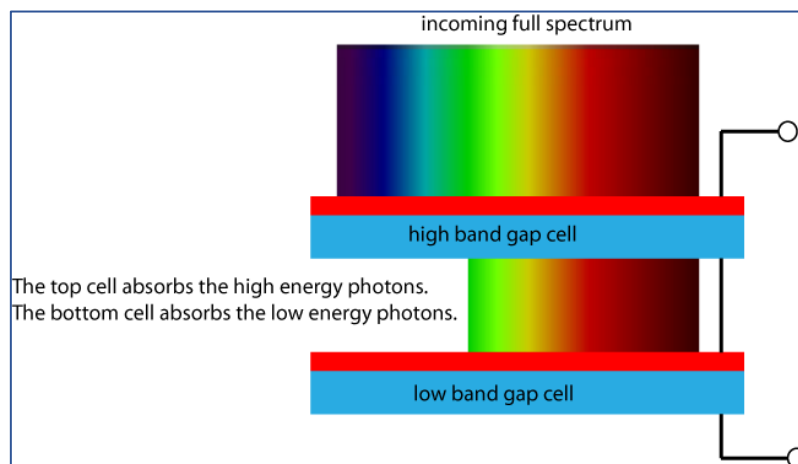


Figure 1.4: Working principle of a typical tandem cell [32]

1.3.2. Cell configuration

The method of stacking and connecting the sub-cells affect the photon absorption and utilization in the tandem cell. Mainly, two types of configurations are used: two-terminal (2-T) and four-terminal (4-T). The 2-T tandem cell configuration has the bottom cell fabricated onto the top cell or vice-versa, electrically connected in series. This structure demands proper current-matching between the sub-cells to ensure that the current of the total tandem is not reduced drastically.

The 4-T configuration has mechanically-stacked, electrically isolated sub-cells, allowing independent optimization and no losses from current mismatch. Mechanically-stacked 4-T tandem solar cells (Figure 1.5 (b)) do not require current matching since the top and bottom cells are physically separate. Optically coupled 4-T devices (Figure 1.5 (c)) separate the incident light into shorter and longer wavelength photons using an optical splitter which is absorbed by the top and bottom cells respectively. Although, dichroic mirrors that form the optical splitter is expensive for commercial use [19], [33].

While solely considering the optical absorption capabilities, the 2-T setup is preferable due to fewer transparent electrodes compared to 4-T cell, further reducing the reflection and parasitic absorption losses. In this study, modules with 2-T and 4-T tandem solar cell configuration will be studied in further detail. The main tandem cell structures are illustrated in Figure 1.5 [19], [34], [35].

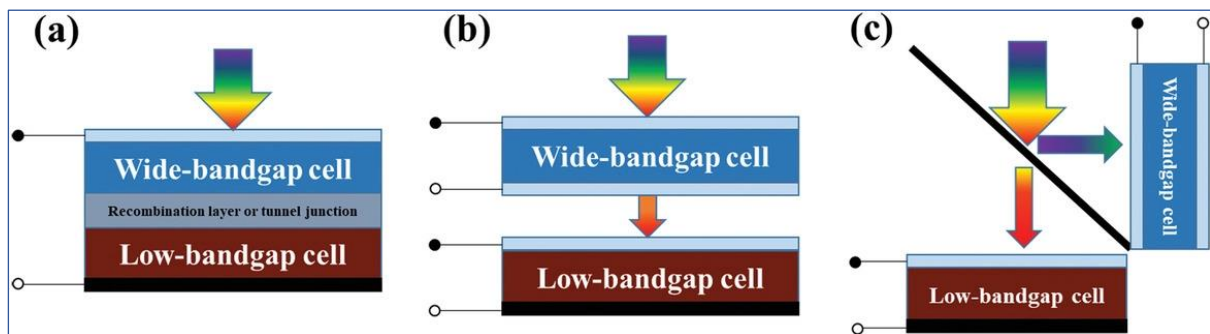


Figure 1.5: Tandem solar cell architectures. a) 2-Terminal b) Mechanically stacked 4-Terminal c) Optically coupled 4-Terminal solar cell [33]

1.4. Bi-facial solar cell technology

Bi-facial solar cells absorb photons from both front and back sides of the cell. This allows the utilization of incident, diffused and ground-reflected light (albedo radiation), which has shown an increase of 20-30% in energy yield compared to their mono-facial counterparts [36]. Due to the absence of Aluminium (or Ag) back metallization, the working temperature of the cell is comparatively lower. This further facilitates the increase in power output of the cell when compared to the mono-facial ones [37], [38].

1.4.1. Working principle

The general structure and working principle of a bi-facial solar cell is shown in Figure 1.6. Compared to mono-facial cells, bi-facial solar cells consist of an anti-reflection coating (ARC) and back contacts at the rear side of the cell. Photons that are transmitted through the ARCs on both sides of the cell form electron-hole pairs. The charge carriers that diffuse into the emitter and substrate use the internal electric field to get attracted towards the front and back contacts respectively [39], [40].

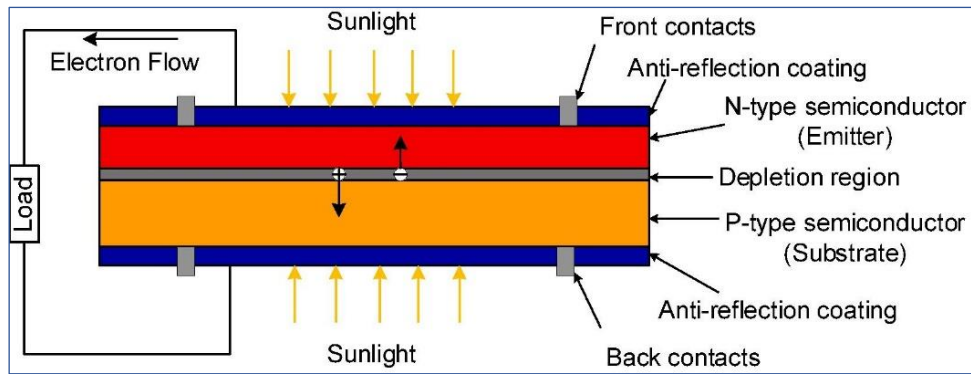


Figure 1.6: General schematic diagram to demonstrate bi-facial photovoltaic technology [40]

1.4.2. Cell configuration

From its inception, bi-facial silicon heterojunction solar cell technology has been studied actively to improve its efficiency [41]–[46]. Inherently, SHJ cell is bi-facial in nature and have low temperature coefficient (range of -0.23% to $0.3\%/^{\circ}\text{C}$), higher energy yield can be achieved [41], [47], [48]. The typical cell structure of a bi-facial SHJ cell is illustrated in Figure 1.2(c).

Similar to mono-facial tandem cells (as discussed in Section 1.3.2.), the bi-facial tandem cells can be structured in both 2-terminal and 4-terminal configurations. The extra power produced in the bottom cell of the 4-T device is linear to the irradiance that falls on it [49]. Although challenging in real-world, due to the need for current matching in 2-T bi-facial tandem cells, the top cell has to be optimized to produce higher current that matches the bottom cell. Part of the light incident on the front of the cell is transmitted to the bottom sub-cell, while the whole spectrum falling on the back is absorbed by the bottom cell [49], [50]. The general cell structure of a 2-T and 4-T bi-facial perovskite/c-Si tandem cell is shown in Figure 1.7.

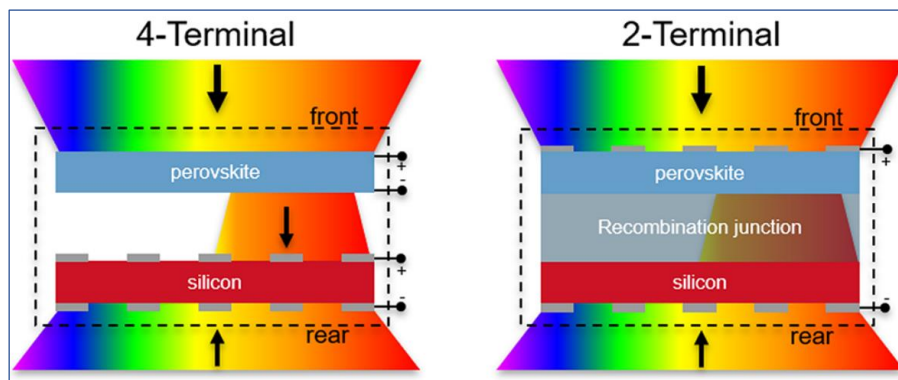


Figure 1.7: 4-T and 2-T configurations for a perovskite/c-Si bi-facial tandem cell [49]

1.5. Energy yield prediction

Efficiency at Standard Test Conditions (STC) is commonly used as a measure of the performance of a photovoltaic module. Standard test conditions mainly state an irradiance intensity of $1000\text{W}/\text{m}^2$ at 25°C cell temperature and no wind [31], [51]. Although, real world conditions may not concur with the standard test conditions. Depending on the location and time of the day, elevation angle of the sun

changes and the spectral distribution of incident light varies. Other natural effects like cloud coverage and turbidity also affect the intensity of light that falls on the module [31]. Therefore, energy yield of a module at a specific location for a certain period of time would be a more accurate representation of the performance of the module. Other than conventional cells, energy yield predictions can also be performed on novel cell technologies that are still in the laboratory phase. This would help researchers evaluate the potential of new type of cell technologies in real world conditions.

1.5.1. Yield prediction models

Multiple energy yield prediction models have been developed in recent years on an institutional and commercial level. To create and develop on a yield prediction tool, it is imperative to understand the existing models present and the features they offer. Few of the significant models available commercially are listed below.

System Advisor Model (SAM) is an open source model designed by U.S Department of Energy's National Renewable Energy Laboratory (NREL). The tool allows the modelling of most renewable sources of energy like geothermal energy, wind, and biomass. It can also be used to design photovoltaic systems with battery backup and concentrated solar power systems. Financial models can be created for these projects that exchange electricity with the power grid. Although, the SAM cannot model off-grid and hybrid systems [52].

PVsyst was developed at University of Geneva by Andre Mermound and Michel Villoz. It is one of the most widely used photovoltaic energy yield prediction models available today. A solar panel of the user's requirement can be chosen from a list of available modules and other required components to set up the design. Depending on the location, weather data is taken from Meteonorm to further calculate the yield of the system. The disadvantage of the tool is that it can only handle conventional solar modules now and cannot design systems with novel cell technologies [53].

MoBiDiG (Modelling of Bi-facial Distributed Gain) was developed in ISC Konstanz, Germany. The tool predicts the energy yield of both mono-facial and bi-facial modules. Upon validation, the tool was found to produce yield predictions at a deviation of 4.9% for five extreme days of the year. The tool also calculates the LCOE of the photovoltaic system [54].

BIGEYE developed by ECN at TNO also predicts energy yield of bi-facial modules in real world conditions at a specific location. The irradiance model uses a three-dimensional view factor and calculates the temperature of each module. The tool takes shading factors into account which could be from mounting structures or due to other panels. BIGYE is also equipped to assist the user in optimizing the photovoltaic system by choosing between module types, the right orientation setup and overall system design [55].

1.6. PVMD Toolbox

PVMD toolbox is the energy yield simulation tool developed by researchers at Photovoltaic Materials and Devices(PVMD) group in Delft University of Technology. It has been in constant development due to works from former researchers at the department. The latest version available now is the added result of the work from Abdallah Nour El Din and explained in the thesis "Improved Electrical Model and Experimental Validation of the PVMD toolbox" [56].

1.6.1. Structure of toolbox

The toolbox is programmed in MATLAB®, and currently consists of five parts that simulate the optical, thermal and electric simulations of the solar module. A brief description of the toolbox elements are given below and the structure of the toolbox is illustrated in Figure 1.8.

Cell level: The model uses GenPro4, an optical model developed for solar cells by Santbergen et.al to simulate the interaction of light with solar cells. It combines the wave and ray-optics to efficiently compute the external quantum efficiency as a function of wavelength [57]. The model can simulate mono-facial and bi-facial silicon heterojunction cells and perovskite/c-Si tandem cells. Depending on the layers that form the cell, corresponding refractive indices and extinction coefficients are input into the model. The result of simulations at defined angles of incidence and all wavelengths are the layer absorptance, transmittance and reflectance for the same [53], [56].

Module level: The module part defines the photovoltaic module structure, where the number of cells, tilt angle orientation, encapsulation and overall module configuration is defined as input from the user. Encapsulation material can be added to the module with glass layer on either sides. The *Lux* ray tracing software creates sensitivity map of the module's reaction to incident light [58]. The sensitivity can vary between 0 and 1, from minimal utilization of light to maximum absorption. Individual cell sensitivity and average sensitivity for the whole module can be calculated depending on the user's choice. The calculated sensitivity values are plotted on a sky dome with each point on it representing the position of incident light [53].

Weather model: Depending on the location of the photovoltaic system, weather data is input into the model from Meteonorm which takes into account the direct normal irradiance (DNI) and diffuse horizontal irradiance (DHI) [59]. The incident light on the module is simulated using Perez diffused irradiance model on the skydome [60]. Since the spectrum of light changes every point of the day over the year, the air mass(AM) is calculated using the zenith angle of the sun and corresponding solar spectrum is extracted. In a previous study, Garcia Goma also included the effect of shading from nearby objects and other cells by taking the location skyline into consideration [56], [61]. The weather level calculates the photo-generated current for the cells in the module for the required hours of the year and the simulated incident spectrum from the sky dome elements to create a sky map.

Thermal model: The weather data from Meteonorm and the output from Weather model, i.e, the photogenerated current and incident irradiance is used to calculate the temperature of the module. Steady state models are used in calculating the temperature, since the weather data available is on an hourly basis and the time constant for a PV module is much lesser at 7 minutes [62].

Electric model: The electric model utilizes the photo-generated current from weather model, the calculated module temperature and thermal coefficients to simulate the effect of weather conditions on the yield of the module [53], [56]. The electric model allows the user to define the metallization structure of the cell to calculate the shading losses and metallization resistance, number of bypass diodes and the configuration of the tandem cell (2T, 3T or 4T). Using the input from user and the calculated photogenerated current, I-V curves are generated for every hour of the year using one-diode model. Correspondingly, the DC annual energy yield can be calculated.

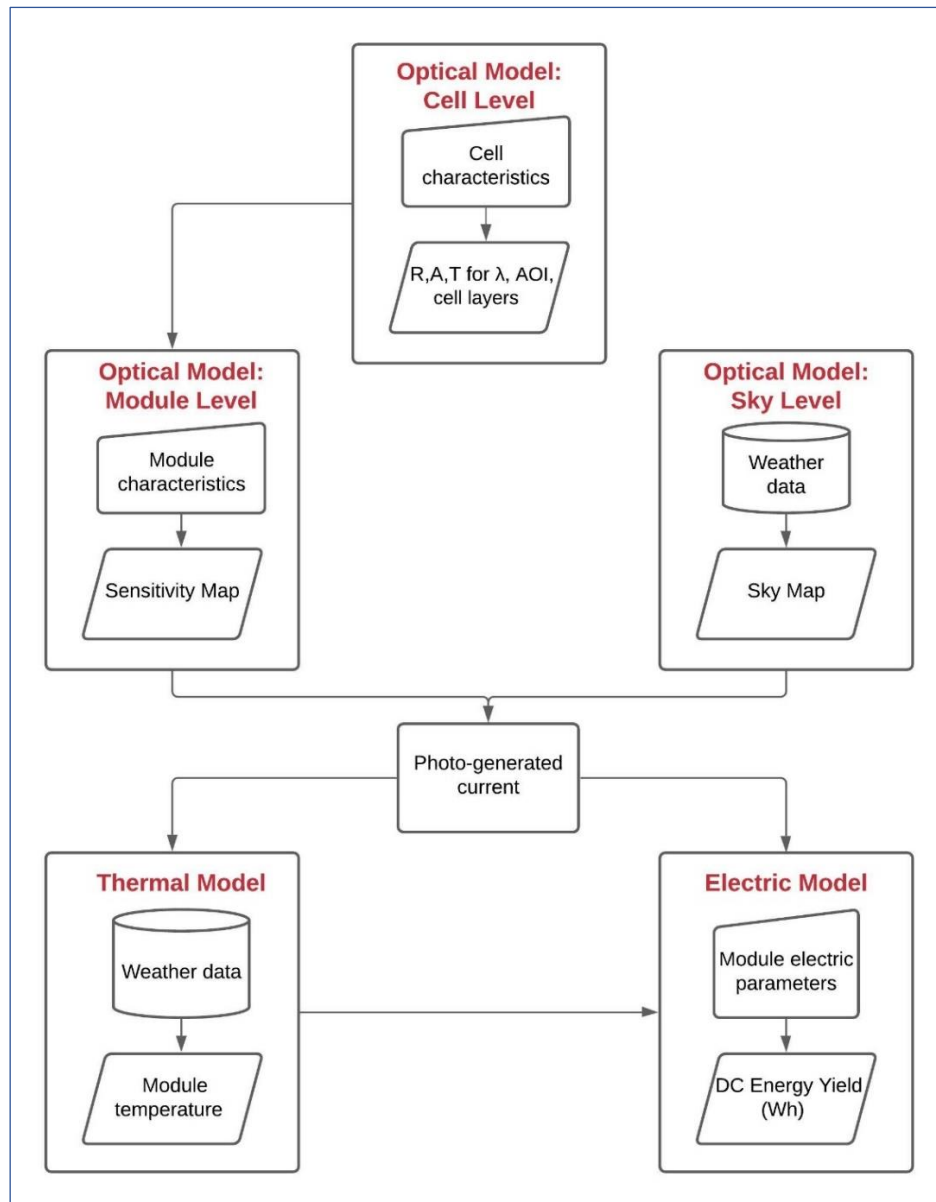


Figure 1.8: Structure of PVMD toolbox

1.6.2. Limitations of toolbox

Numerous additions and improvements have been brought into the toolbox since its inception. Although, it can be further improved. The thermal and electric behaviour of the simulated PV module is dependent on the sky model/irradiance model. The Perez all-weather sky model, currently implemented in the toolbox, calculates the luminance distribution across the skydome to further calculate the absorbed power by the module. Although this model is fairly established and accurate, further improvements have been incorporated into the model to include the effect of Rayleigh scattering, aerosol scattering, and turbidity. Analyzing the power distribution of incident light across the spectrum for a particular point in sky provides a clear understanding of the composition of light falling on the module, which is particularly beneficial for simulating tandem modules.

Realistic visual representation of the sky at any point in time gives a clear idea to the user about the expected exposure of the module towards sunlight. The visual representation would ideally include the effect of atmospheric scattering, cloud scattering and ground reflection. The recent sky models improved from the Perez model could be implemented to render realistic images of the sky that provides better clarity on the system's possibilities to the user.

The previous study introduced the single diode model to extract parameters from simulated J-V curves. Although, the validation method followed during its implementation may not ensure high accuracy in the absolute values of all the extracted parameters. The current model is designed to extract the parameters for one type of cell for different operating conditions. Introducing a validated extraction model that calculates parameters for any given model cell would allow the toolbox to take the impact of varying operating conditions on the parameters into account while simulating the energy yield.

1.7. Thesis Objectives

The objective of this thesis aims to simulate, compare and analyze the energy yield of mono-facial and bi-facial perovskite/c-Si tandem modules and SHJ modules using the PVMD toolbox with improved daylight model and parameter extraction model. Therefore, the main research goal of this thesis is to perform

Energy yield simulations of perovskite/c-Si tandem modules in real-world conditions

The sub-objectives to reach this final goal are:

Objective 1: Implement spectrally resolved daylight model

Perez all-weather model is currently implemented in the 'sky level optical model' of the toolbox to simulate the behaviour of light falling on the module at a given point in time. Currently, the effect of atmospheric particles on the spectral composition of diffuse irradiance is not considered in the simulation. Therefore, for better accuracy and understanding of the incident irradiance on the module, Preetham analytical model will be implemented in the toolbox which takes turbidity, Rayleigh scattering, and aerosol scattering of light into consideration [63]. The model will also be used to render a realistic image of the sky from the module's perspective at a given point in time for an improved user perception in the photovoltaic system modelling process.

Objective 2: Implement parameter extraction model for simulated J-V curves

Single-diode model is to be implemented to extract parameters from the J-V curves of a solar cell. The J-V curves are simulated in Advanced Semiconductor Analysis (ASA) package at varying operating conditions and the extracted parameters are used to simulate the electric performance of the cell

[64]. To ensure the accuracy of the model, the method is to be validated by rebuilding J-V curves from extracted parameters and comparing them with the simulated ones from ASA.

Objective 3: Evaluate and analyze the energy yield of photovoltaic modules

Performance of solar modules can vary in real world conditions when compared to under Standard Test Conditions. Using the improved toolbox after implementing the first two objectives, the energy yield of SHJ and perovskite/c-Si tandem modules (mono-facial and bi-facial) are simulated and compared. The simulations will be performed for three different locations around the world with diverse climatic conditions. The yields from the improved and the previous toolboxes will also be compared to showcase the variation in generated results.

1.8. Outline of Thesis

To explain the process and analysis of this study, this thesis report consists of five chapters.

Chapter 2 discusses the first objective of this study: to implement the spectrally resolved daylight model and render image of the sky. Existing sky models in use today are studied before explaining the implementation method of Preetham model. The images of the sky are rendered and spectral distribution of light on different points of the sky are visualized as results for this chapter.

Chapter 3 discusses the second objective of this thesis. The nature of the J-V curves simulated in ASA are discussed before explaining the implementation process of the single diode model. The validation process is also discussed to showcase the accuracy of the model.

Chapter 4 discusses the simulated energy yield results of mono-facial and bi-facial SHJ and perovskite/c-Si tandem modules. The variation in energy yield of modules in the three locations are studied and reasons for the same are discussed to meet the third objective of this thesis.

Chapter 5 concludes the report with answers to the research questions raised in the start of this thesis, followed by recommendations for the future studies in this field.

2

WEATHER: Implementation of daylight model

The aim of this chapter is to achieve the first objective of this thesis: implement a spectrally resolved daylight model in PVMD toolbox. Daylight model is used to calculate the intensity of incident light falling on a photovoltaic module and accurately model the energy yield of solar modules in real-world conditions. To accurately determine this aspect that allows the user to calculate absorbed irradiance by the module and implied photo-current of absorber layers, this chapter describes the implementation on Preetham daylight model in PVMD toolbox. The model determines distribution of incident light across the sky and allows real-time rendering of sky's image at a particular hour from the module's perspective. At any point in the sky, Preetham model also allows the user to determine relative spectral distribution of light across the visible spectrum. Section 2.1 briefly introduces the atmospheric effects that determine the luminance distribution. Section 2.2 describes the daylight models currently used in research and industry. Section 2.3 explains the procedure to implement Preetham model in the toolbox. The rendered images of the sky and spectral distribution of light at points across the skydome are illustrated in Section 2.4 before concluding the results in Section 2.5.

2.1. Introduction

The prediction of radiant or luminous elements using parameters from meteorological datasets is known as daylight modelling. Depending on the insolation, the intensity and angular distribution of skylight varies. One of the first weather models was introduced by Klassen in 1987 which used single scattering to simulate the appearance of the sky [65]. The models developed from Klassen's method for sky simulations demanded high computational load and time. In 1999, Perez et.al introduced an analytical model for daylight which simulated the sky in real-time with much lower load on the system [60]. Numerous daylight/weather models have been introduced since then to represent the behaviour of light passing through the atmosphere [63], [66]–[68]. They can be used to simulate diverse systems, for example, to evaluate performance of a building to incident irradiance, lighting-design applications and to render images of the sky in the gaming industry [66], [69]–[72]. Advanced daylight models simulate conditions like light scattering and turbidity that affect the attenuation of light travelling through the atmosphere. These phenomena are introduced in the upcoming sections.

2.1.1. Rayleigh and Mie scattering

Light scattering due to atmospheric particles influence the distribution of illuminance across the sky. Rayleigh scattering is the phenomenon of light deflection from particles smaller than the wavelength of light. Rayleigh also showed that the intensity of this scattering is inversely proportional to wavelength of the form, λ^{-4} [65]. This effect explains the characteristic blue color of the sky during the day, and orange hue during dusk and dawn when all other light is scattered off before reaching the viewer's eye [73] [74].

When the particle size is equal to, or larger than the wavelength of light, Mie scattering prevails [74]. It is directionally dependent, and is not wavelength-dependent like Rayleigh scattering. Mie scattering explains the white/grey color of clouds since the incident sunlight on water droplets are scattered around before reaching the viewer's eyes [73], [74]. Both forms of scattering are illustrated in Figure 2.1.

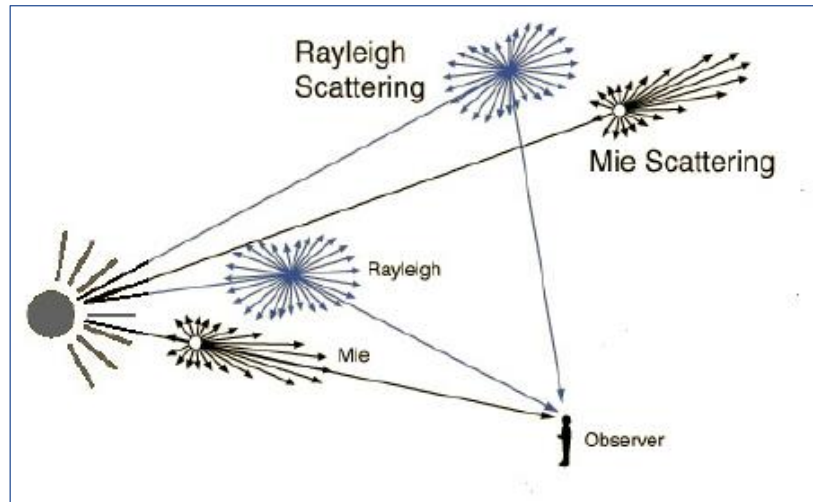


Figure 2.1: Behaviour of Rayleigh and Mie scattering [74]

2.1.3. Turbidity

Turbidity defines the light scattering properties of a fluid [75]. In the atmosphere, haze aerosol particles largely contribute to this phenomenon. A large turbidity value signifies the higher intensity of these particles causing “haziness” and lesser visibility of distant objects [70]. Turbidity is dependent on the wavelength of light, and can be calculated using meteorological range, or standard visibility as shown in Figure 2.2 [70], [76].

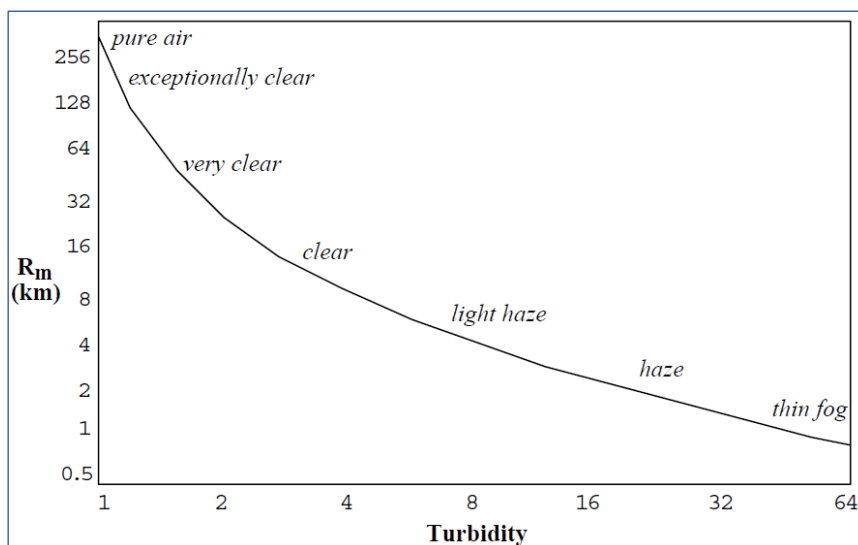


Figure 2.2: Meteorological range v/s turbidity values [70], [76]

In this thesis, newer improved analytic daylight models used in practice today are studied and the most viable option in terms of accuracy and computational speed is implemented to spectrally resolve

the irradiance falling on the module for every hour of the year for a particular location. The model would visualize the skydome and help determine energy yield of the module using the calculated photo-generated current.

2.2. Existing analytical sky models

Sky models aim to obtain the color of the sky and the spectral distribution of light across the visible spectrum at a particular point in the skydome. Numerous factors play important role in calculating the color of the sky, especially the viewing direction, position of the sun and the spectral irradiance ($W/m^2/nm$) [60], [63], [70]. To standardize sky modelling, CIE and ISO created a set of analytical models for skylight luminance distribution [77], [78]. In this section, major sky models will be analyzed. The most viable option in terms of low computational load and high accuracy was implemented in the PVMD toolbox.

2.2.1. Perez model

The toolbox currently employs Perez model to calculate the irradiance falling on the module and to visualize the behaviour of the sun across the user-chosen period of time. To define the characteristics of the sky and the corresponding luminance distribution, five coefficients (A to E) are used. Each of the coefficient represents a certain aspect of the sky:

A: Darkening ($A>0$) or brightening ($A<0$) of the horizon

B: Gradient of luminance resulting from the darkening or brightening of the horizon

C: Luminance intensity of the circumsolar region around the sun

D: Width of the circumsolar region. Holds similar significance to coefficient B

E: Represents light scattered back from the Earth's surface

The coefficients can be varied depending on the sky behaviour and is further used to calculate the relative luminance Y_{rel} given by equation 2.1.

$$Y_{rel} = F(\theta, \gamma) = (1 + Ae^{\frac{B}{\cos\theta}})(1 + Ce^{D\gamma} + E\cos^2\gamma) \quad (2.1)$$

where the angle between the zenith and viewing direction is represented by θ , and angle between the sun position and viewing direction given by γ [60], [70].

Relative luminance is normalized against relative zenith luminance, and the result is multiplied with the luminance at zenith to obtain the absolute luminance of a point in sky. The images rendered using Perez model in the PVMD toolbox will be discussed in later sections of this chapter.

Although Perez model has been widely used to simulate the sky, it carries some drawbacks while considering the accuracy of the obtained luminance distribution values. Besides being computationally expensive to render a realistic image of the sky, the model does not spectrally resolve the diffuse irradiance to consider the effect of turbidity and scattering due to particles in the atmosphere [63], [67].

2.2.2. Preetham model

High computational speed for rendering an image of the sky is one of the major drawbacks of Perez model. To tackle this, Preetham et.al presented an analytic method to calculate the luminance distribution that facilitated faster sky rendering [63]. This model fits a parametric function of turbidity to reference sky data modelled by Nishita et.al [68]. The function is created using the Perez model, which fits the chromaticity values to further determine the color of the sky [63], [70]. Chromaticity contains information that defines the color of certain object or space regardless of the brightness [79].

Preetham et.al provided an algorithm for aerial perspective in addition to the technique for sky modelling [63]. This allows the user to determine the appearance of distant objects with respect to atmospheric conditions like light scattering and turbidity. The spectral distribution of light can also be calculated using Preetham model for all points in the skydome at any point in time. This helps in determining the composition of light at each point in the sky and the utilization of incident light by the object.

A study conducted by Zotti et.al describes certain shortcoming of the Preetham model at certain atmospheric conditions and times of the day [78]. For very clear skies (turbidity<2), the model exaggerates the brightening of horizon at low sun positions. This leads to an orange gradient spread around the skydome, which in reality should only be visible around the sun. At low sun elevations, luminance values are unrealistically high in the antisolar hemisphere where darkening of the sky is otherwise expected. The gradient of luminance hike towards the sun is also noticeably higher than the CIE standard clear-sky models [70], [78].

Despite the drawbacks in Preetham model, the model offers high accuracy and computational speeds to translate the luminance distribution into RGB co-ordinates. The detailed procedure of implementing the Preetham model and the resulting images of the sky will be discussed in the upcoming sections of this chapter.

2.2.3. Hosek-Wilkie Model

In section 2.2.2, the drawbacks of Preetham model were discussed. To eliminate the shortcomings of the Preetham model, an improved sky model was introduced by Hosek and Wilkie in 2012 [67]. Unlike Preetham model, Hosek-Wilkie used reference data created from brute force tracer method. The major improvements include introduction of a separate term ($G\chi$) for simulating Mie scattering, which defines the intensity of circumsolar region (aureole) around the sun. Hosek-Wilkie model also attempts to calculate the absolute luminance using an expected spectral radiance value, instead of relative luminance. The newly introduced coefficient (I) also gives a more realistic depiction of light scattering around the sun near the zenith angle and the horizon. These improvements transformed equation (2.1) presented by Perez et.al into equation 2.2 given below:

$$F(\theta, \gamma) = (1 + Ae^{\frac{B}{\cos\theta+0.01}})(V + Ce^{D\gamma} + E\cos^2\gamma + G\chi(H, \gamma) + I\cos^{\frac{1}{2}}\theta) \quad (2.2)$$

The most significant improvement brought in by Hosek-Wilkie model is introducing a fitting table that takes the effect of turbidity values, albedo values and points on a Bezier curve that parameterizes sun elevation. These fitting tables are created for every wavelength interval or for the three color bands

in CIEXYZ values. In a later study, Hosek and Wilkie added a solar radiance function to the model to calculate and match direct solar radiance with the skylight [66].

Hosek-Wilkie model is proven to be more accurate and produces realistic sky images. But due to the complexity of implementing the model, this study will focus on rendering the sky image and spectrally resolving incident irradiance using Preetham model.

2.3. Implementation of Preetham model in PVMD toolbox

As discussed in section 2.2.3, Hosek-Wilkie model is proven to be more accurate and produces more realistic representation of the sky compared to Perez and Preetham model. Although, considering the complexity of implementing the model, this study will focus on rendering the sky image and spectrally resolving incident irradiance using Preetham model. The following sections and flowchart (Figure 2.3) explain the process followed to incorporate the model into PVMD toolbox and the resulting sky images generated from it.

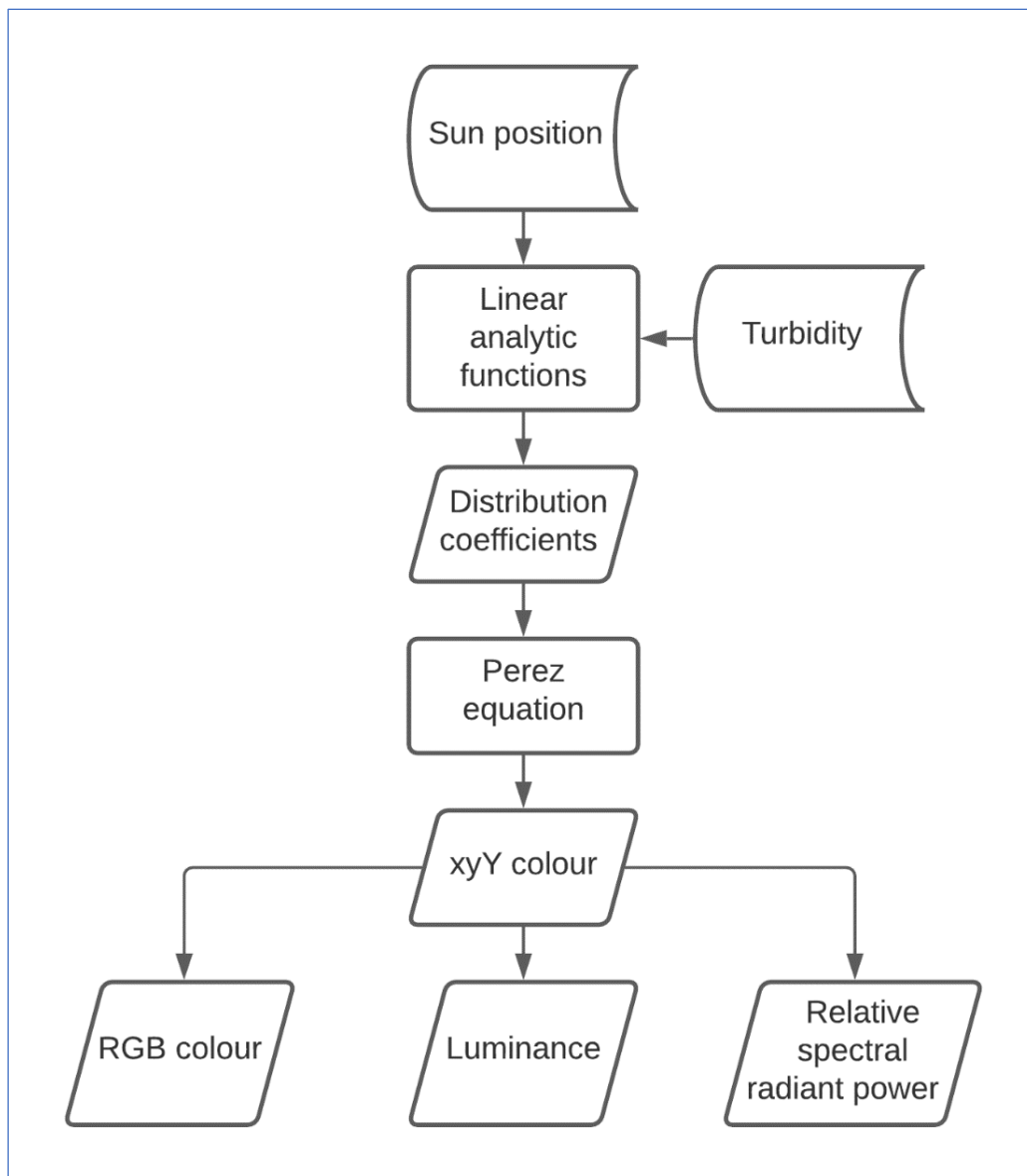


Figure 2.3: Preetham model implementation flowchart

2.3.1. Defined skydome in PVMD toolbox

Sky luminance distribution models are of two kinds: luminance-only models and models that provide both luminance and color information of the sky. Preetham model is a luminance model with color information. It represents the skydome in a hemispherical coordinate system that tracks the sun position and viewing direction with respect to the zenith. The coordinate system is shown in Figure 2.4, where θ_s represents the angle sun makes with zenith, and θ the angle between zenith and viewing direction v . γ gives the angular distance between the viewing direction and the sun.

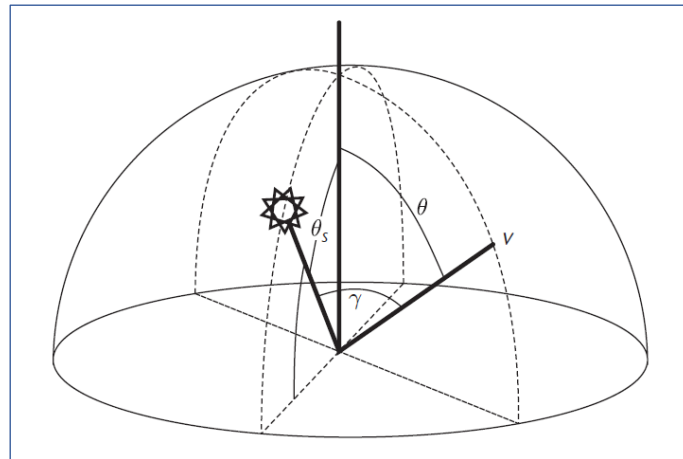


Figure 2.4: Coordinate system of the skydome used in Preetham model [66]

To determine the luminance at every point in the sky, the skydome has to be divided into smaller elements. Using the icosphere algorithm, Dr. Rudi Santbergen of PVMD group implemented this step in the toolbox to create the sensitivity map for solar module and to map calculated incident irradiance data from Perez model [80]. The algorithm allows each triangle on the hemisphere to be divided into 4 smaller triangles upon each recursion. The vertices, faces and position of triangle in the skydome with respect to zenith is extracted from this algorithm.

2.3.2. Distribution coefficients and parametric function

To create the analytic model, Preetham et.al. fits a parametric function to sky spectral radiance function for different turbidity and sun positions [63]. The spectral radiance function was created by Nishita et al. where combinations of simulation were run for different turbidities (2-6), twelve sun positions and 343 points in the sky [68]. The parametrized function for luminance is defined using the Perez formula [60]. While the function represents CIE luminance (Y) variable fairly, it fails to do the same for X and Z variables. Therefore, instead of X and Z, x and y chromaticities are calculated by Perez formula to create a CIE xyY colour representation of the sky, which is widely used to specify colors and their brightness. The five Perez parameters for Y, x and y that are obtained through quadratic functions of turbidity fit using Levenberg-Marquardt non-linear squares method were defined as per the relations given below [63], [70].

$$\begin{bmatrix} A_Y \\ B_Y \\ C_Y \\ D_Y \\ E_Y \end{bmatrix} = \begin{bmatrix} 0.1787 & -1.4630 \\ -0.3554 & 0.4275 \\ -0.0227 & 5.3251 \\ 0.1206 & -2.5771 \\ -0.0670 & 0.3703 \end{bmatrix} \begin{bmatrix} T \\ 1 \end{bmatrix}$$

$$\begin{bmatrix} A_x \\ B_x \\ C_x \\ D_x \\ E_x \end{bmatrix} = \begin{bmatrix} -0.0193 & -0.2592 \\ -0.0665 & 0.0008 \\ -0.0004 & 0.2125 \\ -0.0641 & -0.8989 \\ -0.0033 & 0.0452 \end{bmatrix} \begin{bmatrix} T \\ 1 \end{bmatrix} \quad (2.3)$$

$$\begin{bmatrix} A_y \\ B_y \\ C_y \\ D_y \\ E_y \end{bmatrix} = \begin{bmatrix} -0.0167 & -0.2608 \\ -0.0950 & 0.0092 \\ -0.0079 & 0.2102 \\ -0.0441 & -1.6537 \\ -0.0109 & 0.0529 \end{bmatrix} \begin{bmatrix} T \\ 1 \end{bmatrix}$$

In this study, the sky image is rendered and spectral radiance is calculated for a clear sky. As shown in Figure 2.2, this corresponds to a constant turbidity value of 3. Once the distribution coefficients are calculated, the absolute zenith values for Y, x and y are determined using equations 2.4, 2.5 and 2.6 [63].

Zenith luminance (Kcd/m²):

$$Y_z = (4.0453T - 4.9710) \tan \chi - 0.2155T + 2.4192 \quad (2.4)$$

where $\chi = \left(\frac{4}{9} - \frac{T}{120}\right)(\pi - 2\theta_s)$

Zenith of x:

$$x_z = [T^2 \quad T \quad 1] \begin{bmatrix} 0.00166 & -0.00375 & 0.00209 & 0 \\ -0.02903 & 0.06377 & -0.03202 & 0.00394 \\ 0.11693 & -0.21196 & 0.06052 & 0.25886 \end{bmatrix} \begin{bmatrix} \theta_s^3 \\ \theta_s^2 \\ \theta_s \\ 1 \end{bmatrix} \quad (2.5)$$

Zenith of y:

$$y_z = [T^2 \quad T \quad 1] \begin{bmatrix} 0.00275 & -0.00610 & 0.00317 & 0 \\ -0.04214 & 0.08970 & -0.04153 & 0.00516 \\ 0.15346 & -0.26756 & 0.06670 & 0.26688 \end{bmatrix} \begin{bmatrix} \theta_s^3 \\ \theta_s^2 \\ \theta_s \\ 1 \end{bmatrix} \quad (2.6)$$

Using the distribution coefficients and zenith values for Y, x and y, the CIE xyY values are calculated using equations 2.7, 2.8 and 2.9. The F corresponds to the Perez formula defined in Equation 1 for the sun position and viewing direction.

$$Y = Y_z \frac{F(\theta, \gamma)}{F(0, \theta_s)} \quad (2.7)$$

$$x = x_z \frac{F(\theta, \gamma)}{F(0, \theta_s)} \quad (2.8)$$

$$y = y_z \frac{F(\theta, \gamma)}{F(0, \theta_s)} \quad (2.9)$$

The xyY values thus obtained for a particular sun position is further converted to CIEXYZ and to RGB co-ordinates for rendering the sky image [70].

2.3.3. Rendering the sky image

The CIEXYZ tristimulus values are calculated from xyY using the relation given below (equations 2.10 and 2.11) stated by Poynton et.al [81].

$$X = \frac{x}{y} Y \quad (2.10)$$

$$Z = \frac{1 - x - y}{y} Y \quad (2.11)$$

Y represents the luminance in xyY and CIEXYZ values, and therefore stays the same. To render the sky image, XYZ values rescaled to be in [0,1] range are converted to standard RGB(sRGB) values considering D65 illuminant as the light source. The conversion process from CIEXYZ to sRGB is given below.

$$\begin{bmatrix} R_{linear} \\ G_{linear} \\ B_{linear} \end{bmatrix} = \begin{bmatrix} 3.2406 & -1.5372 & -0.4986 \\ -0.9689 & 1.8758 & 0.0415 \\ 0.0557 & -0.2040 & 1.0570 \end{bmatrix} \begin{bmatrix} X \\ Y \\ Z \end{bmatrix} \quad (2.12)$$

By gamma correction, linear RGB is converted to sRGB values.

$$R_{sRGB} = \begin{cases} 19.92R_{linear} & \text{while } R_{linear} \leq 0.0031308 \\ 1.055R_{linear}^{1/2.4} - 0.55 & \text{while } R_{linear} > 0.0031308 \end{cases} \quad (2.13)$$

$$G_{sRGB} = \begin{cases} 19.92G_{linear} & \text{while } G_{linear} \leq 0.0031308 \\ 1.055G_{linear}^{1/2.4} - 0.55 & \text{while } G_{linear} > 0.0031308 \end{cases} \quad (2.14)$$

$$B_{sRGB} = \begin{cases} 19.92B_{linear} & \text{while } B_{linear} \leq 0.0031308 \\ 1.055B_{linear}^{1/2.4} - 0.55 & \text{while } B_{linear} > 0.0031308 \end{cases} \quad (2.15)$$

The luminance values translated to RGB coordinates for every point of the skydome is then plotted to create the image of the sky for a certain point in time of the year. For a chosen period of time and location, the model allows real-time rendering to visualize the movement of sun across the sky and the distribution of circumsolar light.

2.3.4. Spectrally resolving irradiance

As discussed in section 2.2.2, Preetham model provides the analytical method created by Wyszecki et.al. to convert tristimulus values to relative spectral radiant power [63], [79]. CIE introduced the concept of artificial standard D illuminants to portray spectral light distribution across the world. D-65 illuminant, or daylight illuminant, standardize the spectral power distribution of natural sunlight. Using wavelength-dependent eigen vector functions $S_1(\lambda)$ and $S_2(\lambda)$, a linear relation is defined with mean spectral radiant power $S_0(\lambda)$ to calculate the spectral radiant power of D-illuminants as shown in equation 2.16.

$$S_D(\lambda) = S_0(\lambda) + M_1 S_1(\lambda) + M_2 S_2(\lambda) \quad (2.16)$$

The mean and two eigen vector functions for regular wavelength intervals in the visible spectrum is given in Table 2 of the original study by Preetham et.al [63]. M_1 and M_2 correspond to scalar multiples dependent on the chromaticity values, x and y as shown in equations 2.17 and 2.18.

$$M_1 = \frac{-1.3515 - 1.7703x + 5.9114y}{0.0241 + 0.2562x - 0.7341y} \quad (2.17)$$

$$M_2 = \frac{0.0300 - 31.4424x + 30.0717y}{0.0241 + 0.2562x - 0.7341y} \quad (2.18)$$

For every point in the skydome, the scalar multiples are calculated to further determine the relative spectral radiant power of the illuminant.

2.3.4.1. Solar Spectral model

Upon entry into the Earth's atmosphere, sunlight is attenuated due to absorption and transmittance from atmospheric particles [63], [82]. These may include effect of water vapour, ozone, dust, gases, Rayleigh particles and Mie particles. Preetham model spectrally resolves the extra-terrestrial irradiance to calculate the intensity of sunlight that reaches the Earth's surface using the method introduced by Bird et.al. in 1984 [82]. The study presents a spectral model for direct and diffused irradiance for horizontal and tilted surfaces on Earth. It is created for cloudless skies that includes transmittance functions for ozone and water vapour absorption, aerosol attenuation, Rayleigh scattering, and absorption of uniformly mixed gases for a given wavelength. The spectral model, upon accurate implementation, can be used for validating the illuminance distribution calculated from the sky model for a given hour.

The transmittance from atmospheric particles are calculated using the attenuation coefficients given by Iqbal for wavelength range 300-1200nm. The optical mass (m) dependent on the solar zenith angle is given by equation 2.16.

$$m = \frac{1}{\cos\theta_s + 0.15 * (93.885 - \theta_s)^{-1.253}} \quad (2.16)$$

The direct irradiance falling on a horizontal surface for a given wavelength $\lambda(\mu\text{m})$ is calculated using equation 2.17.

$$I_{dir\lambda} = Irr_{ext} \tau_{r,\lambda} \tau_{a,\lambda} \tau_{o,\lambda} \tau_{g,\lambda} \tau_{wa,\lambda} \cos\theta_s \quad (2.17)$$

where Irr_{ext} is the extraterrestrial irradiance (W/m^2) and transmission functions for Rayleigh scattering, aerosol attenuation, ozone absorption, mixed gases absorption and water vapour absorption are given by $\tau_{r,\lambda}$, $\tau_{a,\lambda}$, $\tau_{o,\lambda}$, $\tau_{g,\lambda}$ and $\tau_{wa,\lambda}$ respectively. The expressions to derive the transmittance functions and approximations used to calculate the same are explained in Appendix B.

The expression by Bird et.al. for diffuse irradiance falling on a horizontal surface is given by equation 2.18.

$$I_{diff\lambda} = I_{r\lambda} + I_{a\lambda} + I_{g\lambda} \quad (2.18)$$

where $I_{r\lambda}$, $I_{a\lambda}$, and $I_{g\lambda}$ refer to the Rayleigh scattering component, aerosol scattering component and ground reflected light component. Separate expressions have been derived for all three terms and the detailed method to calculate them are explained in Appendix A. Due to the complexity of calculation owing to various assumptions, contribution of ground reflected light is ignored.

The PVMD toolbox uses calculated distributed luminance to evaluate the absorbed irradiance on the module. Perez model that is already implemented in the toolbox uses DNI from real-world Meteororm data to calculate luminance distribution. In the original study, Preetham model calculates this factor using the solar spectral model discussed above. Although, due to numerous assumptions and approximations, the calculated DNI is highly inaccurate. The total calculated DNI using spectral model exceeds Meteororm by 12.2% at Rome in 2005. Due to the inaccuracy in spectral model and to minimize the error in implementing Preetham model, in this study, hourly irradiance data is taken from Meteororm to calculate normalized luminance distribution.

2.3.4. Normalizing luminance across skydome

The luminance calculated using Perez formula in equation 2.4 ($F(\theta, \gamma)$) indicates relative luminance at the particular point in the sky. Therefore, distributed light is normalized against diffuse irradiance from Meteororm across the skydome using equation 2.19 to further calculate absorbed irradiance by the module [60]. Upon normalizing, the sum of diffuse irradiance across all points in the skydome sums up to the DHI for the hour.

$$Y = F(\theta, \gamma) * \frac{DHI}{\int_0^{2\pi} \int_0^{\pi} F(\theta, \gamma) * \cos(\gamma) * d\omega} \quad (2.19)$$

where ω : area of considered sky element

2.4. Results from Preetham daylight model

The rendered images of the sky and the relative spectral power distribution calculated from the newly implemented Preetham model are compared with Perez model. The comparisons are made for selected hours of the year using weather data taken from Meteonorm for Rome in Italy.

2.4.1. Sky image

The sky images rendered for three times of the day for May 1 using Preetham and Perez models are shown in Figure 2.5. The results from Perez model are represented as greyscale since the image is not plotted using RGB co-ordinates. The circumsolar light and the scattered light around the sun is described distinctly in the Preetham image, when compared to Perez model. During sunrise and sunset, since light has to pass through larger distance to reach the human eye, light of lower wavelength is scattered around before reaching the human eye. This explains the red/orange gradient around the sun and sky as sun approaches the horizon. During this moment, the gradient spreads across the horizon as well. But the Preetham model exaggerates the luminance of this phenomenon as mentioned in section 2.2.2.

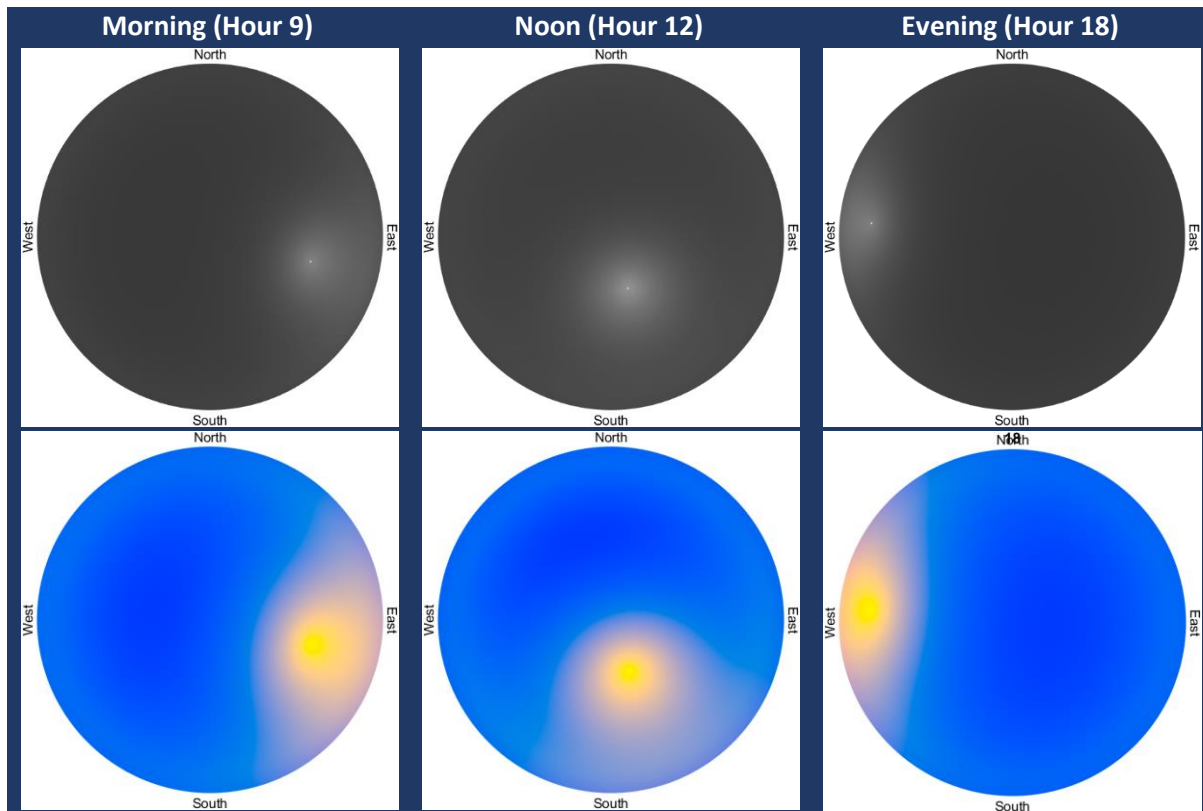


Figure 2.5: The sky images rendered using Perez and Preetham models for three times of the day on May 1, 2005 in Rome, Italy (Turbidity fixed at 3). Note that Perez model plots scalar brightness values and Preetham model plots RGB vector co-ordinates.

The change in position of the sun across the skydome throughout the year is illustrated in Figure 2.6. Here, azimuth of the module is facing the south as the location considered is in the northern hemisphere. For a location in southern hemisphere, position of the sun would move to the upper part of the skydome. Around mid-year, the angle of sunlight reaching the module is more direct than in the beginning and end of the year. As shown in Figure 2.5, this also signifies longer daylight hours, thus

contributing to higher irradiance intensity during summer when compared to other times of the year. While Figure 2.6 plots for the same hour at the start of every month, analemma of the sun can be obtained when the sun position is plotted for every day of the year at the fixed time. By plotting this, for a particular location, the intensity of vertical sunlight received by the module for a certain day can be visualized [83].

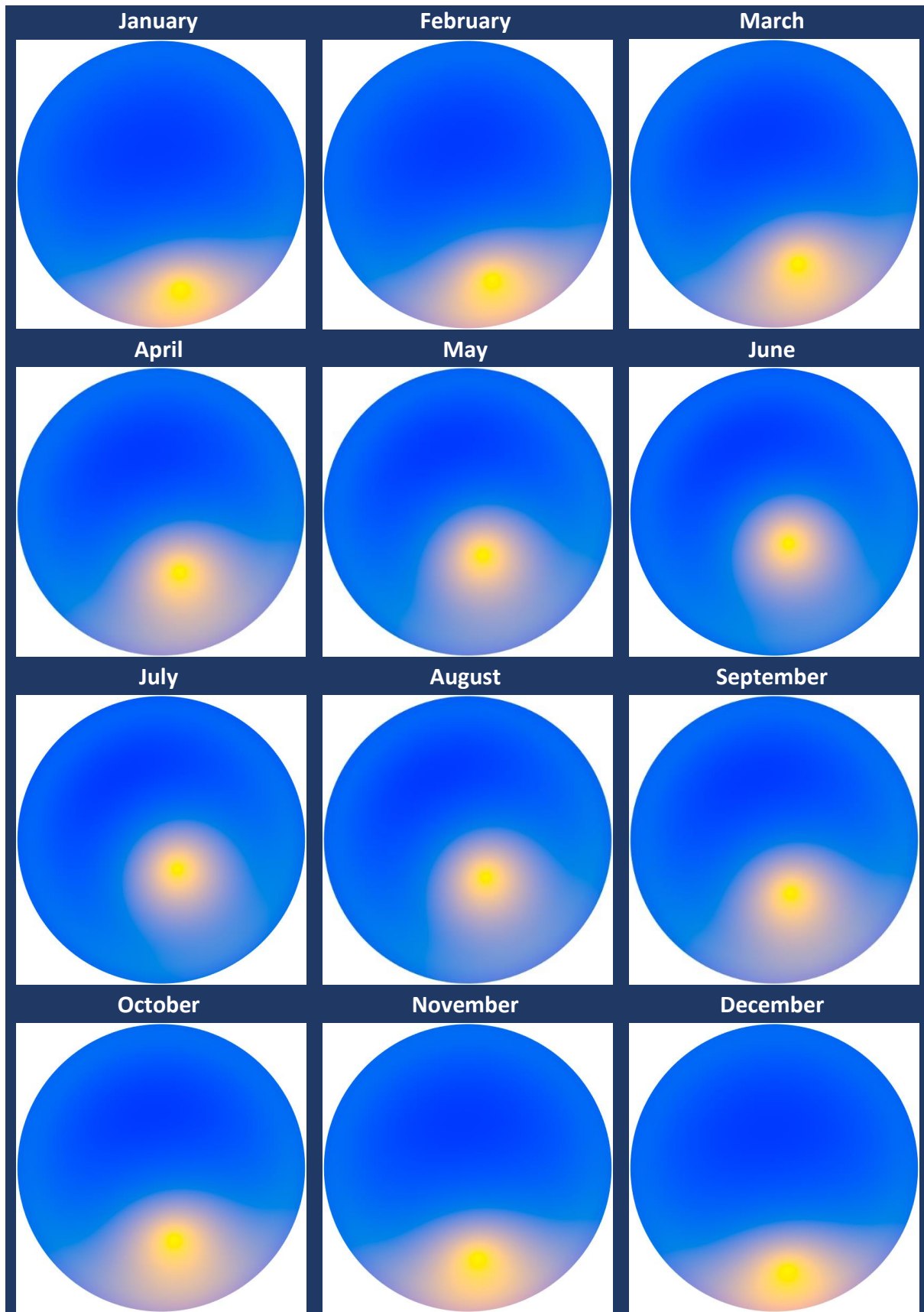


Figure 2.6: The sky images for Day 1 hour 12 for every month of the year in Rome, Italy.

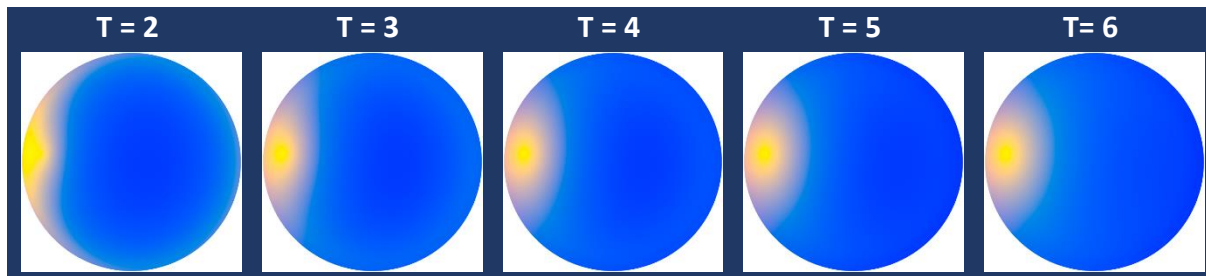


Figure 2.7: Effect of turbidity during sunset on May 1 at Rome, Italy.

Preetham model evaluates Perez coefficients using sky spectral radiance function simulated for turbidities between 2 and 6. Figure 2.7 illustrates the effect of turbidity at a fixed time in Rome. As turbidity increases from 2 to 6, the light is scattered away from the horizon and towards the zenith giving an orange color to the sky. Beyond turbidity of 6, the images rendered are unrealistic. At higher turbidities indicating severe weather conditions as shown in Figure 2.2, a reddish hue is expected around the sun due to light scattering from larger atmospheric particles. Although, to visualize this, reference data for a larger turbidity range must be utilized.

2.4.2. Relative spectral power distribution

The power distribution of incident light across the visible spectrum for a particular point in sky is normalized and compared against standard relative spectral power (RSP) and AM spectrum. The data for D65 illuminant was obtained from Hunt et. al [84]. It is to be noted that the power distribution calculated for Perez model is an interpolated dataset depending on the air mass for the hour.

To understand the variation in spectral power across the skydome, three triangular areas are chosen on the skydome as shown in Figure 2.8. For Hour 12 (noon) on May 1 in Rome, the power distribution across the spectrum for the three areas are evaluated and compared against the hourly AM spectrum as calculated for current irradiance model and the standard D65 illuminant.

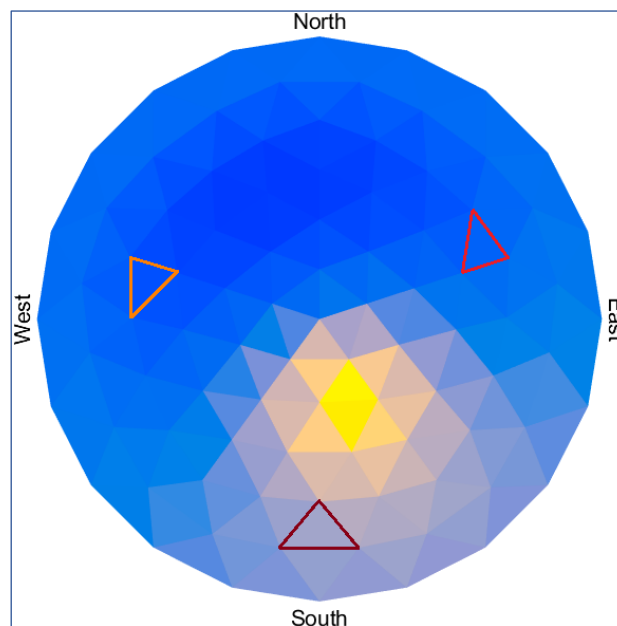


Figure 2.8: Three areas over the skydome to calculate relative spectral power. Triangle 1: towards East; Triangle 2: towards South; Triangle 3: towards West.

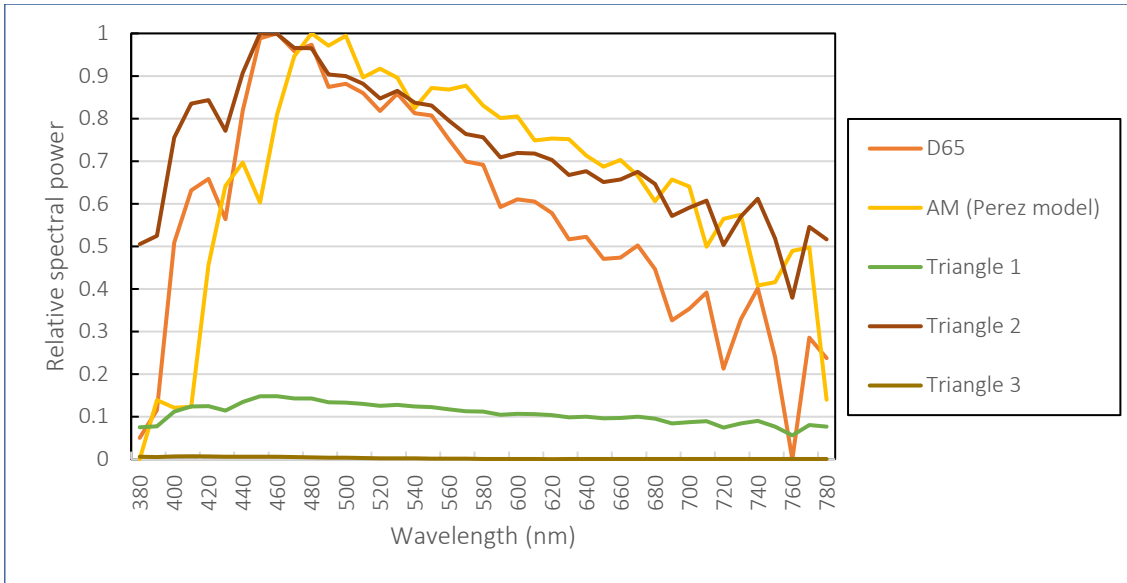


Figure 2.9: The relative spectral power distribution for three points in skydome at noon of May 1 in Rome, Italy. The AM (Perez model) refers to AM 1.13 (calculated air mass)

Out of the three areas chosen, triangle 2 has the highest relative power intensity and matches closely with the power distribution of D65 illuminant. This agrees with the expectation since at noon on May 1, the area chosen is very close to actual position of the sun. Triangle 1 near East and triangle 3 near West have lower intensities compared to the second one since their positions are much further away from the sun. Although more evident in the distribution of triangle 2, the other two triangles also show higher power in 430-500 nm wavelength range (violet/blue range) when compared to the orange/red region. At noon, due to the shorter distance that light travels to reach the human eye, the higher wavelength colors are more prominent. However, due to Rayleigh scattering which is inversely proportional to λ^{-4} , the scattered blue light reaching human eye contributes to more relative power than from higher wavelength region.

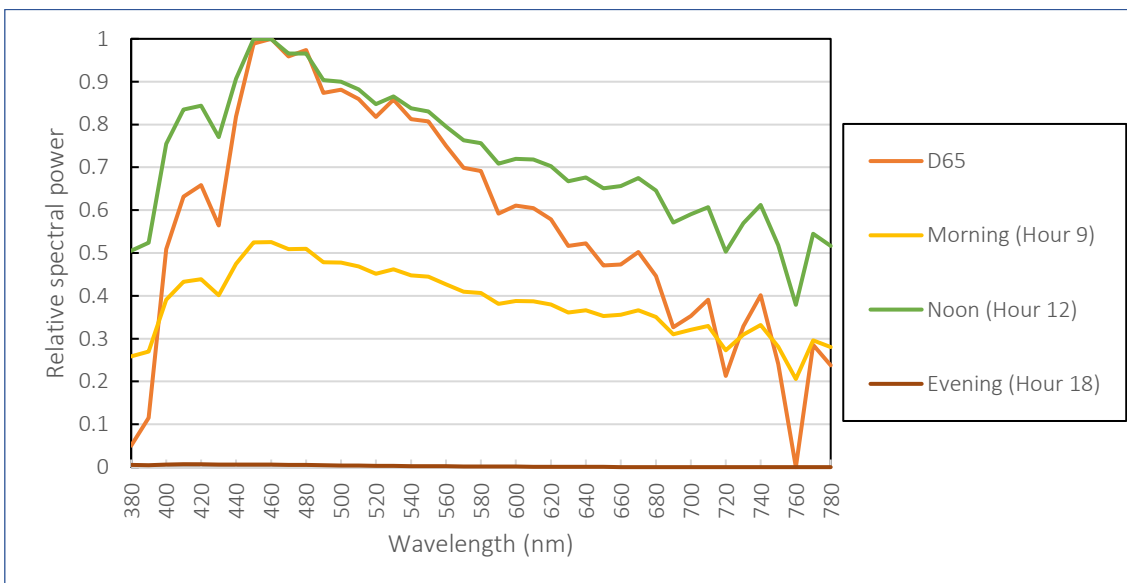


Figure 2.10: The relative spectral power distribution at triangle area 2 as shown in Figure 2.7 for three times of the day on May 1 in Rome, Italy

While considering a fixed point on the skydome for three times of the day, the variation in power distribution with time is even more evident. Figure 2.10 shows the spectral power distribution on triangle area 2 for morning, noon and evening of May 1 in Rome. At noon, the power intensity exceeds the standard illuminant since the point is very close to the sun. The contribution from circumsolar light and the closer distance to the sun gives the point close to half of the relative power distributed across the spectrum. As time moves towards the sunset, the point in consideration is farther away from the sun to only receive scattered blue/violet light of the spectrum.

2.5. Conclusion

This chapter describes the implementation method of Preetham model in the PVMD toolbox. Implementing the model allows the user to accurately determine the energy yield of photovoltaic modules in real-world conditions, which will be further discussed in Chapter 4. By implementing the model, three aspects are determined: luminance distribution, RGB co-ordinates and relative spectral power (RSP) distribution at every point on the skydome. Compared to Perez model currently used in the toolbox, Preetham model renders real-time image of the sky for every hour in chosen time-frame. Calculating RSP distribution gives a better understanding of the spectrum available for utilization from all directions of the sky, which deems useful during the cell and system level design of tandem solar modules. By realizing Preetham model in PVMD toolbox, the first objective of this thesis is achieved.

3

ELECTRIC: Parameter extraction from J-V curves

This chapter describes the development of parameter extraction model for ASA-simulated J-V curves in PVMD toolbox. For a tandem cell structure, the electric performance of top and bottom cells are determined using these extracted parameters from J-V curves simulated at varied operating conditions. By developing this model, the second objective of this thesis is addressed. Section 3.1 introduces the diode models widely used to represent electric circuit in solar cell. The top and bottom cells that form the tandem cell structure is explained in section 3.2. The method used to simulate J-V curves using the in-house built ASA software is described in section 3.3. Section 3.4 gives the step-by-step procedure used to extract parameters from J-V curves. The developed model is validated in section 2.5 before concluding the results from the study in section 2.6.

3.1. Introduction: Diode Models

Performance of a solar cell is usually represented at Standard Test Conditions (STC). However, real world conditions could vary significantly from STC. To predict the electric output of a solar cell and to create their J-V curves, parameters that define their characteristics need to be simulated at various operating conditions. Equivalent circuit models represent the overall behaviour of a cell using the aforementioned parameters. One and two-diode models are the commonly used circuit models that simulate photovoltaic behaviour of solar cells at various irradiance and temperature conditions [1-10]. While one-diode model is easier to implement, two-diode model is more complex but accurate [95].

The main methods followed for extracting parameters from equivalent circuits of PV modules are numerical, curve-fitting, and analytical [96]. Numerical method creates a set of equations that are solved using an iterative algorithm at certain operating points on the J-V curve. Usually, the points taken on the curve to create the equations are short-circuit, open-circuit and maximum power point regions. Newton-Raphson method and Levenberg-Marquardt are few of the commonly used techniques to calculate the parameters numerically. Although, the accuracy of numerical method largely depends on the chosen initial value of the parameter [97].

Least-squares fitting method is used for curve-fitting where all points on the J-V curve are taken into consideration for parameter calculation. The Genetic Algorithm (GA), harmony search-based algorithms, Particle Swarm Optimization (PSO), and Bird Mating Optimizer (BMO) are heuristic approaches to extract parameters from J-V curves. Other heuristic algorithms used for parameter extraction are studied and compared by Hachana et.al [97].

The numerical and curve-fitting methods face uncertainty in calculation and contribute to high computational load and complexity. Analytical method calculate parameters based on physical assumptions and determine the parameters explicitly. Certain methods neglect series and shunt resistances, while other methods assume series and shunt resistances to be the slope of I-V curve at

the open-circuit and short-circuit regions respectively. The computational load of using analytical method is comparatively lesser while calculating parameters at acceptable accuracy [96].

Due to simplicity and fairly good fit with experimental I-V curves, in this study, the five-parameter single diode model will be used to extract parameters from I-V curves using an analytical method.

3.1.1. Five-parameter single diode model

For given operating conditions, equivalent circuit defines the entire J-V curve's characteristics for a solar cell, module or array [98]. The single diode model is represented by an equivalent circuit (Figure 3.1) and an implicit equation which gives the relation between output voltage (V) and current (I) of the circuit as shown in equation 3.1.

$$I = I_{ph} - I_0 \cdot \left\{ \exp \left(\frac{q(V + IR_s)}{nk_B T} \right) - 1 \right\} - \frac{V + IR_s}{R_{sh}} \quad (3.1)$$

The implicit equation composes of five parameters: I_{ph} , I_0 , R_s , R_p and n . The terms used in the equation are explained below:

I_{ph} : Photogenerated current, which indicates the current generated from electron-hole pairs using energy from absorbed photons (A/m^2)

I_0 : Saturation current shows the sum of currents of all recombination mechanisms in the emitter of a cell (A/m^2) [99]

R_s : Series resistance arise from the ohmic losses in the bulk of the cell and contact resistances in the front and back contacts [100]

n : Ideality factor (dimensionless)

k_B : Boltzmann constant ($1.3806E-23$ J/K)

q : Electron charge ($1.602E-19$ C)

T : Cell temperature (K)

R_{sh} : Shunt resistance arises from current leakages which could be caused by crystal defects and cracks in the cell [101]

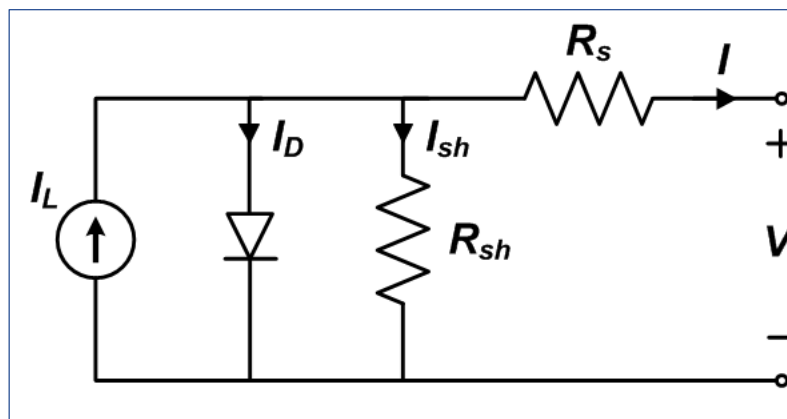


Figure 3.1: Equivalent circuit of single-diode model for single solar cell [98]

Changing irradiance and temperature impact the parameters of a solar cell. Therefore, to analyze the behaviour of the cells for various operating conditions, the parameters will be extracted from J-V curves simulated at pre-determined temperatures and irradiances to further model the solar cell.

3.2. About the cells

3.2.1. Silicon Heterojunction cell

The SHJ cell used in this study is referred from Kobayashi et.al with an efficiency of 22.2% [102]. The cell comprises of a n-type c-Si wafer stacked between a-Si:H i/p layers in the front and a-Si:H i/n layers at the back. The cell also consists of a SnO₂ layer at the front and back of the cell that acts as a transparent conductive oxide (TCO). To reduce the surface reflectance of the cell, SiN layer is deposited in the front before the glass layer. It is to be noted that certain parameters of the cell were optimized by Carlos Ruiz Tobon, Postdoc at PVMD group for higher short-circuit current. This could lead to minor changes in the power conversion efficiency of the solar cell. Structure of the cell and the J-V curve at STC is given in Figure 3.2.

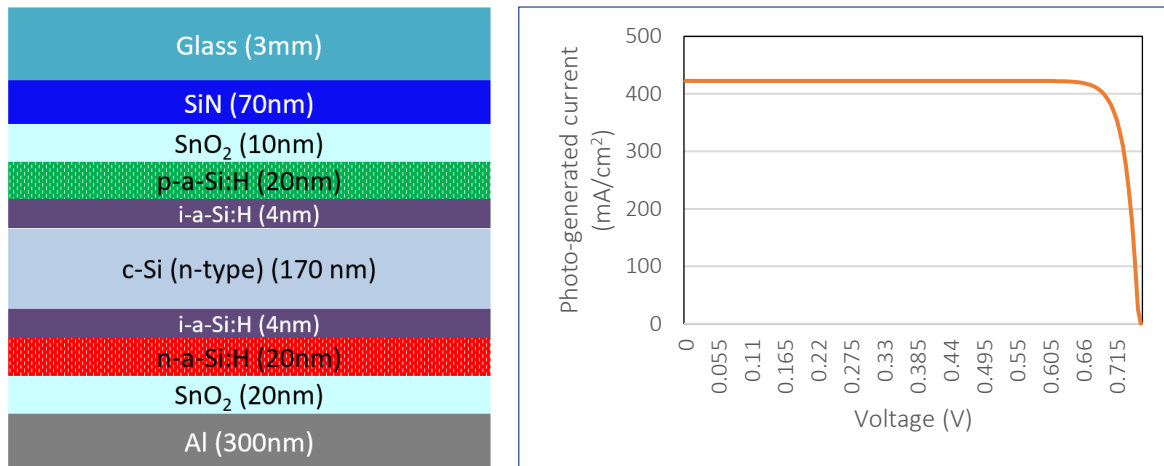


Figure 3.2: Cell structure (left) and J-V curve at STC (right) of SHJ cell

3.2.2. Perovskite solar cell

The perovskite solar cell used in this study is referred from Nayfeh et.al and Murata et.al with an efficiency of 15.4% [103], [104]. Similar to SHJ cell, the parameters for perovskite have been optimized too before simulating in ASA to achieve higher short-circuit current. At the front, the cell consists of SnO₂ layer on top as an anti-reflective coating. TiO₂ layer acts as an electron-transport layer in front of the CH₂NH₃PbI₃ perovskite absorber. Spiro-OMeTAD is deposited in the back of the absorber which acts as the hole-transport material for the perovskite solar cell. The cell is deposited on Ag metal and is protected by glass at front.

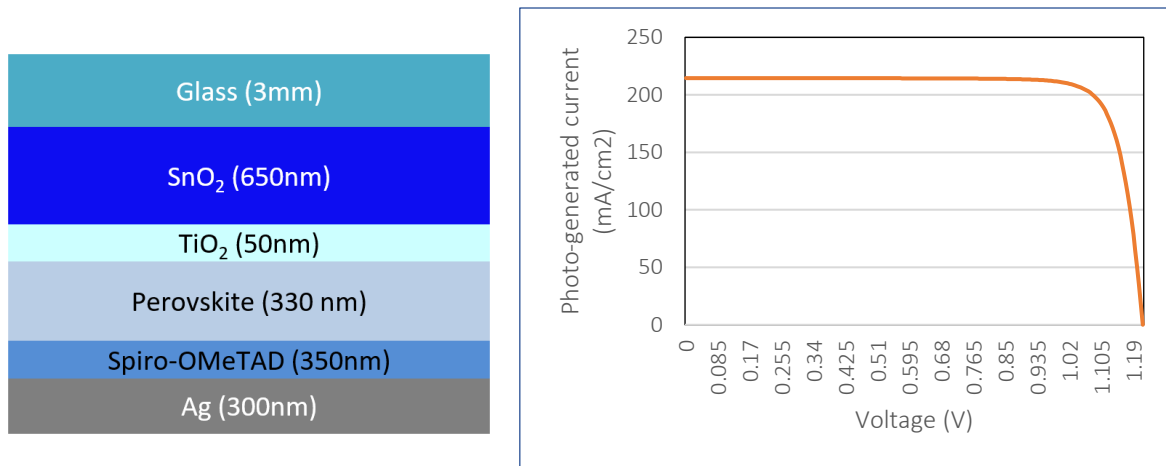
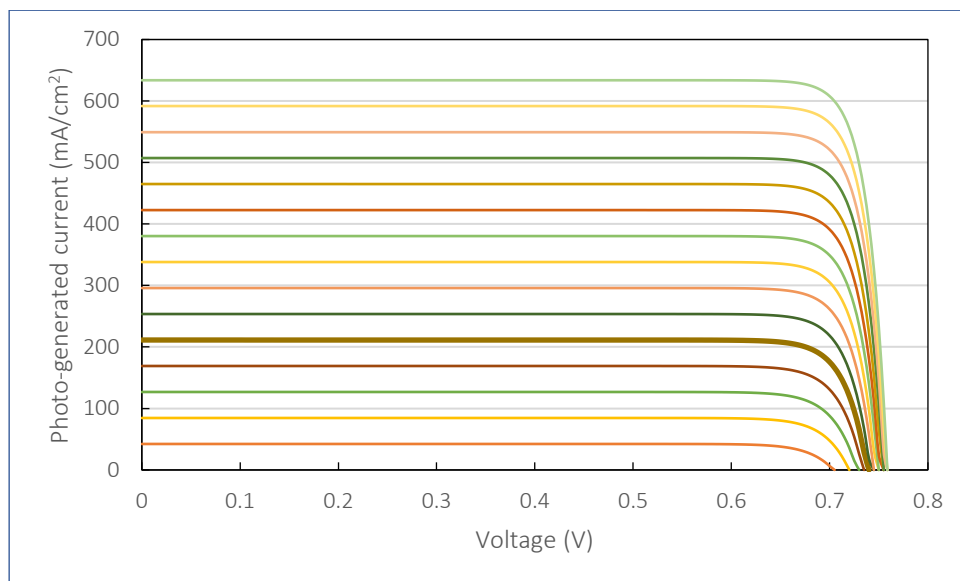


Figure 3.3: Cell structure (left) and J-V curve at STC (right) of perovskite cell

3.3. ASA curves for parameter extraction

The J-V curves of the solar cells in study are simulated using the in-house developed Advanced Semiconductor Analysis (ASA) software. ASA is a one-dimensional optoelectronic device simulator that solves semiconductor equations for amorphous and crystalline semiconductors using concentration of free electrons and holes and electrostatic potential as variables [56], [64]. To simulate behaviour of the cells at different operating conditions, two variables are considered: irradiance and temperature. While one of the variables is fixed at STC, the other is changed to maximize the set of operating conditions at which the J-V curves are simulated. While irradiance is fixed at STC ($1000\text{W}/\text{m}^2$), 12 simulations were run for temperatures between 250K and 360K at regular intervals. Similarly, by fixing the temperature at 298.15K, irradiance was varied between $100\text{W}/\text{m}^2$ and $1500\text{W}/\text{m}^2$ at equal intervals to run 16 simulations. The irradiance intensity was varied by scaling the AM 1.5 spectrum. Figure 3.4 shows the curves obtained from ASA for the SHJ cell from the simulations. These curves are the input for parameter extraction model.



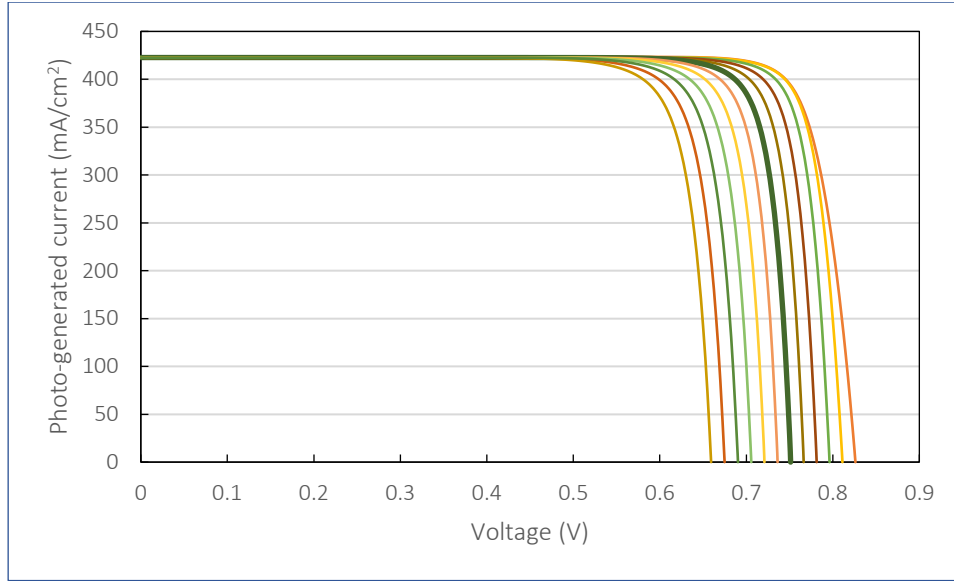


Figure 3.4: The J-V curves simulated from ASA for SHJ cell at different irradiances (top) and different temperatures (bottom). The thicker curves represent J-V curve at STC.

3.4. Parameter extraction method

The step-by-step process of solving the implicit equation used in the model to extract the five parameters of single-diode equivalent circuit is explained in this section. The model implemented using this analytic method takes certain approximations for parameters like series resistance, shunt resistance and photo-generated current. Therefore, besides introducing the model in this study, the calculated parameters are corrected to minimize the deviation of curves reconstructed using the parameters from ASA J-V curves. Flowchart in Figure 3.5 illustrates the parameter extraction method.

Photo-generated current density: The one-diode model equivalent circuit equation reduces to equation 3.2 at short circuit region:

$$J = J_{ph} - \frac{V + J \cdot R_s}{R_{sh}} \quad (3.2)$$

Rearranging the equation, we get

$$J = \frac{J_{ph} \cdot R_{sh} - V}{R_{sh} + R_s} \quad (3.3)$$

When compared to shunt resistance, series resistance is non-significant. Since voltage is zero at short-circuit, short-circuit current density is assumed to be same as photo-generated current density as given in equation 3.4:

$$J_{sc} = \frac{J_{ph} \cdot R_{sh}}{R_s + R_{sh}} \approx J_{ph} \quad (3.4)$$

Shunt resistance: According to literature, the shunt resistance can be approximated as the inverse slope of J-V curve at the short-circuit region [105]. Therefore we get equation 3.5.

$$\left. \frac{dJ}{dV} \right|_{J=J_{sc}} = -\frac{1}{R_s + R_{sh}} = -\frac{1}{R_{sh}} \quad (3.5)$$

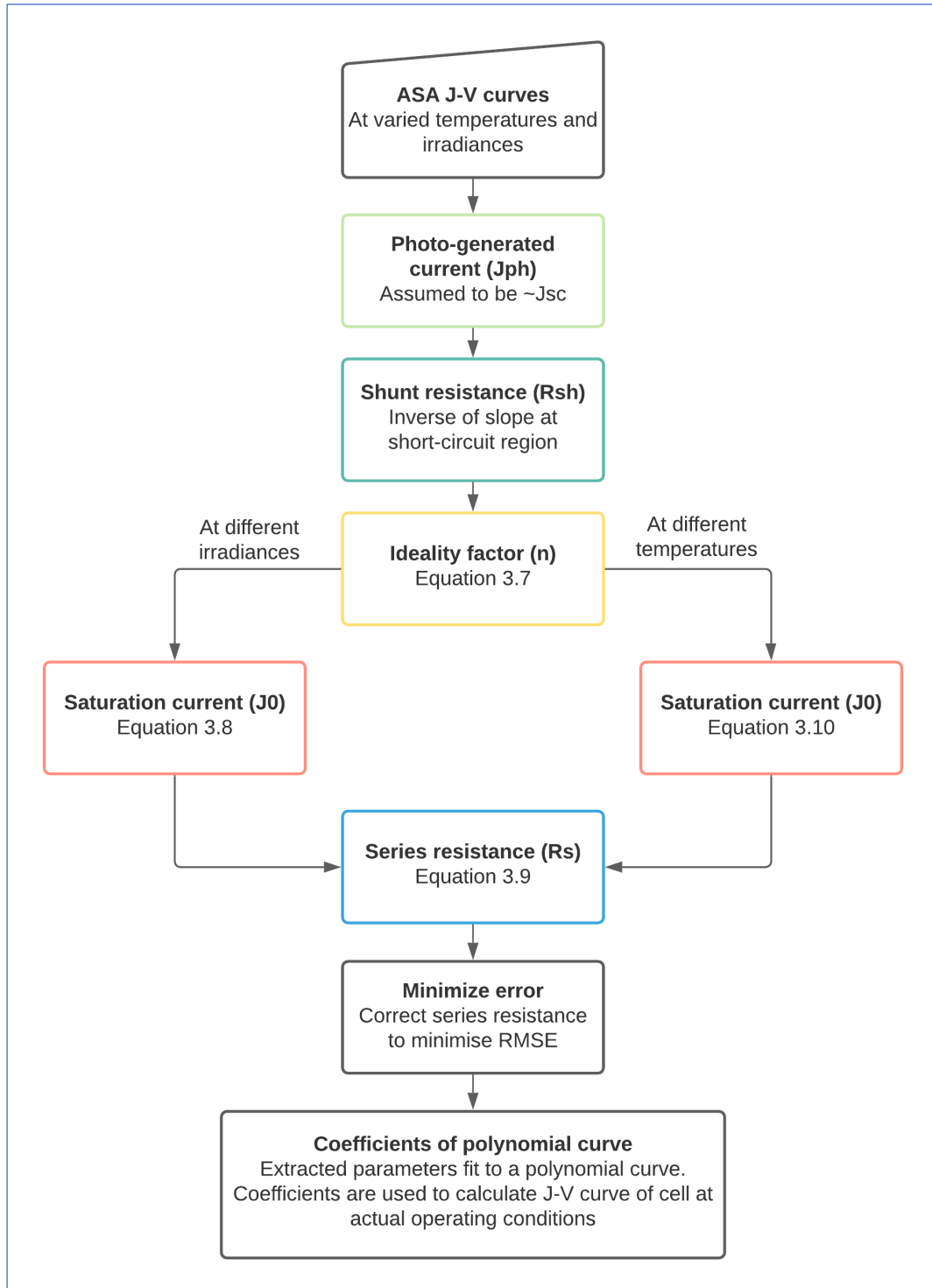


Figure 3.5: Process diagram to extract cell parameters from implicit equation representing five-parameter single diode model

Ideality factor: Change in irradiance have large impact on ideality factor. To calculate saturation current density and ideality factor, Meyer et.al discusses a method where the diode equivalent circuit equation is considered at open circuit point [106]. The implicit equation at V_{oc} becomes

$$V_{oc} = \frac{nk_B T}{q} \ln \left(\frac{J_{sc}}{J_0} \right) \quad (3.6)$$

Rearranging the above equation to express ideality factor gives equation 3.7.

$$n = \frac{q}{k_B T} \cdot \frac{dV_{oc}}{d(\ln J_{sc})} \quad (3.7)$$

The natural logarithmic values of J_{sc} at every irradiance intensity is interpolated to search points indicated by the V_{oc} values. The gradient of the resulting curve between $\ln(J_{sc})$ and V_{oc} gives the ideality factor.

Saturation current density: Similar to ideality factor, the saturation current density is also calculated at the open circuit voltage region [31]. Simplifying the implicit equation for the condition and rearranging, we get equation 3.8:

$$J_0 = \frac{J_{ph}}{\left[\exp \left(\frac{q \cdot V_{oc}}{n \cdot k_B \cdot T} \right) - 1 \right]} \quad (3.8)$$

Saturation current is calculated for every irradiance intensity using the corresponding photo-generated current, previously calculated ideality factor and open-circuit voltage.

Series resistance: The slope of J-V curve near the open circuit voltage region gives series resistance [105]. This can be expressed as equation 3.9.

$$\left. \frac{dJ}{dV} \right|_{V=V_{oc}} = -\frac{1}{R_s} \quad (3.9)$$

The procedure explained above calculates parameters from J-V curves at different irradiances. Besides saturation current density and ideality factor, all other parameters can be calculated similarly from J-V curves at different temperatures. Saturation current density varies significantly with temperature. Therefore, Baruch et.al developed the procedure to calculate saturation current dependent on temperature [107]. The relation is given by equation 3.10.

$$J_0 = \frac{q}{k_B} \frac{15\sigma}{\pi^4} T^3 \int_u^\infty \frac{x^2}{e^x - 1} dx \quad (3.10)$$

where $u = \frac{E_g}{k_B T}$ and σ is Stefan-Boltzmann constant.

E_g indicates the bandgap of material that is dependent on temperature. For c-Si and perovskite cells, the relation is given by equations 3.11 and 3.12 [108] [109]. The bandgap relation for perovskite of

the form $\text{CH}_3\text{NH}_3\text{PbI}_3$ stabilized with PMMA is used here, and is assumed to follow the same behaviour as the perovskite used in this study.

$$E_g(T) = 1.12 - 2.3 (T - 300) * 10^{-4} \quad (3.11)$$

$$E_g(T) = E_g(T_0) - 4.1376 (T - T_0)^2 * 10^{-7} \quad (3.12)$$

Using the `polyfit()` function in MATLAB®, a polynomial curve with the best fit is determined between the calculated parameters and varying operating condition (temperature or irradiance) at which they are calculated [110]. The coefficients of the polynomial of that best fits the data represents the behaviour of the cell parameter at select operating conditions. These are used as reference to calculate the parameters at other operating conditions that the module is exposed to using Calibrated Lumped Element Model and operation condition coupling method developed in the previous study [56].

3.5. Model validation

Previous study by Nour el Din implemented a parameter extraction model for simulated J-V curves of solar cells [18]. The parameter behaviour obtained from the model was compared with observations from literature to analyze their accuracy. Although the J-V curves extracted from ASA and calibrated lumped element model (CLEM) were also measured and analyzed at a later stage in the electric model, the accuracy of parameter extraction model alone was not quantified. Therefore, in this study, the analytical model used to extract parameters from ASA-simulated J-V curves will be validated for their accuracy.

The analytical method involves certain assumptions while calculating the parameters, for example, while approximating shunt resistance as the negative inverse slope of J-V curve at the short circuit point. The extracted parameters are used to create the cell's J-V curve using the single-diode model equation while matching with the simulated J-V curve from ASA. Therefore, corrections are made to the approximated parameters to minimize the error between the simulated and calculated J-V curves.

The reconstructed J-V curve of SHJ and perovskite cells using extracted parameters from irradiance-varied ASA-simulated J-V curves at STC is shown in Figure 3.6. For the considered voltage range, the Root Mean Square Error (RMSE) is observed to be 1.98% and 3.02% for SHJ cell and perovskite cell respectively. Due to the inaccuracy in calculating series resistance, for higher voltages, the error between calculated and simulated J-V curves is comparatively high. RMSE between ASA and simulated curves of SHJ and perovskite cells for all irradiances and temperatures in consideration are shown in Figure 3.7. Series resistance notably have significant influence on the maximum power output of a cell exposed to varying irradiance [111]. Therefore, due to the approximations in series resistance, for higher irradiance, the re-constructed J-V curve deviates from its corresponding ASA curve.

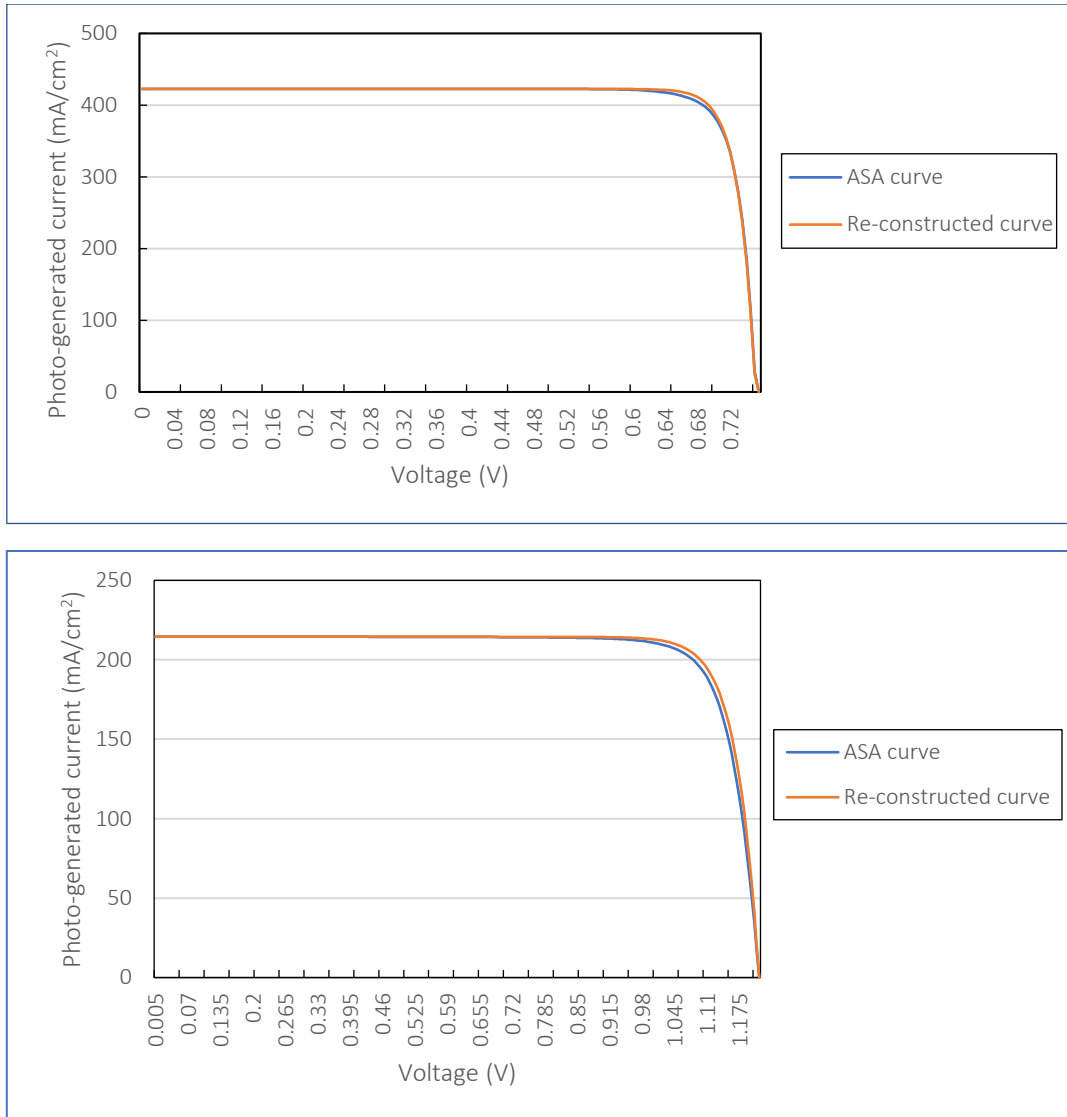
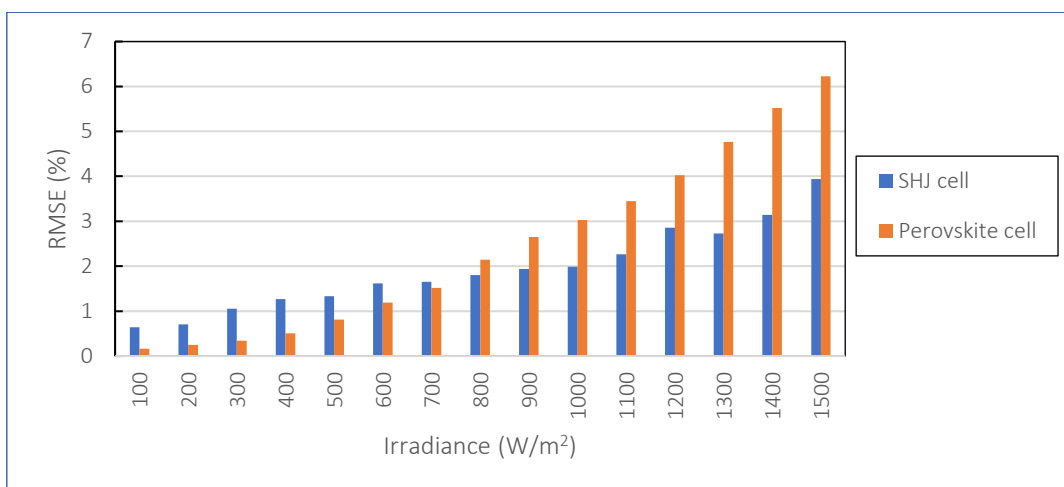


Figure 3.6: The reconstructed and simulated J-V curves for SHJ cell (top) and perovskite cell (bottom) at STC conditions



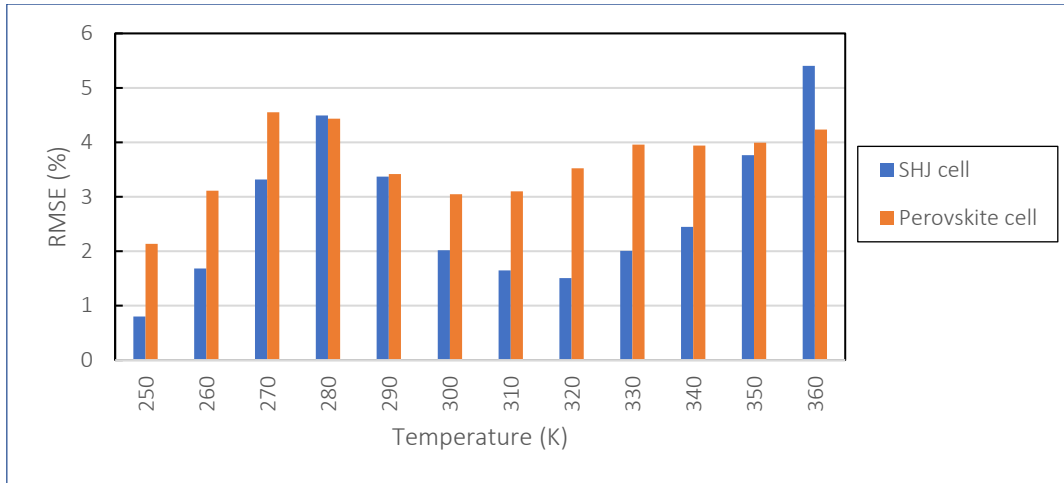


Figure 3.7: RMSE between reconstructed and simulated ASA J-V curve of SHJ cell and perovskite cell at different irradiance intensities (top) and at different temperatures (bottom)

As mentioned before, a variation in series resistance was found to have large impact on accuracy of the model. Using the other parameters and simulated photo-generated current from ASA as reference, series resistance is re-calculated through the single-diode equivalent circuit equation. The curves were re-constructed using corrected series resistance value with a RMSE as shown in Figure 3.7. Although the deviation is not large, further improvements in the model can improve the accuracy. The dependence of extracted parameters on irradiance and temperature for both SHJ and perovskite cells are illustrated in Appendix C.

3.6. Conclusion

The electric behaviour of solar cells at varying operating conditions are simulated to calculate energy yield of the module in real-world conditions. The electric behaviour of cell is determined by extracting parameters of J-V curves of cell(s) that forms the solar cell structure. This chapter addresses the second objective of this thesis: Implement parameter extraction model for simulated J-V curves. Implementing this analytic model allows PVMD toolbox to extract parameters of any cells that form the solar module. Apart from introducing the model, it was further improved by correcting the series resistance to minimize error between ASA J-V curves and J-V curves reconstructed using extracted parameters, thus validating the model. For the perovskite and SHJ cells used in this study, at STC, the RMSE between ASA-simulated J-V curves and reconstructed curves were calculated at 3.02% and 1.98% respectively. The energy yield calculated using these extracted parameters will be studied in Chapter 4.

4

Energy yield analysis of photovoltaic modules

This chapter answers the final objective of this thesis: evaluate and analyze the energy yield of photovoltaic modules using PVMD toolbox. The daylight model newly introduced into the toolbox and parameter extraction model will be utilized to accurately determine the energy yield of tandem modules in real-world conditions.

The tandem cell structures created from the sub-cells are explained in section 4.1. Section 4.2 describes the step-by-step method of calculating the annual energy yield of a module placed at a certain location using the toolbox. Three locations where the yield of modules are determined are introduced in this section. Parameters like top and bottom cell thicknesses, albedo and location are varied to study their effect on the energy yield of the modules in consideration. The results of the analysis are discussed in section 4.4 before discussing the findings from this chapter in section 4.5.

4.1. Tandem cell structures

The concept of tandem solar cell technology and cell configurations were introduced in Chapter 1. In this study, encapsulated mono-facial and bi-facial perovskite/c-Si tandem modules are studied at monolithically integrated 2T and mechanically stacked 4T configurations. The tandem structures illustrated in Figure 4.1 are created using SHJ and perovskite sub-cells discussed in section 3.2. Due to large parasitic absorption losses, the thickness of SnO₂ layer was reduced to maximize photo-current density of tandem cells [112]. The top and bottom cells in 4-terminal tandem cells are separated by Ethylene-vinyl acetate (EVA) layer [25], [113], [114]. Although it is challenging to fabricate textured perovskite cell on glass in 4T configuration, to maximize photo-generated current, we simulate tandem cells with textured perovskite layer [25]. Perovskite thickness is considered a variable that is optimized depending on location for 2T tandem devices. The optimized thickness will be discussed further in section 4.3.

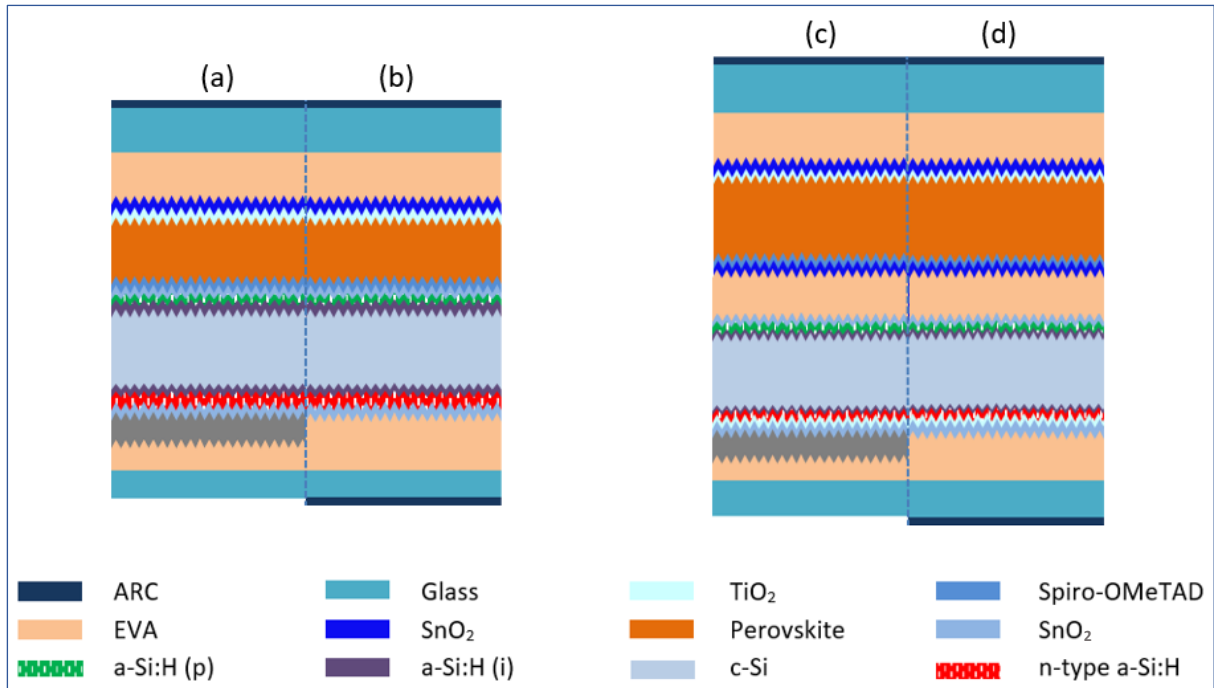


Figure 4.1: Simulated perovskite/c-Si tandem cell structures for (a) encapsulated mono-facial 2T (b) encapsulated bi-facial 2T (c) encapsulated mono-facial 4T and (d) encapsulated bi-facial 4T configurations

4.2. Energy yield calculation in toolbox

Chapter 1 introduces the structure of PVMD toolbox. Each model simulates characteristics of the photovoltaic technology to determine energy yield of the module in real-world conditions. To illustrate the working of PVMD toolbox, annual energy yield (AEY) of bi-facial 2T perovskite/c-Si tandem module at Rome is calculated as follows:

Cell model: As introduced in section 1.6.1, optical properties of the cell are simulated using GenPro4. The simulation is performed at STC by integrating the absorbed photons over AM 1.5 spectrum. The output of cell model are reflectance (R), absorptance (A), transmittance (T) and implied photocurrent densities of all layers of the simulated cell structure. Optical properties of bi-facial tandem cells can also be simulated considering the illumination received from rear side of the cell (Figure 4.2). For mono-facial 2T tandem cells, the photocurrent densities of perovskite and c-Si absorber layers are current-matched at 20.5 mA/cm^2 by tuning the perovskite layer thickness to 310 nm. Although, the optimum perovskite layer thickness varies with location and the corresponding spectrum of incident light received by the tandem cell. This will be discussed further in the section 4.3.

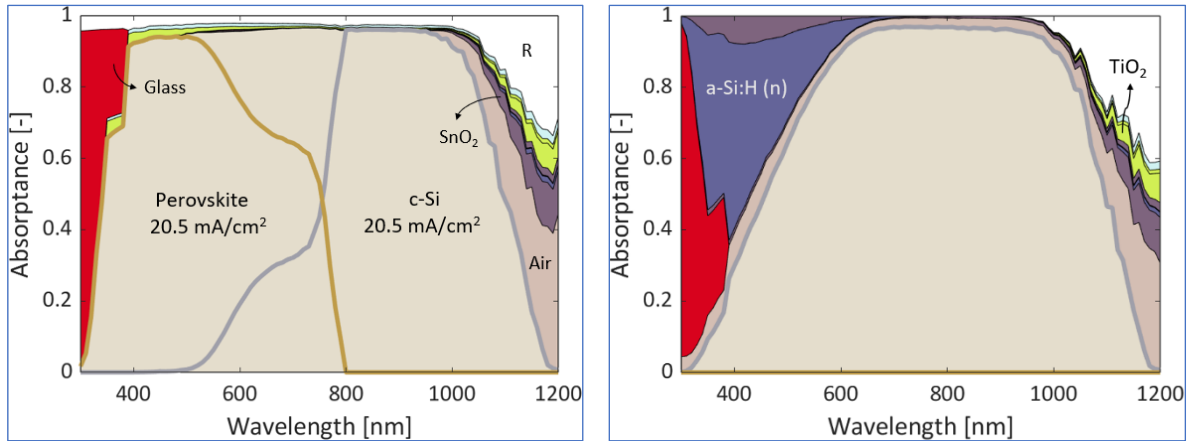


Figure 4.2: Absorbance and reflectance of 2T bi-facial perovskite/c-Si tandem cell under STC for front side (left) and rear side (right) illumination

Module model: In this study, the modules consist of 72 cells arranged uniformly across 10 rows. The geometry of the simulated module are default values set in PVMD toolbox as shown in Appendix D. Tilt of the module is set to its optimum value depending on the chosen location. The module is south-facing (module azimuth = 0°) or north-facing (module azimuth = 180°) if the module is located in the northern or southern hemispheres respectively. The plane of array irradiance is simulated using ray-tracing method at different incident angles to create a sensitivity map of the module. The ground albedo value (default = 0.2) can be varied in the model which has significant effect on the energy yield of bifacial module. Module model creates a sensitivity map of the module at STC condition as shown in figure 4.3. Since they utilize light from front and rear side, the calculation is performed for both sides separately [25], [58].

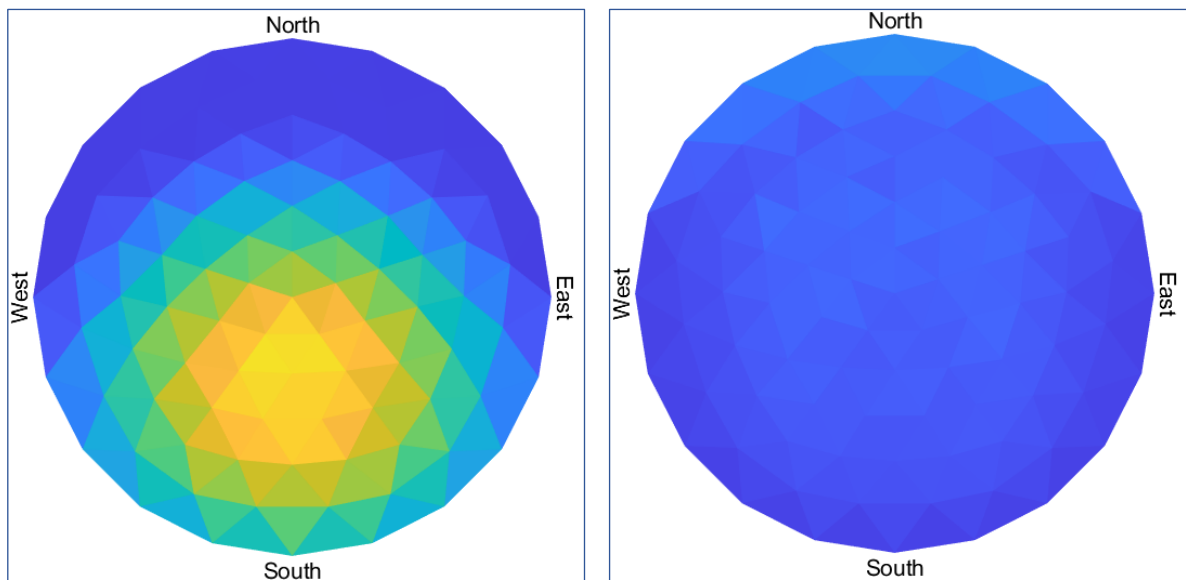


Figure 4.3: Sensitivity maps of the module for front (left) and rear (right) irradiance (Albedo = 0.4)

Weather model: The weather model employs Perez or newly implemented Preetham model to calculate the absorbed irradiance and corresponding photogenerated current of all 72 cells and absorber layers of the module. To study the effect of location on performance of photovoltaic

modules, energy yield is evaluated at three distinct sites: Reykjavik (Iceland, 64°08' N, Optimum tilt: 43°), Rome (Italy, 41°53' N, Optimum tilt: 30°) and Alice Springs (Australia, 23°42' S, Optimum tilt: 20°) [115]. The sky map developed using weather model for Rome is discussed in Chapter 2 and the effect of irradiance model in calculating the energy yield will be discussed in next section.

Thermal model: Depending on the hourly weather data for Rome and absorbed irradiance, temperature of individual cells in the module are calculated using the fluid-dynamic model explained by Smets et.al [31]. Energy balance equations are used to take into account, the effect of convective and radiative heat transfer between front glass, solar cell and rear glass while calculating individual cell temperature for a particular hour. The module temperature is assumed to be average of the maximum and minimum calculated cell temperatures for the hour (Figure 4.4).

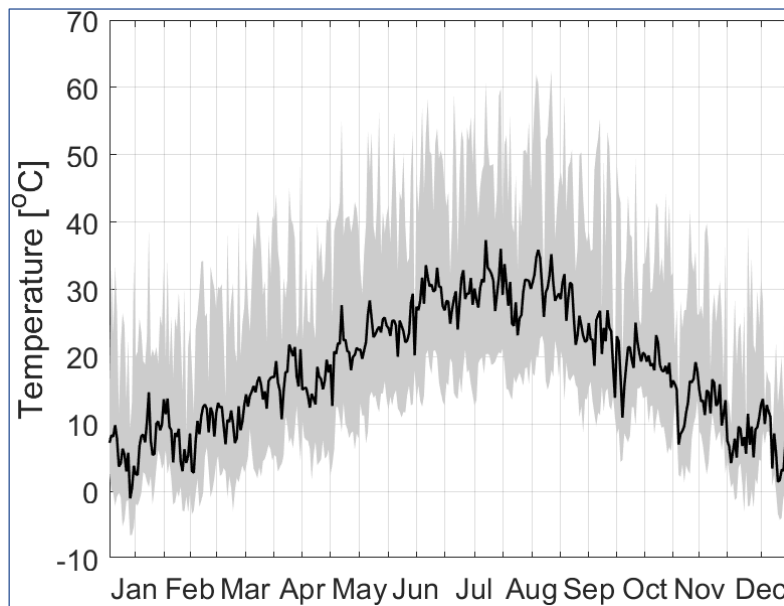


Figure 4.4: Calculated module temperature for every hour of the year at Rome from PVMD toolbox. The grey limits represent highest and lowest hourly cell temperatures.

Electric model: The parameter extraction model developed in Chapter 3 simulates the behaviour of cell parameters towards varying operating conditions. Calibrated lumped element model (CLEM) utilize the parameter fit functions to simulate the module-level electrical behavior and calculate their DC energy yield (Figure 4.5). The possible electrical configuration of cells available in the toolbox, i.e 2T, 3T or 4T, is chosen by the user to calculate I-V curve of the module. The number of bypass diodes are set to zero, and default metallization configuration set in toolbox (see Appendix D) is used to calculate the metallization and shading losses. Currently, the electrical effect of front and rear irradiation in bifacial modules is assumed to be similar to mono-facial modules in PVMD toolbox and for this study.

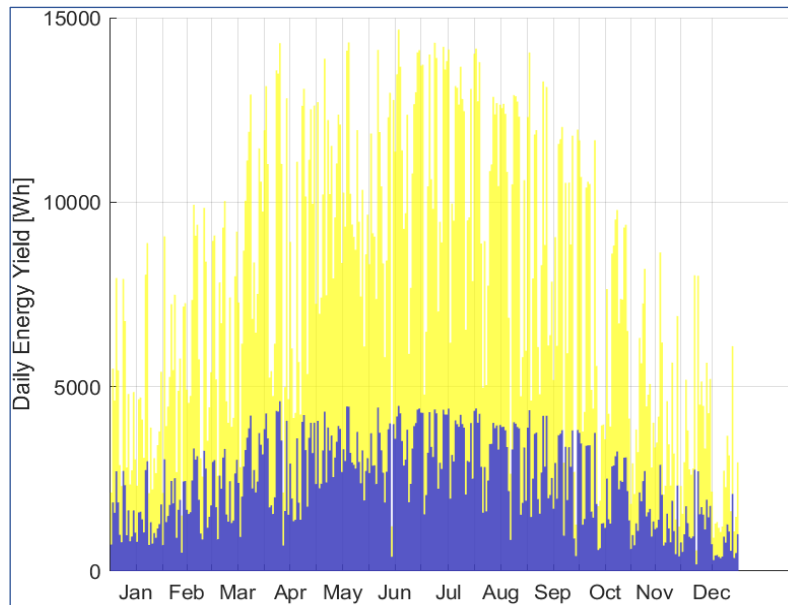


Figure 4.5: Hourly DC energy yield (blue) and incident irradiance for every hour of the year in Rome.

4.3. Real world conditions

As mentioned before, performance of photovoltaic modules in real world conditions differ from STC. To analyze and optimize their performance, in this section, effect of real world conditions on the modules are studied.

4.3.1. Effect of perovskite thickness

The top and bottom cells of mono-facial 2T tandem cell is current-matched at AM 1.5 spectrum, as mentioned before ($20.2\text{mA}/\text{cm}^2$ at 310 nm perovskite thickness). Although, depending on the location and time, the position of sun and corresponding AM spectrum changes. This could lead to a current mismatch at most times of the year, thus limiting the energy yield of the module. The analysis performed by Singh et.al studied the dependance of annual average photogenerated current of the 2T tandem module with changing perovskite thickness and location [25]. In this study, similar method is followed to optimize the perovskite thickness that maximizes specific energy yield of the module as shown in Figure 4.6. In the toolbox, the specific energy yield of a module is calculated by setting the operating conditions to STC while the module is set horizontal to the ground and sun at the zenith. Under these settings, the 2T tandem module is calculated to produce 530 Wp. For Rome, the optimum perovskite thickness is $\sim 310\text{nm}$, similar to the cell's current-matching perovskite thickness at STC. This is explained by the spectrum of incident light received by Rome, averaged across the year, being similar to AM 1.5 spectrum. Reykjavik receives incident light of higher AM spectrum. This is noticeable from the hourly zenith angle of sun for the location. The intensity of visible light, predominantly absorbed by perovskite top cell, is lesser when compared to infrared region. Therefore, thicker perovskite layer is required at Reykjavik to match the current produced by c-Si absorber layer ($\sim 320\text{nm}$). The specific yield of the module at optimum thickness is 39% lesser than at Rome. Conversely, Alice Springs receive lower AM spectrum light when averaged across the year. Ample visible light is received by the location to have a lower perovskite thickness ($\sim 290\text{nm}$) as the optimum to produce maximum specific energy yield of 2281.5 kWh/kWp, 48% higher than at Rome. For further

yield calculations of mono-facial 2T tandem modules in this study, the optimized perovskite thickness for the location will be used.

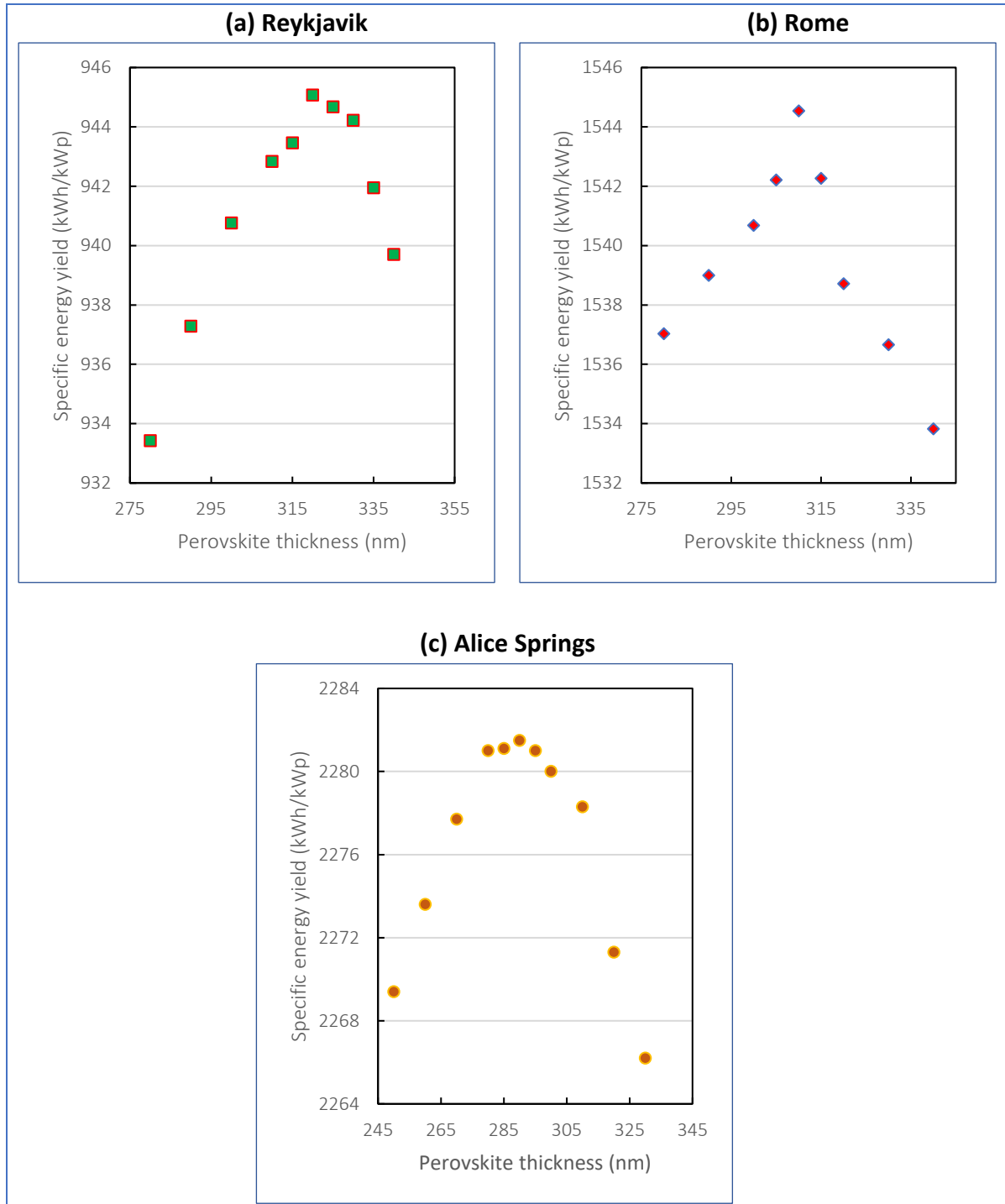


Figure 4.6: The effect of perovskite thickness on specific energy yield of 2T mono-facial tandem module at three different locations with distinct incident spectrum of light

In the case of bi-facial tandem modules, the rear side irradiance contributes to additional current from the bottom cell. Therefore, for a certain albedo value, the top cell absorber layer thickness has to be increased to match the extra current produced by c-Si absorber. Figure 4.7 illustrates the dependence of perovskite thickness on implied photo-current generated by top and bottom cells of bi-facial 2T tandem module at STC. Until a certain perovskite thickness (600 nm in this case), for a fixed albedo

value, the top cell is current-limiting. Beyond this point, bottom cell becomes current-limiting in 2T configuration, thereby causing a reduction in yield of the module. For higher albedo, the c-Si absorber layer produces current that requires very thick perovskite layer to achieve current-matching. This explains the dependency of AEY of bi-facial 2T tandem modules on albedo which will be discussed in section 4.3.4.

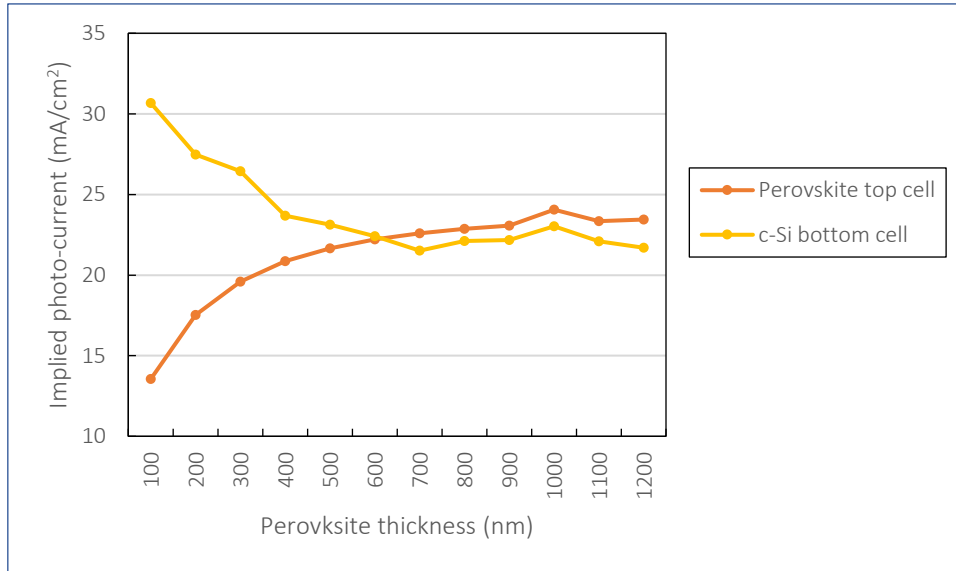


Figure 4.7: Implied photo-current of bi-facial 2T tandem module as a function of perovskite thickness (Albedo: 0.2)

4.3.2. Effect of daylight models

As discussed in Chapter 2, irradiance/daylight models calculate the luminance distribution across the skydome for a particular sun position. In this section, the annual energy yield (AEY) of 2T/4T mono-facial tandem modules and SHJ module are compared for Reykjavik, Rome and Alice Springs using Preetham and Perez daylight models. For the three locations, the yield difference for all modules in consideration differed by <1% between Preetham and Perez models. The sum of luminance from Preetham model exceeds Perez model over the year for all three locations (Rome: 2.35%, Reykjavik: 2.52%, Alice Springs: 1.2%). Although, this calculated difference in luminance is not reflected in the AEY when skymap and sensitivity maps of the module are combined as shown in Figure 4.8. This could be attributed to Preetham model using Equation 2.15 to calculate the air mass to determine the hourly spectral brightness while Perez model calculates air mass using the expression, $AM = 1/(\cos \theta)$. Air mass for the hour is significant in calculating interpolated spectral radiant power. The spectral radiant power further determines the absorbed power in every cell and absorbed photon flux in every cell layer. Due to this reason, the yields calculated using the two daylight models are almost equal in Rome, while Preetham model exceeds Perez model in Reykjavik and vice-versa at Alice Springs.

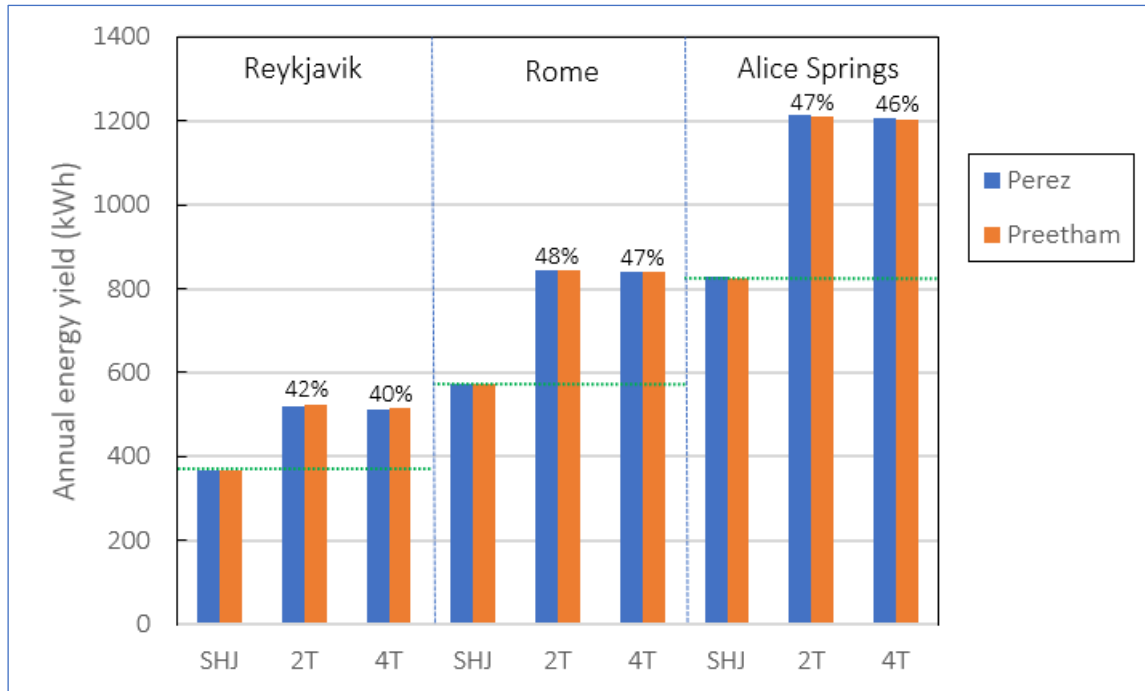


Figure 4.8: The annual energy yield of SHJ and mono-facial 2T/4T tandem modules at Reykjavik, Rome and Alice Springs. The percentages indicate the increase in energy yield of 2T and 4T modules when compared to SHJ module for every location.

4.3.3. Effect of location

Figure 4.8 indicates the increase in AEY for mono-facial 2T/4T tandem modules when compared to SHJ module at the same location. It is to be noted that the thickness of perovskite layer in 4T device is set to the current-matched perovskite thickness of their 2T counterpart for the location for a fair comparison between the two configurations. Numerous factors like insolation, cloud coverage, temperature and wind speed at a location affect the energy yield of a module. Therefore, the production can vary significantly when the same module is placed at different locations. At all three locations, 4T module displayed slightly lesser yield compared to their 2T counterpart. This is explained by the optical losses in 4T cell structure due to transparent electrodes for collecting the charge carriers and the EVA layer to separate the top and bottom cells. At Rome, the 2T module produces 843 kWh, giving 48% higher yield than the SHJ module at same location. 2T tandem modules at Reykjavik and Alice Springs produce 518 kWh and 1213 kWh, thereby producing 42% and 47% higher energy yield compared to SHJ modules. Due to thicker perovskite layer, the c-Si layer is current-limiting for optimized 2T tandem module in Reykjavik most time of the year. Although, since 4T device is mechanically stacked, the production from top and bottom cells are utilized completely. Besides the optimum perovskite thickness for the location, the energy produced by the tandem modules is highest at Alice Springs due to the highest insolation received by the location. Since 4T devices are electrically de-coupled, the thickness of perovskite layer in 4T tandem can be set at a higher value allowing the module to have a higher yield than the 2T device for a certain location. Since 4T devices are optically coupled, increasing the perovskite thickness would result in lower photo-generated current from the bottom cell. Besides the thicker perovskite layer, due to the absorber's higher bandgap compared to c-Si, more energy is generated from absorbed photons, resulting in higher energy yield. The effect of perovskite thickness on AEY of mono-facial and bi-facial tandem modules are studied in next section.

4.3.4. Mono-facial and bi-facial modules

All modules considered until now only utilizes the front side illumination. Depending on the ground albedo, bi-facial modules utilize rear side illumination for a higher energy yield when compared to mono-facial modules [49], [116]–[118]. The effect of albedo for varied perovskite thickness on mono-facial and bi-facial 2T/4T devices at Rome will be studied in this section. Since a standard model is not defined to involve bi-faciality factor while calculating the energy yield of bi-facial module at STC, annual energy yield is used to compare performance of the modules. Figure 4.8 illustrates the AEY of bi-facial 2T tandem modules at three albedo values: 0.09 (sandstone), 0.44 (green grass) and 0.85 (snow).

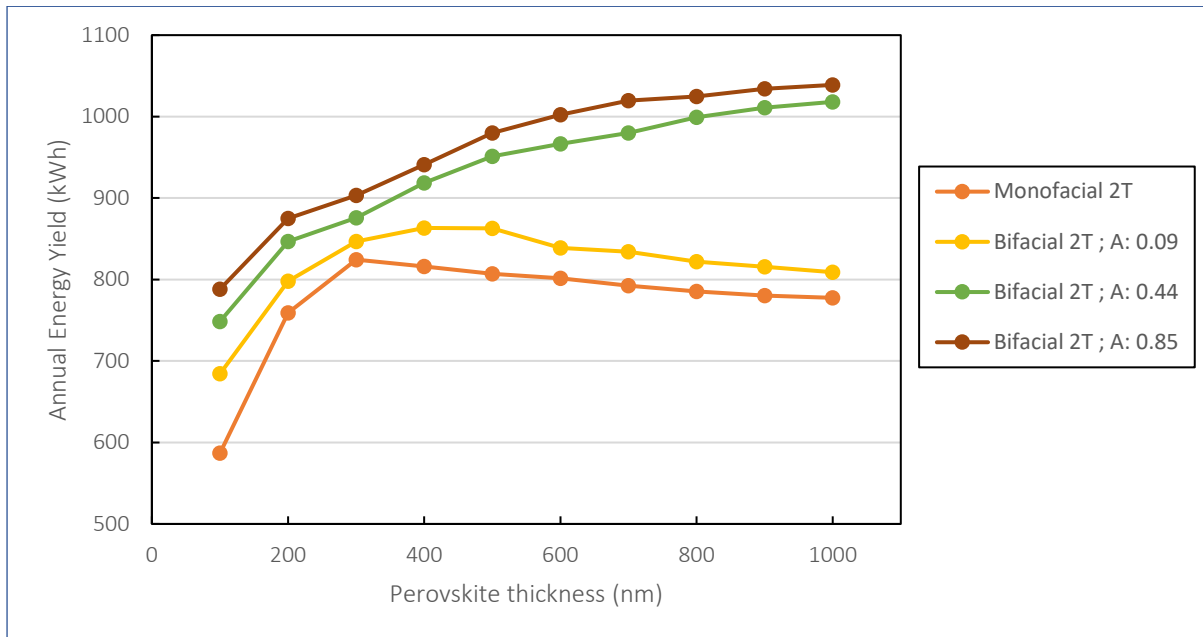


Figure 4.9: Effect of albedo on AEY of bi-facial 2T tandem module at Rome as a function of perovskite thickness. (A: Albedo)

As discussed in previous section, mono-facial 2T tandem modules produce maximum energy yield at the current-matched perovskite thickness for the location. But for bi-facial modules, apart from front side irradiance, incident light from rear side is also utilized by c-Si bottom cell. Although, since top cell do not benefit from rear side luminance, a thicker perovskite layer is required to compensate for the higher current produced in bottom cell. As the thickness of perovskite is increased even further, bottom cell becomes the current-limiting layer, causing a decline in AEY. For higher albedo values of 0.44 and 0.85, even at high perovskite thickness of 1000nm, the AEY seems to increase. This is due to the current-limiting top cell that do not compensate for the extra current produced by bottom cell using rear side irradiance.

At high perovskite thickness, the bottom cell is current-limiting, causing a reduction in AEY. Although, due to constraints in fabricating perovskite of thicknesses beyond 1000nm, we do not consider their effect in this study [25]. Study conducted by Fabrizio et.al noticed a similar trend in dependency of perovskite thickness on AEY of mono-facial 2T tandem modules [22]. This dependency of perovskite thickness on AEY of the module is due to the monolithic integrated top and bottom cells in 2T configuration.

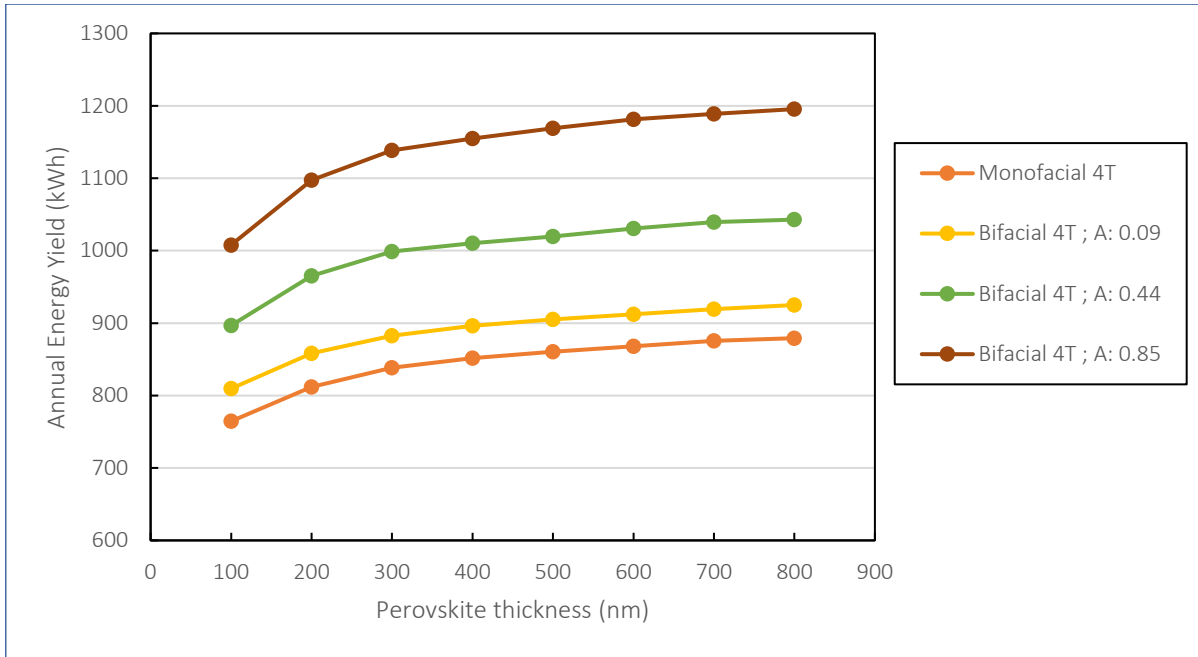


Figure 4.10: Effect of albedo on AEY of bi-facial 4T tandem module at Rome as a function of perovskite thickness. (A: Albedo)

As discussed in Chapter 1, mechanically-stacked 4T devices do not require current-matching between top and bottom cells. Although, this advantage of 4T tandem modules come at a cost of higher optical losses due to transparent contacts between top and bottom cells [25]. For increasing perovskite thickness, the optical losses are compensated by higher production in the top cell for low albedo values. The bifacial tandem module considered in this study consists of textured top cell as mentioned in section 4.1, which explains the difference in energy yield between mono-facial 4T tandem and bi-facial 4T tandem module exposed to ground with low albedo value of 0.09. As the albedo increases, extra current is generated in the bottom cell due to the utilization of rear side irradiance. But as the perovskite thickness increases beyond a certain point (beyond 800 nm) for a given albedo, the rate of increase in AEY goes down. This is explained by absorption depth of semiconductor material and decay of incident light intensity. Absorption depth gives the distance incident light has to travel through the absorber before being absorbed completely, and is expressed as the inverse of wavelength-dependent absorption coefficient [119]. Absorption coefficient is a characteristic of the material used in the device. As the intensity of incident photons drop exponentially with distance (Lambert-Beer's Law), there is no significant increase in generated current from perovskite cell as their thickness exceeds 800 nm [31]. Therefore, increasing perovskite thickness beyond this point do not have significant impact on energy yield of the module.

Figure 4.11 illustrates the effect of albedo on energy yield contribution of top and bottom cells for bi-facial 4T tandem module with perovskite thickness fixed at 700 nm. With increasing albedo, the energy produced from bottom cell increases significantly when compared to perovskite top cell. While the rear side irradiance is completely utilized by the c-Si bottom cell, a slight increase in contribution to energy yield is noticed from perovskite top cell.

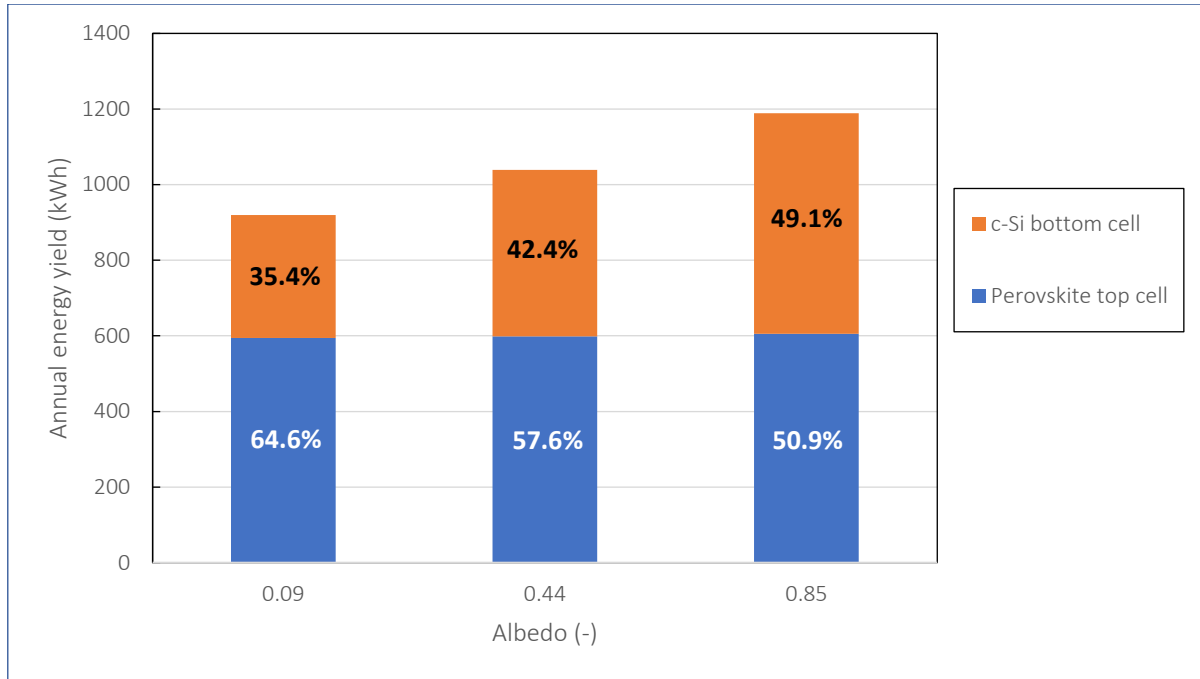


Figure 4.11: Contribution of perovskite top cell and c-Si bottom cell to AEY of bi-facial 4T tandem module for different albedo surfaces. The perovskite thickness is fixed at 700nm.

4.4. Conclusion

In this chapter, the energy yield of mono-facial and bi-facial 2T/4T tandem modules are calculated and analyzed using the newly implemented Preetham model and parameter extraction model at Reykjavik, Rome and Alice Springs. Therefore, this chapter realizes the final objective of this thesis.

The tandem structures used in this study are introduced before describing the step-by-step process of calculating the annual energy yield of bifacial 2T tandem module in PVMD toolbox. To maximize specific energy yield, perovskite thickness of mono-facial 2T tandem modules are optimized for every location. While the module produced maximum yield for 310 nm in Rome, Reykjavik produced 39% lesser yield at 320 nm and Alice Springs displayed 47% higher yield for 290 nm, owing to air mass of the locations. Although there is significant difference in calculated luminance between the two daylight models, the energy yield difference is <1% for all modules and locations. Due to the highest insolation received at the location, modules at Alice Springs produce highest yield among all locations. The effect of perovskite thickness on energy yield of 2T/4T mono-facial and bi-facial modules are studied as well. For increasing perovskite thickness and high albedo, energy yield of 2T bi-facial modules increase significantly due to extra current generated by bottom cell. At the same time, energy yield drops beyond optimum thickness due to current mismatch for low albedo surfaces. Bi-facial 4T modules produce highest yield among all modules for high albedo (0.85) surface, thereby producing 36% higher yield than mono-facial 4T tandem module in Rome.

5

Conclusions and Recommendations

This chapter summarizes and concludes the results obtained while answering the objectives defined in Chapter 1 and provides recommendations for future study. The main research goal of this thesis was to perform

Energy yield simulations of perovskite/c-Si tandem modules in real-world conditions

To achieve this goal, three main objectives were defined as mentioned in section 1.7 and answered through this study. Following sections summarize the answers to these research objectives.

5.1. Implement spectrally resolved daylight model

To accurately determine the irradiance falling on a module, and the corresponding absorbed irradiance and energy yield, Preetham daylight model is implemented as an improvement to Perez model currently used in the PVMD toolbox. Preetham model is proven to be more efficient in terms of computational speed, and accurate since the model considers the effect of turbidity into account when compared to Perez model [70], [78]. Three components are calculated using the model: luminance, RGB vector co-ordinates and spectrally resolved relative power distribution across the visible spectrum for all points on the skydome.

Luminance is predominantly calculated using the relation introduced by Perez et.al that utilizes coefficients determined through a spectral radiance function for varied sun positions and turbidities created by Preetham et.al [60], [63]. The relative luminance thus calculated is normalized against hourly DHI. Finally, DNI is added to the sky element closest to the sun to determine the overall hourly luminance distribution. Although spectral model introduced by Bird et.al is implemented in this study to calculate the hourly irradiance received by the module from attenuated extra-terrestrial irradiance, the calculated DNI varies largely from measured data [82]. Therefore, the irradiance data used in Preetham model is taken from Meteonorm for this study. The RGB vector co-ordinates are calculated using relative luminance normalized against zenith luminance for every hour to evaluate CIE xyY values for every point on the skydome. Colored image of the sky is rendered by plotting standard RGB co-ordinates converted from CIE xyY values for every point of the sky and for every hour. Calculating the relative spectral radiant power distribution allows the analysis of incident visible light falling on the module from all points of the skydome. The method introduced by Wyszecki and Stiles was incorporated into the Preetham model that assumes sun as a D65 illuminant and calculates relative SRP as a function of the chromaticity values determined for every point of the sky [79].

For Reykjavik, Rome and Alice Springs, sum of yearly luminance calculated using Preetham model exceeded Perez model by 2.52%, 2.35% and 1.2% respectively. The luminance at every point is normalized against DHI such that the sum of luminance across the skydome from the module's

perspective adds up to the DHI received at the location for that hour. Rendering the colored sky image gives a distinct hourly visual representation of the sun and sky, and effect of light scattering due to atmospheric particles. Images rendered using Preetham model at all months of the year in Rome and at different turbidities are illustrated in Figures 2.6 and 2.7. Finally, the relative intensity of light in the visible spectrum received by a tandem module can now be analyzed using the relative spectral radiant power distribution. The change in visible light spectrum received from a certain point in sky at different times of the day is shown in Figure 2.10. While the sun is closest to the triangle at noon, the relative intensity of light from the sky element is higher than the standard D65 illuminant. At sunset, least amount of incident light is received from that point in sky since the sun is farthest from the chosen sky element.

5.2. Implement parameter extraction model for simulated J-V curves

Energy yield of a module is calculated by simulating the electrical behaviour of solar cells at various operating conditions. For this purpose, an analytical model is developed to extract solar cell parameters from ASA J-V curves using five-parameter single diode model for PVMD toolbox. The method offers good computational speed in calculating the parameters while not compromising on accuracy. Although, parameters like series and shunt resistances are calculated under certain assumptions. This leads to inaccuracies that are visible while fitting the ASA J-V curve to re-constructed J-V curve using extracted parameters. Through trial-and-error, a change in series resistance is noted to have significant impact in fitting the simulated and re-constructed curves. Therefore, the analytic model is extended to recalculate and correct the series resistance to minimize the deviation between ASA and re-constructed J-V curves.

In this study, parameters of perovskite and SHJ cells are extracted to simulate the electrical behaviour of top and bottom cells that form the tandem cell structure. J-V curves at 12 different temperatures between 250 K and 360 K, and 15 irradiance intensities between 100 W/m² and 1500 W/m² are simulated in ASA to calculate the behavioural trend of parameters for numerous operating conditions. This trend of extracted parameters is expressed through coefficients of a polynomial fit curve that is used in the cell level electrical model to couple the effect of irradiance and temperatures to simulate real-world operating conditions.

The parameter extraction model developed in this study is validated by determining the deviation between ASA J-V curves and reconstructed J-V curve using extracted parameters from the model. The deviations thus noted for perovskite and c-Si solar cells at different irradiances and temperatures are shown in Figure 3.3. At STC, the RMSE for perovskite and SHJ cells are calculated at 3.02% and 1.98% respectively. For simulating the energy yield of tandem modules consisting of any top and bottom cells, the parameter extraction model developed in this study can be utilized to simulate the electrical behaviour of the cells at various operating conditions. Although fairly accurate, the model can be improved by correcting parameters that are calculated under fair assumptions other than series resistance (e.g shunt resistance) to minimize the fitting error between simulated and re-constructed J-V curves.

5.3. Evaluate and analyze the energy yield of photovoltaic modules

The main objective of implementing Preetham daylight model and parameter extraction model in PVMD toolbox is to simulate the energy yield of photovoltaic modules in real-world conditions. Therefore, using these models, performance of mono-facial and bi-facial perovskite/c-Si tandem modules in 2T and 4T configurations are analysed.

Using the perovskite and c-Si sub-cells introduced in Chapter 3, tandem cell structures are introduced. Later, the step-by-step process of simulating the AEY of bi-facial 2T tandem module is explained to show the working of PVMD toolbox. While the performance of modules are usually expressed at STC, real-world conditions may largely differ from this throughout the year depending on the location. Therefore, the energy yield of tandem modules are calculated at three locations (Reykjavik, Rome and Alice Springs) to study the effect of location and perovskite thickness on the modules. To maximize the yield of the module, optimum module tilt is chosen for the location.

For a particular location, the perovskite thickness is optimized for 2T mono-facial tandem module to minimize current-mismatch losses and to maximize specific yield. Rome produces highest specific yield for optimum thickness of 310 nm, whereas Reykjavik and Alice Springs produce maximum specific yield at 320 nm and 290 nm respectively. While Rome receives incident light similar to AM 1.5 spectrum when averaged over the year, Reykjavik with higher air mass requires thicker perovskite layer to absorb lower intensity of light in visible region and vice-versa for Alice Springs. The optimized perovskite thickness is used in 2T and 4T mono-facial modules to compare the effect of the new Preetham daylight model and Perez models on their AEY. As summarized in section 5.1, although Preetham model calculates higher annual luminance compared to Perez model, the AEY difference for both modules is <1% for all locations. This is attributed to the air mass that accounts for scattering by air molecules used in Preetham model. While comparing the locations, 2T tandem module has highest AEY at Alice Springs (43% higher than Rome) owing to the highest insolation received at the location, while Reykjavik produces the least (38% lower than Rome). Similar trends are noticed for SHJ and 4T tandem modules as well. To consider the effect of rear side irradiance, AEY of bi-facial 2T/4T modules are compared against their mono-facial counterparts at different albedo surfaces. For bi-facial 2T devices, at low albedo values ($A=0.09$) and beyond perovskite thickness of 400 nm in this case, bottom cell becomes current-limiting causing a decrease in AEY. At the same time, for high albedo, current generated by a thick perovskite layer is current-limiting due to the extra current produced by c-Si cell. Since 4T devices are mechanically stacked, using a perovskite layer thicker than 2T device's optimum allows higher current generation from top cell and consecutively, higher yield from the module.

5.4. Recommendations

The models introduced in this thesis and the analysis conducted provide scope for improvement in future studies. They are as follows:

- Preetham daylight model: The luminance calculated using the model is in photometric units (cd/m^2). Since PVMD toolbox uses radiometric units ($\text{W}/\text{m}^2\text{-sr}$), the luminance values can be converted using the photopic spectral luminous efficiency curve rather than normalizing it against DHI values. By implementing this, a larger difference in calculated luminance may be noticed between Preetham and Perez models.
- Preetham daylight model: Currently, the model keeps the turbidity constant (at 3) indicating clear sky throughout the year. If varying turbidity is considered, the image rendered and yield calculated can be more realistic.
- Preetham daylight model: Preetham model utilizes reference data simulated by Nishita et.al between turbidities of 2 and 6 to create a sky spectral radiance function. Therefore, to include more atmospheric conditions, Hosek-Wilkie model can be implemented in PVMD toolbox.
- Relative spectral power distribution: The Preetham model calculates relative spectral power distribution over the visible light spectrum for every point on the skydome. For a better understanding of the incident light, absolute spectral power distribution could be calculated, and for a larger wavelength range outside the visible spectrum.

- Parameter extraction model: The accuracy of model can be improved by correcting series and shunt resistance extracted from ASA-simulated J-V curves. The model can be incorporated into the PVMD toolbox to facilitate direct parameter extraction depending on the top and bottom cells input from the user.
- Parameter extraction model: Usability of the model must be tested for other cell structures as well.
- Cell level electric model: For every cell simulated in the toolbox, the coupling of temperature and irradiance conditions require modification to avoid infinite/illogical values for calculated current. Therefore, operating conditions coupling require further development to avoid manual modifications while simulating energy yield of any module.
- Electric model: In this study, energy yield of bi-facial tandem modules are simulated without considering the electrical effects of temperature and irradiance. Therefore, model to simulate bi-facial tandem modules at electric level could be developed in future study. Spectral effects of albedo on bi-facial modules is not considered in this work. This could be interesting for future study.
- Analysis of energy yield: In this study, the energy yield of 2T and 4T devices are analysed. Recently, 3T configuration of tandem devices have shown promising results that combine the advantages of 2T/4T configurations [22], [25]. In future study, the performance of 3T device would be interesting to analyse and compare with 2T and 4T devices.

Appendix | A

The expressions in this section are referred from the model created by Bird and Riordan in 1984 [82], [120].

Direct irradiance

The transmittance functions for the atmospheric particles are as follows:

Rayleigh scattering, $\tau_{r,\lambda} = e^{-0.008735\lambda^{-4.08}m}$

Aerosol attenuation, $\tau_{a,\lambda} = e^{-\beta\lambda^{-\alpha m}}$

Ozone absorption, $\tau_{o,\lambda} = e^{-k_{o,\lambda}lm}$

Mixed gases absorption, $\tau_{g,\lambda} = e^{-1.41k_{g,\lambda}m/(1+118.93k_{g,\lambda}m)^{0.45}}$

Water vapour absorption, $\tau_{wa,\lambda} = e^{-0.2385k_{wa,\lambda}wm/(1+20.07k_{wa,\lambda}wm)^{0.45}}$

where

$k_{o,\lambda}$, $k_{g,\lambda}$ and $k_{wa,\lambda}$ are the attenuation coefficients for ozone, mixed gases and water vapour respectively.

Angstrom's turbidity coefficient, $\beta = 0.04608T - 0.04586$

Amount of ozone in atmosphere, $l = 0.34 \text{ atm} - \text{cm}$ at STC

Precipitable water vapour, $w = 0.34 \text{ cm}$ at STC

As per the rural aerosol model,

$$\alpha = \begin{cases} 1.0274 & \text{for } \lambda < 0.5 \mu\text{m} \\ 1.2060 & \text{for } \lambda > 0.5 \mu\text{m} \end{cases}$$

Diffuse irradiance

The components taken into consideration to calculate diffuse irradiance is as follows:

Rayleigh scattering component, $I_{r\lambda} = Irr_{ext} \cos\theta_s \tau_{o,\lambda} \tau_{u,\lambda} \tau_{wa,\lambda} \tau_{aa,\lambda} (1 - \tau_{r,\lambda}^{0.95}) 0.5 * C_s$

Aerosol scattering component, $I_{a\lambda} = Irr_{ext} \cos\theta_s \tau_{o,\lambda} \tau_{u,\lambda} \tau_{wa,\lambda} \tau_{aa,\lambda} \tau_{r,\lambda}^{1.5} (1 - \tau_{as,\lambda}) * F_s C_s$

where,

$$C_s(\lambda) = \begin{cases} (\lambda + 0.55)^{1.8} & \text{for } \lambda \leq 0.45 \\ 1 & \text{for } \lambda > 0.45 \end{cases}$$

Aerosol albedo, $\omega_\lambda = 0.945 * \exp(-0.095 * [\ln(\frac{\lambda}{0.4})]^2)$

Angstrom formula for turbidity, $\tau_{a,\lambda} = \beta * (\lambda/0.5)^{-\alpha}$

$$\tau_{as,\lambda} = \exp(-\omega_\lambda - \tau_{a,\lambda} * m)$$

$$\tau_{aa,\lambda} = \exp(-(1 - \omega_\lambda) * \tau_{a,\lambda} * m)$$

For rural aerosol model,

$$\langle \cos\theta \rangle = 0.65$$

$$ALG = \ln(1 - \langle \cos\theta \rangle)$$

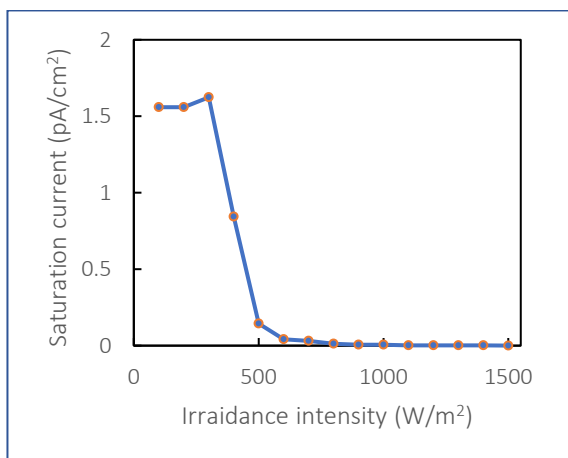
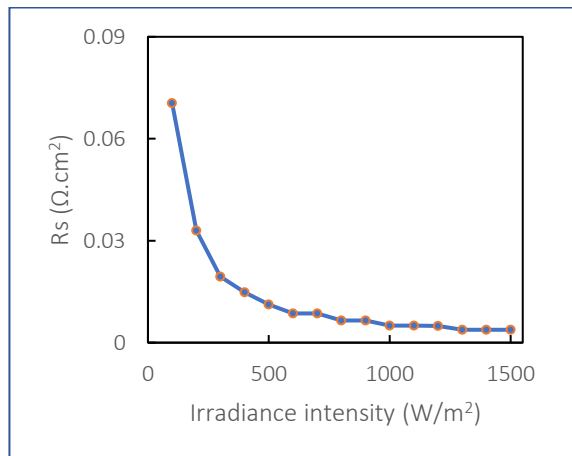
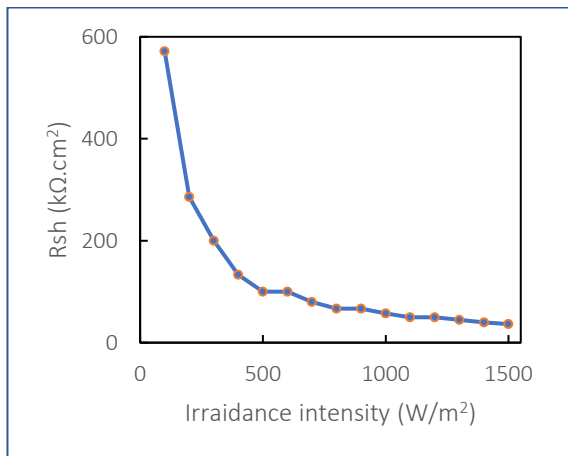
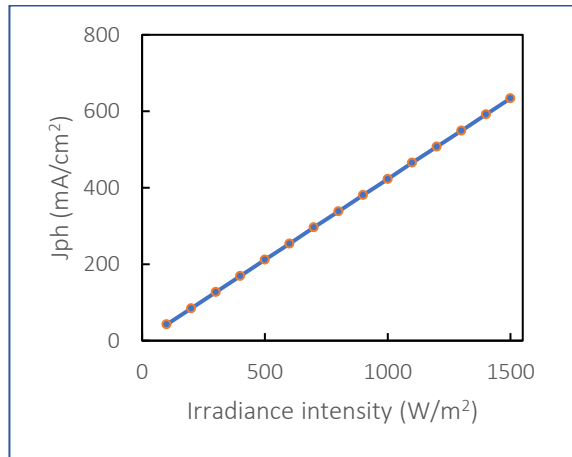
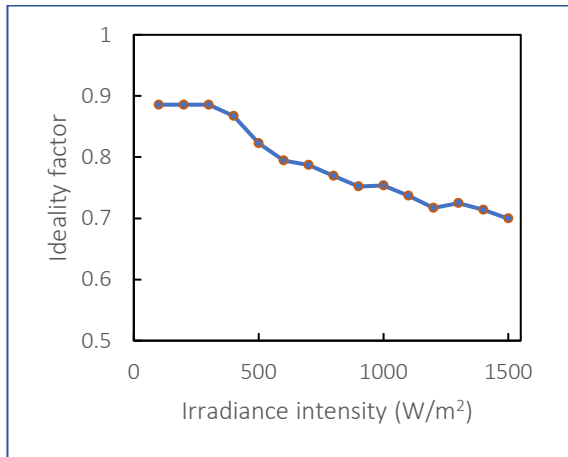
$$AFS(\lambda) = ALG * (1.459 + (ALG(0.1595 + ALG * 0.4129)))$$

$$BFS(\lambda) = ALG * (0.0783 + ALG(-0.3824 - ALG * 0.5874))$$

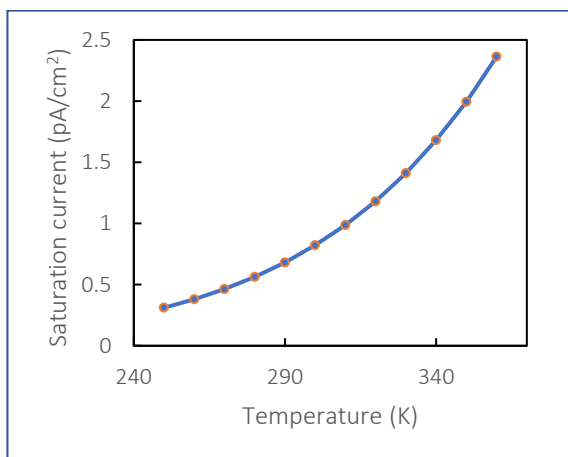
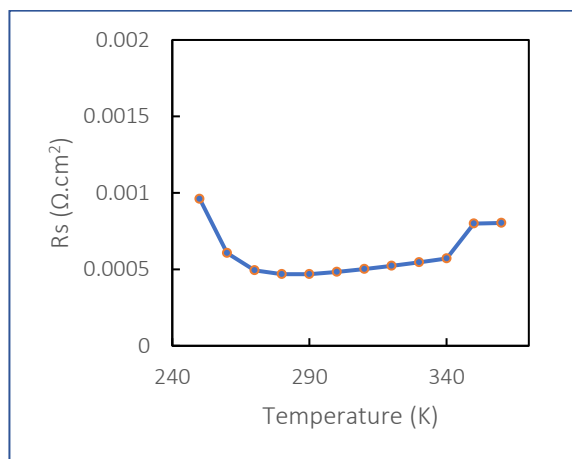
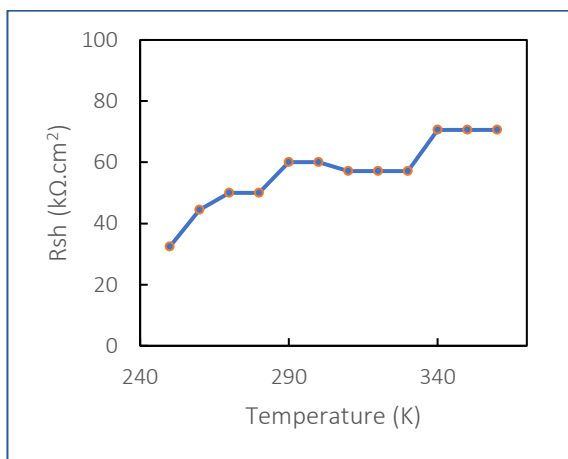
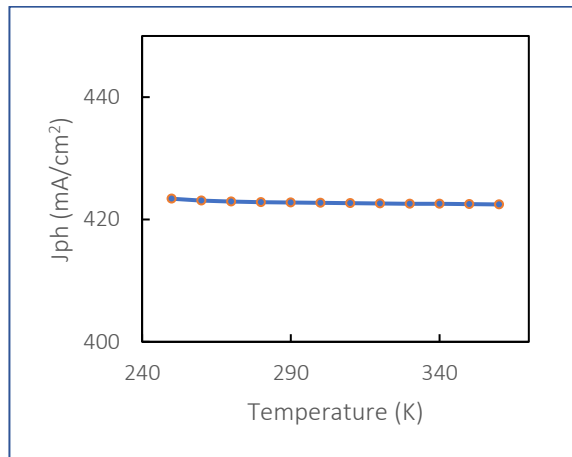
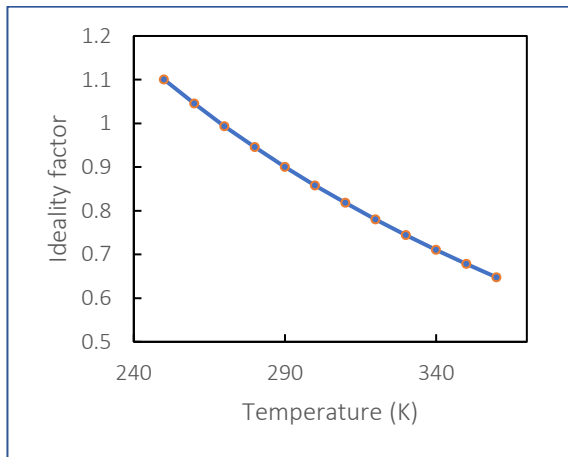
$$F_s(\lambda) = 1 - 0.5 * \exp((AFS(\lambda) + BFS(\lambda) * \cos(\theta_s)) * \cos(\theta_s))$$

Appendix | B

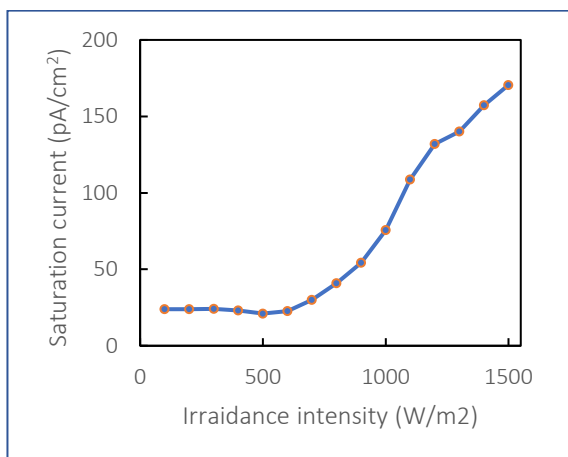
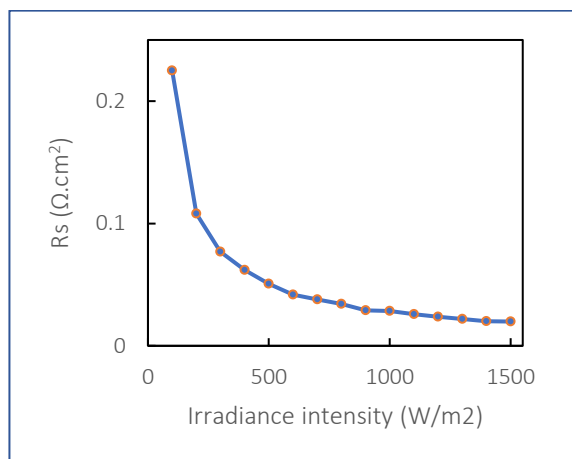
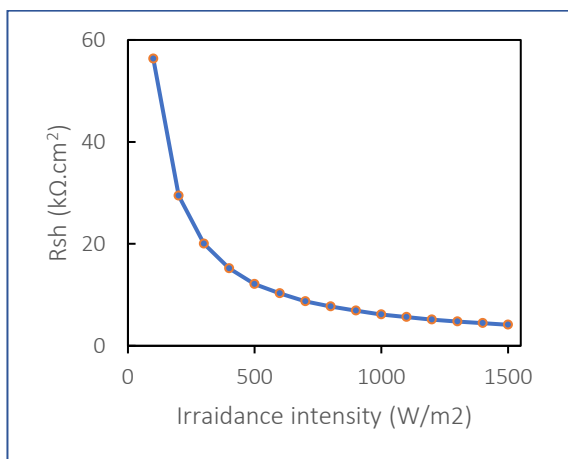
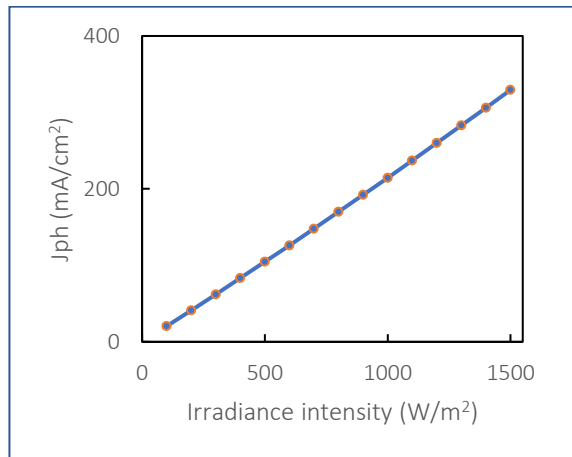
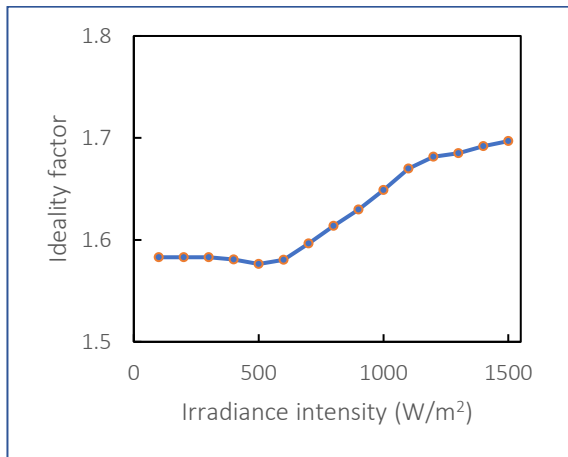
Effect of irradiance on SHJ cell



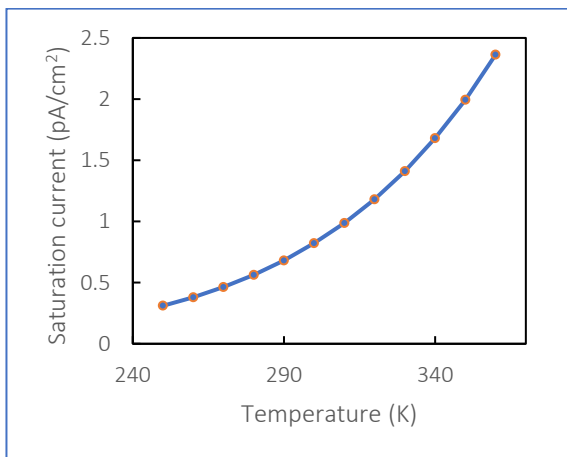
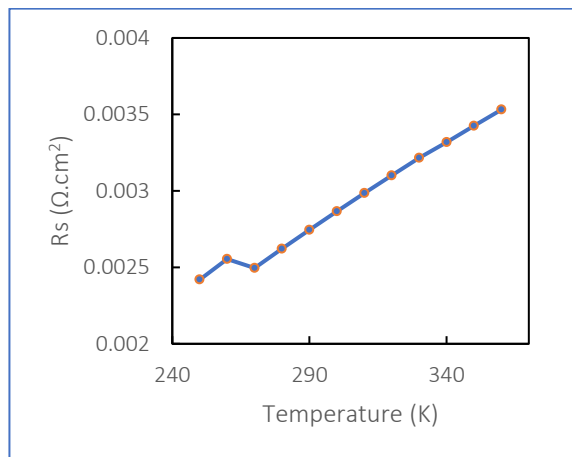
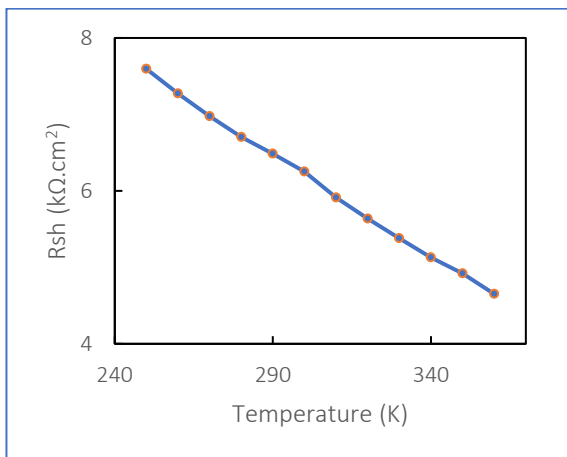
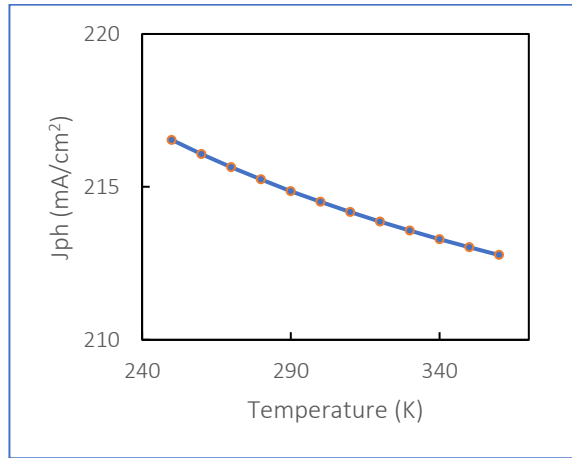
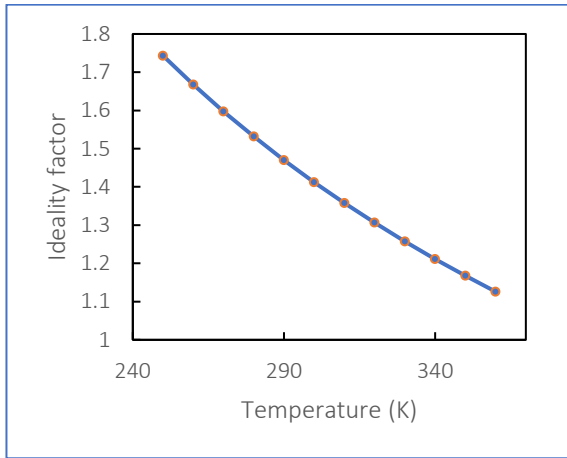
Effect of temperature on SHJ cell



Effect of irradiance on perovskite cell



Effect of temperature on perovskite cell



Appendix | C

Module Geometry

Number of cell rows	12
Number of cell columns	6
Module thickness (cm)	0.5
Cell spacing (cm)	0.3
Edge spacing (cm)	1
Module tilt (deg)	<i>Optimum tilt for the location. Default = 27</i>
Module azimuth (deg)	(South= 0; West= 90; North= 180; East= 270)
Height to ground (cm)	50
Module side spacing (cm)	100
Module row spacing (cm)	800
Cell length (cm)	15.675
Cell width (cm)	15.675
Albedo [0-1]	<i>Variable. Default = 0.2</i>

Metallization

Number of busbars (#/cell)	3
Fingers spacing (#/cm)	10
Busbar thickness (m)	100e-6
Finger thickness (m)	50e-6

Bibliography

- [1] EIA, 'EIA projects nearly 50% increase in world energy use by 2050, led by growth in Asia', Sep. 24, 2019. <https://www.eia.gov/todayinenergy/detail.php?id=41433> (accessed Sep. 11, 2020).
- [2] IRENA, 'Renewable energy highlights'. International Renewable Energy Agency, Jul. 01, 2020. Accessed: Sep. 11, 2020. [Online]. Available: <https://www.irena.org/publications/2020/Jul/Renewable-energy-statistics-2020>
- [3] Oxford PV, 'Oxford PV hits new world record for solar cell', Dec. 21, 2020. <https://www.oxfordpv.com/news/oxford-pv-hits-new-world-record-solar-cell> (accessed Jun. 28, 2021).
- [4] IRENA, 'Renewable power generation costs in 2020'. IRENA. Accessed: Jun. 28, 2021. [Online]. Available: <https://www.irena.org/publications/2021/Jun/Renewable-Power-Costs-in-2020>
- [5] W. Shockley and H. J. Queisser, 'Detailed balance limit of efficiency of p-n junction solar cells', *Journal of applied physics*, vol. 32, no. 3, pp. 510–519, 1961.
- [6] A. Richter, J. Benick, F. Feldmann, A. Fell, M. Hermle, and S. W. Glunz, 'n-Type Si solar cells with passivating electron contact: Identifying sources for efficiency limitations by wafer thickness and resistivity variation', *Solar Energy Materials and Solar Cells*, vol. 173, pp. 96–105, 2017.
- [7] K. Yoshikawa *et al.*, 'Exceeding conversion efficiency of 26% by heterojunction interdigitated back contact solar cell with thin film Si technology', *Solar Energy Materials and Solar Cells*, vol. 173, pp. 37–42, Dec. 2017, doi: doi.org/10.1016/j.solmat.2017.06.024.
- [8] J. Haschke, O. Dupré, M. Boccard, and C. Ballif, 'Silicon heterojunction solar cells: Recent technological development and practical aspects - from lab to industry', *Solar Energy Materials and Solar Cells*, vol. 187, pp. 140–153, Dec. 2018, doi: [10.1016/j.solmat.2018.07.018](https://doi.org/10.1016/j.solmat.2018.07.018).
- [9] A. Louwen, W. van Sark, R. Schropp, and A. Faaij, 'A cost roadmap for silicon heterojunction solar cells', *Solar Energy Materials and Solar Cells*, vol. 147, pp. 295–314, Apr. 2016, doi: [10.1016/j.solmat.2015.12.026](https://doi.org/10.1016/j.solmat.2015.12.026).
- [10] K. Masuko *et al.*, 'Achievement of More Than 25% Conversion Efficiency With Crystalline Silicon Heterojunction Solar Cell', *IEEE Journal of Photovoltaics*, vol. 4, no. 6, pp. 1433–1435, Nov. 2014, doi: [10.1109/JPHOTOV.2014.2352151](https://doi.org/10.1109/JPHOTOV.2014.2352151).
- [11] M. A. Green, Y. Hishikawa, E. D. Dunlop, D. H. Levi, J. Hohl-Ebinger, and A. W. Y. Ho-Baillie, 'Solar cell efficiency tables (version 51)', *Progress in Photovoltaics: Research and Applications*, vol. 26, no. 1, pp. 3–12, Jan. 2018, doi: [10.1002/pip.2978](https://doi.org/10.1002/pip.2978).
- [12] J. Nakamura, N. Asano, T. Hieda, C. Okamoto, H. Katayama, and K. Nakamura, 'Development of Heterojunction Back Contact Si Solar Cells', *IEEE Journal of Photovoltaics*, vol. 4, no. 6, pp. 1491–1495, Nov. 2014, doi: [10.1109/JPHOTOV.2014.2358377](https://doi.org/10.1109/JPHOTOV.2014.2358377).
- [13] K. Ghosh, C. J. Tracy, S. Herasimenka, C. Honsberg, and S. Bowden, 'Explanation of the device operation principle of amorphous silicon/ crystalline silicon heterojunction solar cell and role of the inversion of crystalline silicon surface', in *2010 35th IEEE Photovoltaic Specialists Conference*, Jun. 2010, pp. 001383–001386. doi: [10.1109/PVSC.2010.5614387](https://doi.org/10.1109/PVSC.2010.5614387).
- [14] S. De Wolf *et al.*, 'Organometallic halide perovskites: sharp optical absorption edge and its relation to photovoltaic performance', *The journal of physical chemistry letters*, vol. 5, no. 6, pp. 1035–1039, 2014.
- [15] E. Unger, L. Kegelmann, K. Suchan, D. Sörell, L. Korte, and S. Albrecht, 'Roadmap and roadblocks for the band gap tunability of metal halide perovskites', *Journal of Materials Chemistry A*, vol. 5, no. 23, pp. 11401–11409, 2017.
- [16] S. D. Stranks *et al.*, 'Electron-hole diffusion lengths exceeding 1 micrometer in an organometal trihalide perovskite absorber', *Science*, vol. 342, no. 6156, pp. 341–344, 2013.

- [17] H. J. Snaith, 'Present status and future prospects of perovskite photovoltaics', *Nature materials*, vol. 17, no. 5, pp. 372–376, 2018.
- [18] C. Zuo, H. J. Bolink, H. Han, J. Huang, D. Cahen, and L. Ding, 'Advances in Perovskite Solar Cells', *Advanced Science*, vol. 3, no. 7, Jan. 2016, doi: <https://doi.org/10.1002/adv.201500324>.
- [19] Z. Fang, Q. Zeng, C. Zuo, and L. Zhang, 'Perovskite-based tandem solar cells', *Science Bulletin*, Nov. 2020, doi: <https://doi.org/10.1016/j.scib.2020.11.006>.
- [20] M. A. Green, A. Ho-Baillie, and H. J. Snaith, 'The emergence of perovskite solar cells', *Nature Photonics*, vol. 8, no. 7, pp. 506–514, Jul. 2014, doi: 10.1038/nphoton.2014.134.
- [21] F. Sahli *et al.*, 'Fully textured monolithic perovskite/silicon tandem solar cells with 25.2% power conversion efficiency', *Nature materials*, vol. 17, no. 9, pp. 820–826, 2018.
- [22] F. Gota, M. Langenhorst, R. Schmager, J. Lehr, and U. W. Paetzold, 'Energy yield advantages of three-terminal perovskite-silicon tandem photovoltaics', *Joule*, vol. 4, no. 11, pp. 2387–2403, 2020.
- [23] S. Gharibzadeh *et al.*, '2D/3D heterostructure for semitransparent perovskite solar cells with engineered bandgap enables efficiencies exceeding 25% in four-terminal tandems with silicon and CIGS', *Advanced Functional Materials*, vol. 30, no. 19, p. 1909919, 2020.
- [24] R. Schmager, M. Langenhorst, J. Lehr, U. Lemmer, B. S. Richards, and U. W. Paetzold, 'Methodology of energy yield modelling of perovskite-based multi-junction photovoltaics', *Optics express*, vol. 27, no. 8, pp. A507–A523, 2019.
- [25] M. Singh, R. Santbergen, I. Syifai, A. Weeber, M. Zeman, and O. Isabella, 'Comparing optical performance of a wide range of perovskite/silicon tandem architectures under real-world conditions', *Nanophotonics*, vol. 10, no. 8, pp. 2043–2057, 2020, doi: 10.1515/nanoph-2020-0643.
- [26] A. S. Subbiah *et al.*, 'High-performance perovskite single-junction and textured perovskite/silicon tandem solar cells via slot-die-coating', *ACS Energy Letters*, vol. 5, no. 9, pp. 3034–3040, 2020.
- [27] J. Zheng *et al.*, 'Large-area 23%-efficient monolithic perovskite/homojunction-silicon tandem solar cell with enhanced UV stability using down-shifting material', *ACS Energy Letters*, vol. 4, no. 11, pp. 2623–2631, 2019.
- [28] E. Köhnen *et al.*, 'Highly efficient monolithic perovskite silicon tandem solar cells: analyzing the influence of current mismatch on device performance', *Sustainable Energy & Fuels*, vol. 3, no. 8, pp. 1995–2005, 2019.
- [29] M. I. Hossain, W. Qarony, S. Ma, L. Zeng, D. Knipp, and Y. H. Tsang, 'Perovskite/Silicon Tandem Solar Cells: From Detailed Balance Limit Calculations to Photon Management', *Nano-Micro Letters*, vol. 11, no. 1, p. 58, Jul. 2019, doi: 10.1007/s40820-019-0287-8.
- [30] H. Liu, C. D. Rodríguez-Gallegos, Z. Liu, T. Buonassisi, T. Reindl, and I. M. Peters, 'A Worldwide Theoretical Comparison of Outdoor Potential for Various Silicon-Based Tandem Module Architecture', *Cell Reports Physical Science*, vol. 1, no. 4, p. 100037, Apr. 2020, doi: 10.1016/j.xcrp.2020.100037.
- [31] A. Smets, K. Jäger, O. Isabella, R. van Swaaij, and M. Zeman, *Solar Energy: The Physics and Engineering of Photovoltaic Conversion, Technologies and Systems*. UIT Cambridge, 2016. [Online]. Available: <https://books.google.nl/books?id=vTkdjgEACAAJ>
- [32] S. P. Bremner, M. Y. Levy, and Christiana B Honsberg, 'Analysis of tandem solar cell efficiencies under {AM1.5G} spectrum using a rapid flux calculation method', *Progress in Photovoltaics: Research and Applications*, vol. 16, 2008, [Online]. Available: <http://dx.doi.org/10.1002/pip.799>
- [33] Z. Wang, Z. Song, Y. Yan, S. (Frank) Liu, and D. Yang, 'Perovskite—a Perfect Top Cell for Tandem Devices to Break the S–Q Limit', *Advanced Science*, vol. 6, no. 7, p. 1801704, Apr. 2019, doi: 10.1002/adv.201801704.

- [34] J. Werner *et al.*, 'Efficient Near-Infrared-Transparent Perovskite Solar Cells Enabling Direct Comparison of 4-Terminal and Monolithic Perovskite/Silicon Tandem Cells', *ACS Energy Lett.*, vol. 1, no. 2, pp. 474–480, Aug. 2016, doi: 10.1021/acseenergylett.6b00254.
- [35] J. Werner *et al.*, 'Parasitic Absorption Reduction in Metal Oxide-Based Transparent Electrodes: Application in Perovskite Solar Cells', *ACS Appl. Mater. Interfaces*, vol. 8, no. 27, pp. 17260–17267, Jul. 2016, doi: 10.1021/acscami.6b04425.
- [36] C. Comparotto *et al.*, 'Bifacial n-type solar modules: indoor and outdoor evaluation', 2014, pp. 3248–3250.
- [37] R. Guerrero-Lemus, R. Vega, T. Kim, A. Kimm, and L. E. Shephard, 'Bifacial solar photovoltaics – A technology review', *Renewable and Sustainable Energy Reviews*, vol. 60, pp. 1533–1549, Jul. 2016, doi: 10.1016/j.rser.2016.03.041.
- [38] A. Hubner, A. Aberle, and R. Hezel, 'Temperature behavior of monofacial and bifacial silicon solar cells', 1997, pp. 223–226.
- [39] W. Gu, T. Ma, A. Song, M. Li, and L. Shen, 'Mathematical modelling and performance evaluation of a hybrid photovoltaic-thermoelectric system', *Energy Conversion and Management*, vol. 198, p. 111800, 2019.
- [40] W. Gu, T. Ma, S. Ahmed, Y. Zhang, and J. Peng, 'A comprehensive review and outlook of bifacial photovoltaic (bPV) technology', *Energy Conversion and Management*, vol. 223, p. 113283, Nov. 2020, doi: 10.1016/j.enconman.2020.113283.
- [41] A. Faes *et al.*, 'Metallization and interconnection for high-efficiency bifacial silicon heterojunction solar cells and modules', *Photovolt. Int.*, vol. 41, pp. 65–76, 2018.
- [42] J. Yu *et al.*, 'Tungsten doped indium oxide film: Ready for bifacial copper metallization of silicon heterojunction solar cell', *Solar Energy Materials and Solar Cells*, vol. 144, pp. 359–363, 2016.
- [43] T. Hatt *et al.*, 'Novel mask-less plating metallization route for bifacial silicon heterojunction solar cells', 2018, vol. 1999, no. 1, p. 040009.
- [44] A. Chebotareva, G. Untila, T. Kost, A. Stepanov, S. Salazkin, and V. Shaposhnikova, 'Bifacial silicon heterojunction solar cells with advanced Ag-free multi-wire metallization attached to ITO layers using new transparent conductive PAEK copolymers', *Solar Energy*, vol. 193, pp. 828–836, 2019.
- [45] J. Wang, Y. Xuan, L. Zheng, Y. Xu, and L. Yang, 'Improvement of bifacial heterojunction silicon solar cells with light-trapping asymmetrical bifacial structures', *Solar Energy*, vol. 223, pp. 229–237, 2021.
- [46] C. Voz *et al.*, 'Bifacial heterojunction silicon solar cells by hot-wire CVD with open-circuit voltages exceeding 600 mV', *Thin solid films*, vol. 511, pp. 415–419, 2006.
- [47] J. Haschke *et al.*, 'The impact of silicon solar cell architecture and cell interconnection on energy yield in hot & sunny climates', *Energy Environ. Sci.*, vol. 10, no. 5, pp. 1196–1206, 2017, doi: 10.1039/C7EE00286F.
- [48] T. Mishima, M. Taguchi, H. Sakata, and E. Maruyama, 'Development status of high-efficiency HIT solar cells', *Solar Energy Materials and Solar Cells*, vol. 95, no. 1, pp. 18–21, Jan. 2011, doi: 10.1016/j.solmat.2010.04.030.
- [49] G. Coletti *et al.*, 'Bifacial Four-Terminal Perovskite/Silicon Tandem Solar Cells and Modules', *ACS Energy Lett.*, vol. 5, no. 5, pp. 1676–1680, May 2020, doi: 10.1021/acseenergylett.0c00682.
- [50] R. Asadpour, R. V. Chavali, M. Ryyan Khan, and M. A. Alam, 'Bifacial Si heterojunction-perovskite organic-inorganic tandem to produce highly efficient ($\eta_{T^*} \sim 33\%$) solar cell', *Applied Physics Letters*, vol. 106, no. 24, p. 243902, 2015.
- [51] IEC, 'Photovoltaic devices - Part 3: Measurement principles for terrestrial photovoltaic (PV) solar devices with reference spectral irradiance data (IEC 60904-3:2019)'. Feb. 15, 2019. [Online]. Available: <https://www.sis.se/api/document/preview/572792/>
- [52] J. M. Freeman *et al.*, 'System Advisor Model (SAM) General Description (Version 2017.9.5)', NREL/TP--6A20-70414, 1440404, May 2018. doi: 10.2172/1440404.

- [53] Z. Wang, O. Isabella, R. Santbergen, R. van Swaaij, and Z. Qin, 'Improvements and Experimental Validation of the PVMD Toolbox'. Jun. 28, 2019. [Online]. Available: <https://repository.tudelft.nl/islandora/object/uuid:5cc83e7e-e18e-4c80-9ab0-91616af83978?collection=education>
- [54] D. Berrian, J. Libal, and S. Glunz, 'MoBiDiG simulations and LCOE', 2017, pp. 25–26.
- [55] A. R. Burgers, G. J. M. Janssen, and B. B. van Aken, 'BIGEYE: Accurate energy yield prediction of bifacial PV systems'. TNO. [Online]. Available: <https://repository.tno.nl/islandora/object/uuid%3Ad34d4e48-4f2d-4afe-aff8-ca5771fbc400>
- [56] A. Nour El Din, 'Improved Electrical Model and Experimental Validation of the PVMD Toolbox'. Jul. 15, 2020.
- [57] R. Santbergen, T. Meguro, T. Suezaki, G. Koizumi, K. Yamamoto, and M. Zeman, 'GenPro4 Optical Model for Solar Cell Simulation and Its Application to Multijunction Solar Cells', *IEEE Journal of Photovoltaics*, vol. 7, no. 3, pp. 919–926, May 2017, doi: 10.1109/JPHOTOV.2017.2669640.
- [58] R. Santbergen, V. A. Muthukumar, R. M. E. Valckenborg, W. J. A. van de Wall, A. H. M. Smets, and M. Zeman, 'Calculation of irradiance distribution on PV modules by combining sky and sensitivity maps', *Solar Energy*, vol. 150, pp. 49–54, Jul. 2017, doi: 10.1016/j.solener.2017.04.036.
- [59] 'Meteonorm: Handbook part II'. Meteonorm, Sep. 2020. [Online]. Available: https://meteonorm.com/assets/downloads/mn80_theory.pdf
- [60] R. Perez, R. Seals, and J. Michalsky, 'All-weather model for sky luminance distribution—Preliminary configuration and validation', *Solar Energy*, vol. 50, no. 3, pp. 235–245, Mar. 1993, doi: 10.1016/0038-092X(93)90017-I.
- [61] E. Garcia Goma, O. Isabella, and R. Santbergen, 'Development of Cell to System Annual Energy Yield Toolbox for Bifacial Modules'. Apr. 20, 2018. [Online]. Available: <https://repository.tudelft.nl/islandora/object/uuid%3A255ac731-b59b-453a-b899-1ff5dec1add2?collection=education>
- [62] F. Feldmann, M. Bivour, C. Reichel, M. Hermle, and S. W. Glunz, 'A Passivated Rear Contact for High-Efficiency n-Type Si Solar Cells Enabling High Voc's and FF>82 %', *28th European Photovoltaic Solar Energy Conference and Exhibition; 988-992*, p. 5 pages, 4939 kb, 2013, doi: 10.4229/28THEUPVSEC2013-2CO.4.4.
- [63] A. J. Preetham, P. Shirley, and B. Smits, 'A practical analytic model for daylight', 1999, pp. 91–100.
- [64] M. Zeman, J. van den Heuvel, M. Kroon, and J. Willemen, 'Advanced Semiconductor Analysis'. Aug. 23, 2019.
- [65] R. V. Klassen, 'Modeling the effect of the atmosphere on light', *ACM Trans. Graph.*, vol. 6, no. 3, pp. 215–237, Jul. 1987, doi: 10.1145/35068.35071.
- [66] L. HošekHošek and A. Wilkie, 'Adding a solar-radiance function to the hošek-wilkie skylight model', *IEEE computer graphics and applications*, vol. 33, no. 3, pp. 44–52, 2013.
- [67] L. Hosek and A. Wilkie, 'An analytic model for full spectral sky-dome radiance', *ACM Transactions on Graphics (TOG)*, vol. 31, no. 4, pp. 1–9, 2012.
- [68] T. Nishita, Y. Dobashi, K. Kaneda, and H. Yamashita, 'Display method of the sky color taking into account multiple scattering', 1996, vol. 96, pp. 117–132.
- [69] J. Mardaljevic, 'Daylight Simulation: Validation, Sky Models and Daylight Coefficients'. Dec. 1999. Accessed: Feb. 07, 2021. [Online]. Available: https://repository.lboro.ac.uk/articles/thesis/Daylight_simulation_validation_sky_models_and_daylight_coefficients/9460817
- [70] T. R. Kol, 'Analytic sky simulation: An implementation and analysis of daytime skylight models'. [Online]. Available: <https://www.timothykol.com/pub/sky.pdf>

- [71] Y. K. Yi, J. Yin, and Y. Tang, 'Developing an advanced daylight model for building energy tool to simulate dynamic shading device', *Solar Energy*, vol. 163, pp. 140–149, Mar. 2018, doi: 10.1016/j.solener.2018.01.082.
- [72] M. Ayoub, 'A review on light transport algorithms and simulation tools to model daylighting inside buildings', *Solar Energy*, vol. 198, pp. 623–642, Mar. 2020, doi: 10.1016/j.solener.2020.02.018.
- [73] R. Nave, 'Blue sky'. <http://hyperphysics.phy-astr.gsu.edu/hbase/atmos/blusky.html>
- [74] T. Kment, M. Rauter, and G. Zotti, 'Modelling of Daylight for Computer Graphics'. TU Wien. Accessed: Apr. 07, 2021. [Online]. Available: https://www.academia.edu/809995/Modelling_of_Daylight_for_Computer_Graphics
- [75] Inc. Woodard & Curran, '5 - Waste Characterization', in *Industrial Waste Treatment Handbook (Second Edition)*, Inc. Woodard & Curran, Ed. Burlington: Butterworth-Heinemann, 2006, pp. 83–126. doi: 10.1016/B978-075067963-3/50007-2.
- [76] E. J. McCartney and F. F. Hall, 'Optics of the Atmosphere: Scattering by Molecules and Particles', *Physics Today*, vol. 30, no. 5, pp. 76–77, May 1977, doi: 10.1063/1.3037551.
- [77] Y. Uetani *et al.*, 'SPATIAL DISTRIBUTION OF DAYLIGHT - CIE STANDARD GENERAL SKY'. CIE, 2004. Accessed: Mar. 07, 2021. [Online]. Available: <https://cie.co.at/publications/spatial-distribution-daylight-cie-standard-general-sky>
- [78] G. Zotti, A. Wilkie, and W. Purgathofer, 'A Critical Review of the Preetham Skylight Model', 2007.
- [79] P. Mertz, "'Color Science: Concepts and Methods, Quantitative Data and Formulas" (Günter Wyszecki and W. S. Stiles; 1967) [Books Reviewed]', *Journal of the SMPTE*, vol. 76, no. 11, pp. 1154–1154, Nov. 1967, doi: 10.5594/J13680.
- [80] A. Vladimír, 'Fast Icosphere Mesh', *Fast Icosphere Mesh*, Sep. 23, 2019. <https://observablehq.com/@mourner/fast-icosphere-mesh>
- [81] C. Poynton, Ed., '25 - The CIE system of colorimetry', in *Digital Video and HD (Second Edition)*, Boston: Morgan Kaufmann, 2012, pp. 265–286. doi: 10.1016/B978-0-12-391926-7.50025-4.
- [82] R. E. Bird, 'A simple, solar spectral model for direct-normal and diffuse horizontal irradiance', *Solar Energy*, vol. 32, no. 4, pp. 461–471, Jan. 1984, doi: 10.1016/0038-092X(84)90260-3.
- [83] 'Analemma', *Astronomy 101*. https://www.wvu.edu/astro101/a101_analemma.shtml (accessed Dec. 07, 2021).
- [84] R. W. G. Hunt and M. Pointer, *Measuring colour*, 4. ed. Chichester: Wiley, 2011.
- [85] B. Goss, I. R. Cole, E. Koubli, D. Palmer, T. R. Betts, and R. Gottschalg, '4 - Modelling and prediction of PV module energy yield', in *The Performance of Photovoltaic (PV) Systems*, N. Pearsall, Ed. Woodhead Publishing, 2017, pp. 103–132. doi: 10.1016/B978-1-78242-336-2.00004-5.
- [86] C. Saravanan and M. Panneerselvam, 'A Comprehensive Analysis for Extracting Single Diode PV Model Parameters by Hybrid GA-PSO Algorithm', *International Journal of Computer Applications*, vol. 78, pp. 16–19, 2013.
- [87] S. Silvestre, 'Chapter 7 - Strategies for Fault Detection and Diagnosis of PV Systems', in *Advances in Renewable Energies and Power Technologies*, I. Yahyaoui, Ed. Elsevier, 2018, pp. 231–255. doi: 10.1016/B978-0-12-812959-3.00007-1.
- [88] M. Theristis, V. Venizelou, G. Makrides, and G. E. Georghiou, 'Chapter II-1-B - Energy Yield in Photovoltaic Systems', in *McEvoy's Handbook of Photovoltaics (Third Edition)*, S. A. Kalogirou, Ed. Academic Press, 2018, pp. 671–713. doi: 10.1016/B978-0-12-809921-6.00017-3.
- [89] C. W. Hansen, 'Estimation of parameters for single diode models using measured IV curves', in *2013 IEEE 39th Photovoltaic Specialists Conference (PVSC)*, Jun. 2013, pp. 0223–0228. doi: 10.1109/PVSC.2013.6744135.
- [90] J. Bikaneria and S. P. Joshi, 'Modelling and simulation of PV cell based on two-diode model', *International Journal on Recent Trends in Engineering & Technology*, vol. 11, no. 1, p. 589, 2014.

- [91] M. Hejri, H. Mokhtari, M. R. Azizian, M. Ghandhari, and L. Söder, 'On the Parameter Extraction of a Five-Parameter Double-Diode Model of Photovoltaic Cells and Modules', *IEEE Journal of Photovoltaics*, vol. 4, no. 3, pp. 915–923, May 2014, doi: 10.1109/JPHOTOV.2014.2307161.
- [92] D. Muhsen, H. T. Haider, and H. Shahadi, 'PARAMETER EXTRACTION OF SINGLE-DIODE PV-MODULE MODEL USING ELECTROMAGNETISM-LIKE ALGORITHM', 2018.
- [93] A. M. Eltamaly, 'Performance of smart maximum power point tracker under partial shading conditions of photovoltaic systems', *Journal of Renewable and Sustainable Energy*, vol. 7, no. 4, p. 043141, 2015.
- [94] N. M. Shannan, N. Z. Yahaya, and B. Singh, 'Two diode model for parameters extraction of PV module', 2014, pp. 260–264.
- [95] N. M. A. Alrahim Shannan, N. Z. Yahaya, and B. Singh, 'Single-diode model and two-diode model of PV modules: A comparison', in *2013 IEEE International Conference on Control System, Computing and Engineering*, Dec. 2013, pp. 210–214. doi: 10.1109/ICCSCE.2013.6719960.
- [96] E. I. Batzelis and S. A. Papathanassiou, 'A Method for the Analytical Extraction of the Single-Diode PV Model Parameters', *IEEE Transactions on Sustainable Energy*, vol. 7, no. 2, pp. 504–512, Apr. 2016, doi: 10.1109/TSTE.2015.2503435.
- [97] O. Hachana, K. E. Hemsas, G. M. Tina, and C. Ventura, 'Comparison of different metaheuristic algorithms for parameter identification of photovoltaic cell/module', *Journal of Renewable and Sustainable Energy*, vol. 5, no. 5, p. 053122, Sep. 2013, doi: 10.1063/1.4822054.
- [98] 'Single Diode Equivalent Circuit Models', *DC Module IV characteristics*. <https://pvpmc.sandia.gov/modeling-steps/2-dc-module-iv/diode-equivalent-circuit-models/> (accessed Jul. 13, 2021).
- [99] P. J. Verlinden, 'Chapter IC-5 - High-Efficiency Back-Contact Silicon Solar Cells for One-Sun and Concentrator Applications', in *Solar Cells (Second Edition)*, A. McEvoy, L. Castañer, and T. Markvart, Eds. Elsevier, 2013, pp. 327–351. doi: 10.1016/B978-0-12-386964-7.00011-1.
- [100] M. S. Benghanem and S. N. Alamri, 'Modeling of photovoltaic module and experimental determination of serial resistance', *Journal of Taibah University for Science*, vol. 2, pp. 94–105, Jan. 2009, doi: 10.1016/S1658-3655(12)60012-0.
- [101] M. S. I. RAGEH and F. A. S. SOLIMAN, 'RADIATION DAMAGE IN SILICON SOLAR CELLS BY HELIUM IONS', in *Energy and the Environment*, A. A. M. SAYIGH, Ed. Oxford: Pergamon, 1990, pp. 351–356. doi: 10.1016/B978-0-08-037539-7.50058-2.
- [102] E. Kobayashi *et al.*, 'Increasing the efficiency of silicon heterojunction solar cells and modules by light soaking', *Solar Energy Materials and Solar Cells*, vol. 173, pp. 43–49, Dec. 2017, doi: 10.1016/j.solmat.2017.06.023.
- [103] A. Alnuaimi, I. Almansouri, and A. Nayfeh, 'Effect of mobility and band structure of hole transport layer in planar heterojunction perovskite solar cells using 2D TCAD simulation', *J Comput Electron*, vol. 15, no. 3, pp. 1110–1118, Sep. 2016, doi: 10.1007/s10825-016-0850-1.
- [104] T. Minemoto and M. Murata, 'Device modeling of perovskite solar cells based on structural similarity with thin film inorganic semiconductor solar cells', *Journal of Applied Physics*, vol. 116, no. 5, p. 054505, Aug. 2014, doi: 10.1063/1.4891982.
- [105] M. S. Benghanem and S. N. Alamri, 'Modeling of photovoltaic module and experimental determination of serial resistance', *Journal of Taibah University for Science*, vol. 2, pp. 94–105, Jan. 2009, doi: 10.1016/S1658-3655(12)60012-0.
- [106] E. L. Meyer, 'Extraction of Saturation Current and Ideality Factor from Measuring Voc and Isc of Photovoltaic Modules', *International Journal of Photoenergy*, vol. 2017, p. 8479487, Dec. 2017, doi: 10.1155/2017/8479487.
- [107] P. Baruch, A. De Vos, P. T. Landsberg, and J. E. Parrott, 'On some thermodynamic aspects of photovoltaic solar energy conversion', *Solar Energy Materials and Solar Cells*, vol. 36, no. 2, pp. 201–222, Feb. 1995, doi: 10.1016/0927-0248(95)80004-2.
- [108] H. F. Wolf and R. L. Meek, 'Semiconductors', *Journal of The Electrochemical Society*, vol. 119, no. 8, p. 256C, 1972, doi: 10.1149/1.2404419.

- [109] T. Dittrich, C. Awino, P. Prajongtat, B. Rech, and M. Ch. Lux-Steiner, 'Temperature Dependence of the Band Gap of $\text{CH}_3\text{NH}_3\text{PbI}_3$ Stabilized with PMMA: A Modulated Surface Photovoltage Study', *J. Phys. Chem. C*, vol. 119, no. 42, pp. 23968–23972, Oct. 2015, doi: 10.1021/acs.jpcc.5b07132.
- [110] MathWorks, 'polyfit'. <https://nl.mathworks.com/help/matlab/ref/polyfit.html> (accessed Jul. 28, 2021).
- [111] Z. Machacek, V. Benda, R. Barinka, Praha, and R. Radh, 'Parameters of photovoltaic cells in dependence on irradiance and temperature', Jul. 2021.
- [112] T. Hitosugi, N. Yamada, S. Nakao, Y. Hirose, and T. Hasegawa, 'Properties of TiO₂-based transparent conducting oxides', *phys. stat. sol. (a)*, vol. 207, no. 7, pp. 1529–1537, Jun. 2010, doi: 10.1002/pssa.200983774.
- [113] D. Zhang, W. Soppe, and R. E. I. Schropp, 'Design of 4-terminal Solar Modules Combining Thin-film Wide-Bandgap Top Cells and c-Si Bottom Cells', *Energy Procedia*, vol. 77, pp. 500–507, Aug. 2015, doi: 10.1016/j.egypro.2015.07.071.
- [114] Y. Jiang *et al.*, 'Optical analysis of perovskite/silicon tandem solar cells', *J. Mater. Chem. C*, vol. 4, no. 24, pp. 5679–5689, 2016, doi: 10.1039/C6TC01276K.
- [115] M. Z. Jacobson and V. Jadhav, 'World estimates of PV optimal tilt angles and ratios of sunlight incident upon tilted and tracked PV panels relative to horizontal panels', *Solar Energy*, vol. 169, pp. 55–66, Jul. 2018, doi: 10.1016/j.solener.2018.04.030.
- [116] J. Lehr *et al.*, 'Energy yield of bifacial textured perovskite/silicon tandem photovoltaic modules', *Solar Energy Materials and Solar Cells*, vol. 208, p. 110367, 2020.
- [117] M. De Bastiani *et al.*, 'Efficient bifacial monolithic perovskite/silicon tandem solar cells via bandgap engineering', *Nature Energy*, vol. 6, no. 2, pp. 167–175, 2021.
- [118] A. Onno *et al.*, 'Predicted power output of silicon-based bifacial tandem photovoltaic systems', *Joule*, vol. 4, no. 3, pp. 580–596, 2020.
- [119] C. Honsberg and S. Bowden, 'Absorption depth'. <https://www.pveducation.org/pvcdrom/pn-junctions/absorption-depth> (accessed May 08, 2021).
- [120] L. A. Kosyachenko, Ed., *Solar Cells - Thin-Film Technologies*. InTech, 2011. doi: 10.5772/821.